Non-parametric Bayesian Spatial Normalization in Medical Imaging

DISSERTATION
zur Erlangung des Doktorgrades der Technischen Fakultät der
Albert-Ludwigs-Universität Freiburg im Breisgau

vorgelegt von
David Pilutti

UNIVERSITÄTS
KLINIKUM FREIBURG

UNI
FREIBURG

Dekan: Prof. Dr. Georg Lausen

Date of the defense: April 27, 2016

Prüfungskommission:

Prof. Dr. Matthias Teschner	(Vorsitz)
Prof. Dr. Rolf Backofen	(Beisitz)
Prof. Dr.-Ing. Thomas Brox	(1. Gutachter)
Prof. Dr. Dr. h. c. Jürgen Hennig	(2. Gutachter)

Abstract

Medical imaging modalities provide high quality three-dimensional data sets that can be used to study anatomy and pathologies. Medical images of internal organs are often used to highlight the anatomy of the internal organs as well as to identify lesions such as tumors in different regions of the human body. Such images can help the clinicians in the qualitative characterization of a lesion in the investigated organs and in the consequent diagnosis of a disease. The automated analysis of medical images is a challenging task due to different artifacts which are often resulting from the displacement of internal organs due to physiological motion and of the scanned patient. This requires further processing with automated methods such as registration and segmentation. Different images of the same patient are normally taken at different time points along the scan session, making the resulting images susceptible to movements of internal organs such as due to respiration, heart-beat, and peristalsis. The post-processing for alignment of medical images representing internal organs is fundamental for their quantitative and even qualitative analysis. Analytical methods for image registration may help to obtain the desired alignment of medical images and may be applied to images of different organs.

Magnetic Resonance Imaging (MRI) has been used extensively to investigate the human brain. A brain MRI examination protocol typically includes several imaging contrasts that can provide complementary information by highlighting different tissue properties. The acquired datasets often need to be co-registered or processed to compute a standard anatomic space before any further processing. In particular, the identification of vital tumors in the internal organs of chest, abdomen, and pelvis anatomic regions can be performed with the analysis of Dynamic Contrast Enhanced Magnetic Resonance Imaging (DCE-MRI) data. The contrast agent is accumulated differently by pathologic and healthy tissues and that results in a temporally varying contrast in an image series. The internal organs of the torso

are also subject to potentially extensive movements mainly due to breathing, heart-beat, and peristalsis. This contributes to making the analysis of DCE-MRI datasets challenging as well as time consuming. Current registration methods particularly for data with different contrasts are computationally very intensive, their resolution is lower than that of the images, and their distance metric and its optimization can be limiting.

The work in this thesis proposes a novel pairwise non-rigid registration method with a Non-Parametric Bayesian Registration (NParBR) formulation. The NParBR method assumes an underlying model for the effect of the distortion on the joint intensity statistics, a non-parametric prior for the restored statistics, and also applies a spatial regularization for the estimated registration with Gaussian filtering. In this thesis the NParBR method is applied to different registration problems including to images of the same contrast, different contrasts, and DCE-MRI as well as to images from different modalities such as MRI and Computed Tomography (CT). The validation of the NParBR method applied to human brain data has been performed with a modificaiton of the Shepp-Logan phantom, images from the BrainWeb database, the real data of the NIREP database, and real multi-contrast datasets of 5 healthy volunteers. A minimally biased intra-dataset atlas is computed for each DCE-MRI dataset and used as reference for the registration of the time series. The time series registration method has been tested with 20 datasets including the liver, lungs, intestines, and the prostate. It has been compared to the B-Splines and to the SyN methods with results that demonstrate that the proposed method improves both accuracy and efficiency.

Zusammenfassung

Die medizinische Bildgebung erzeugt qualitativ hochwertige dreidimensionale Datensätze, die verwendet werden, um Gewebeanatomie und pathologie zu studieren. Medizinische Bilder der inneren Organe werden oft eingesetzt, um die Anatomie darzustellen sowie Läsionen wie Tumoren in verschiedenen Bereichen des menschlichen Körpers zu identifizieren. Solche Bilder helfen den Ärzten bei der qualitativen Charakterisierung von Läsionen in den untersuchten Organen und bei der daraus resultierenden Diagnose einer Krankheit. Die automatisierte Analyse von medizinischen Bildern ist eine schwierige Aufgabe aufgrund verschiedener Artefakte, die oft aus der Bewegung der inneren Organe resultieren welche durch physiologische Bewegungen oder Bewegungen des untersuchten Patienten hervorgerufen werden. Die Analyse erfordert die Weiterverarbeitung mit automatisierten Verfahren wie der Registrierung und der Segmentierung. Unterschiedliche Bilder des gleichen Patienten werden normalerweise zu verschiedenen Zeitpunkten während der Untersuchung aufgenommen, so dass die resultierenden Bilder anfällig sind für Bewegungen der inneren Organe aufgrund von Atmung, Herzschlag und Peristaltik. Die Nachverarbeitung zur Ausrichtung von medizinischen Bildern, die die inneren Organe darstellen, ist entscheidend für die quantitative und qualitative Analyse. Analyseverfahren zur Bildregistrierung können helfen, medizinische Bilder in der gewünschten Ausrichtung zu erhalten, und können bei verschiedenen Organen eingesetzt werden.

Die Magnetresonanztomographie (MRT) wurde ausgiebig zur Untersuchung des menschlichen Gehirns eingesetzt. Ein MRT-Protokoll zur Untersuchung des Hirns beinhaltet in der Regel mehrere Bildkontraste, die komplementäre Informationen liefern, indem sie verschiedene Gewebeeigenschaften hervorheben. Die gemessenen Datensätze müssen oft koregistriert oder bearbeitet werden, um sie auf standardisierte anatomische Koordinaten abzubilden, bevor sie weiterverarbeitet werden können. Insbesondere können vitale Tumoren der inneren Organe der Brust, des Bauchs, oder des Beckens identifiziert werden durch die Analyse von dynamischen kontrastverstärkten Magnetresonanztomographie-Daten (DCE-MRI). Das Kontrastmittel wird durch pathologisches und gesundes Gewebe unterschiedlich akkumuliert, was zu einem zeitlich veränderlichen Kontrast in einer Bildserie führt. Die inneren Organe des Torsos unterliegen ebenfalls potentiell umfangreichen Bewegungen, vor allem aufgrund von Atmung, Herzschlag und Peristaltik. Dies trägt dazu bei, dass die Analyse der DCE-MRI Datensätze schwierig und zeitaufwendig wird. Aktuellen Registrierungsverfahren sind insbesondere für Daten mit unterschiedlichen Kontrasten sehr rechenintensiv, ihre Auflösung ist geringer als die der Eingangsbilder, und ihre Distanzmetrik und deren Optimierung kann einschränkend sein.

Diese Arbeit schlägt eine neue, paarweise, nicht-starre Registrierung mit einer nicht-parametrischen Formulierung der Bayes-Registrierung (NParBR) vor. Das NParBR Verfahren geht aus von einem zugrundeliegenden Modell für die Wirkung der Verzerrung auf die gemeinsame Intensitätsstatistik, einem nicht-parametrischen Voraussetzung (prior) für die rekonstruierte Statistik, und es wendet eine räumliche Regularisierung an für die Schätzung der Registrierung mit Gauß-Filterung. Das NParBR Verfahren wird in dieser Arbeit auf verschiedene Registrierungsprobleme angewandt, einschließlich Bildern gleichen und unterschiedlichen Kontrasts, DCE-MRI sowie Bilder von verschiedenen Modalitäten wie der MRT und der Computertomographie (CT). Die Validierung des NParBR Verfahrens für Daten des menschlichen Gehirns wurde mit einem modifizierten Shepp-Logan Phantom, Bildern aus der BrainWeb Datenbank, realen Daten der NIREP Datenbank und gemessenen Multikontrastdatensätzen von 5 gesunden Probanden durchgefhrt. Für jeden DCE-MRI-Datensatz wurde ein interner Atlas mit minimaler Abweichung (minimal bias) berechnet und als Referenz für die Registrierung der Zeitreihe verwendet. Die Zeitreihenregistrierung wurde an 20 Datensätzen der Leber, der Lunge, des Darms, und der Prostata getestet. Es wurde außerdem zu B-Splines- und SyN-Methoden verglichen, und die Ergebnisse zeigten, dass das vorgeschlagene Verfahren sowohl die Genauigkeit als auch die Effizienz verbessert.

Contents

List of Publications

International Journals

David Pilutti, Maddalena Strumia, Martin Büchert, Stathis Hadjidemetriou. *Non-Parametric Bayesian Registration (NParBR) of Body Tumors in DCE-MRI Data.* Submitted to IEEE Transactions on Medical Imaging - accepted. DOI:10.1109/ TMI.2015.2506338.

David Pilutti, Maddalena Strumia, Stathis Hadjidemetriou. *Bi-modal Non-rigid Registration of Brain MRI Data with Deconvolution of Joint Statistics.* IEEE Transactions on Image Processing, vol. 23, no. 9, 2014.

Inge Kalis, **David Pilutti**, Axel J. Krafft, Jürgen Hennig, Michael Bock. *Time-Resolved Renal BOLD MRI with Prospective Image Alignment.* Magnetic Resonance in Medicine (MRM), 2016.

International Conferences

David Pilutti, Maddalena Strumia, Stathis Hadjidemetriou: *Non-Parametric Bayesian Registration (NParBR) on CT Lungs Data-EMPIRE10 Challenge*, url:http://empire10.isi.uu.nl/ (2015).

David Pilutti, Maddalena Strumia, Stathis Hadjidemetriou: *Bi-Modal Non-Rigid Registration of Brain MRI Data Based on Deconvolution of Joint Statistics.* Oral and poster presentation. In proceedings of MBIA 2013, MICCAI Workshop Nagoya, September 2013

David Pilutti, Martin Büchert, Stathis Hadjidemetriou. *Registration of Abdominal*

Tumor DCE-MRI Data Based on Deconvolution of Joint Statistics. Oral and poster presentation. In proceedings of EMBC 2013 Osaka, July 2013

David Pilutti, Martin Büchert, Stathis Hadjidemetriou. *DCE-MRI Registration of Abdominal Tumor Data Based on Deconvolution of Joint Statistics.* Oral and poster presentation. In proceedings of MIBISOC Buxelles, May 2013. ISBN: 978-84-695-7710-3.

David Pilutti, Martin Büchert, Stathis Hadjidemetriou. *Registration of DCE-MRI Image Sequences Based on Multicontrast Optical Flow.* Poster presentation, ISBI 2012, Barcelona.

David Pilutti, Claudia Weidensteiner, Martin Büchert, Ulrike Fasol, Stathis Hadjidemetriou. *An overview of registration methods used for the automatic analysis of abdominal DCE-MRI.* Educational e-poster. In proceedings of ISMRM 2011, Montreal.

Glossary

CC: Cross Correlation

CR: Correlation Ratio

CSF: Cerebro-Spinal Fluid

CT: Computed Tomography

DCE-MRI: Dynamic Contrast Enhanced - Magnetic Resonance Imaging

EMPIRE10: Evaluation of Methods for Pulmonary Image Registration 2010

FFD: Free Form Deformations

FFT: Fast Fourier Transform

FLAIR: FLuid Attenuation Inversion Recovery

fMRI: functional Magnetic Resonance Imaging

H.O.T.: High Order Terms

LDDMM: Large Deformation Diffeomorphic Metric Mapping

MACMI: Multi Attribute Combined Mutual Information

MRF: Markov Random Fields

MI: Mutual Information

MIND: Modality Independent Neighborhood Descriptor

MRI: Magnetic Resonance Imaging

MS: Multiple Sclerosis

NCC: Normalized Cross Correlation

NIREP: Non-Rigid Image Registration Evaluation Project

NMI: Normalized Mutual Information

NParBR: Non-Parametric Bayesian Registration

PCA: Principal Component Analysis

PET: Positron Emission Tomography

PPCR: Progressive Principal Component Registration

PSD: Power Spectral Densities

RF: Radio Frequency

RIU: Ratio of Image Uniformity

ROI: Region Of Interest

SAD: Sum of Absolute Differences

SIFT: Scale Invariant Feature Transform

SNR: Signal to Noise Ratio

SOR: Successive Over Relaxation

SPECT: Single Photon Emission Computed Tomography

SSD: Sum of Squared Differences

SyN: Symmetric Normalization

US: Ultra Sound

Chapter 1

Motivation of Work

The alignment of medical images is fundamental for many automated post-processing methods and for a qualitative and quantitative analysis of image datasets of internal organs. The intra-subject registration is necessary since images from the same subject taken at different time points during the same scan session may be affected by different types of movement such as patient displacement, respiration, heart-beat, and peristalsis. Another application of the intra-subject image registration is the alignment of images from the same subject taken within different scan sessions. In this case the registration can help to better identify the evolution of a possible lesion in time. Another motivation for the intra-subject registration comes from spatial normalizations that can be handled differently within MRI scanners. Images of subjects taken from different imaging modalities such as MRI, CT, PET, and others, also need to be co-registered to better identify the functionality of certain anatomy (MRI-fMRI, MRI-PET) or a lesion (T_1w-MRI-T_2w-MRI, T_1w-MRI-FLAIR-MRI). Image registration can be performed also as inter-subject mainly for the creation of anatomical atlases.

Image co-registration is still an open problem which has raised a wide number of different approaches and, consequently, a significant literature. Methods with limited degrees of freedom such as rigid and affine registration methods can perform an alignment of images in an efficient way giving a global solution, at the cost of the alignment precision. On the other hand, non-rigid registration methods have many more degrees of freedom which might provide a more precise alignment at the cost of a limited computational performance. Many different methods have been proposed to cope with the non-rigid registration problem providing a certain degree of precision. The most commonly used methods in medical image registration are the ones based on Free Form Deformations (FFD) with B-Splines [1], Demons [2], and Symmetric Normalization (SyN) [3]. FFD methods normally deform B-Splines basis functions over a grid of control points to obtain the registration. Due to its demanding computational complexity, subsampling is often applied to this registration method, resulting in a lower resolution for the registration. On the other hand the Demons method is dense and more efficient in its original formulation, which is applied on images of same image modality and contrast. Similarly the SyN method was also developed for a dense, same contrast registration providing a diffeomorphic and symmetric formulation for the spatial transformation. For the more general case of multi-contrast or inter-modality registration the aforementioned methods have to be combined with similarity criteria such as Mutual Information (MI) that can drive the registration even in such cases. The drawback of the integration of the MI in such methods is that it has to be estimated many times per iteration, resulting in a drastic effect on the time performance.

The purpose of this work is to introduce a new registration method based on statistical analysis with the objective to reach a spatial precision comparable with the current state-of-the-art methods at a smaller computational cost. A Bayesian formulation is implemented and provides an estimation of the spatial registration by firstly restoring the join intensity statistics with a Wiener filter and then back-projecting the result to the spatial domain. The focus of the proposed method is to cope with non-rigid registration of medical images in the more general case of images with different contrast. The proposed method is able to compensate displacements that are smaller than the size of the considered Region Of Interest (ROI). The proposed method also preserves the form of the joint intensity histogram, which gives it an approximate volume preservation property [4].

1.1 Thesis Outline

This thesis is structured in 5 chapters. In Chapter 2 are introduced the concepts relative to medical imaging and image registration, starting with the difference between linear and non-linear transformations. Section 2.1 introduce some of the most commonly used imaging techniques in medicine with a particular focus on Magnetic Resonance Imaging (MRI) and Computed Tomography (CT). Section 2.2 presents some of the most popular transformation models used for medical image registration. In Section 2.3 different registration approaches are categorized into feature-based or intensity-based methods. Literature on Demons, SyN, and B-Splines methods, as well as other transformation models are also discussed in Section 2.4. Literature has been selected with a particular focus on the application to medical image analysis. Section 2.5 introduces metrics such as Sum of Square Differences (SSD), Cross Correlation (CC), and Mutual Information (MI) and Section 2.6 introduces the optimization of image registration methods presenting the most common techniques. Finally, Section 2.8 introduce some non-parametric signal processing methods for image restoration such as the Wiener filter. In this work the Wiener filter is applied to the joint statistics to guide the image registration.

In Chapter 3 the new Non-Parametric Bayesian Registration (NParBR) method is presented. A general overview of the method is provided in Section 3.1. The theoretical part regarding the Bayesian estimation of smooth spatial transformations is introduced in Sections 3.2 to 3.5. The implementation of the method is introduced in Section 3.6. An analytical estimation of the computational cost of the NParBR method compared with some commonly used registration methods such as SyN and B-Splines is provided in Section 3.7. In Section 3.8 the calculation of an intra-patient atlas for Dynamic Contrast Enhanced - Magnetic Resonance Imaging (DCE-MRI) datasets to cope with the possible bias of the results is presented.

In Chapter 4 the new image registration method is applied to medical images. In Section 4.1 are defined the validation criteria used in this work. In Section 4.2 three different brain phantoms are presented and compared with the results of the state-of-the-art image registration methods. In Section 4.3 the case of Brain MRI registration is presented for the same contrast as well as different contrast images. In Section 4.4, DCE-MRI datasets are also co-registered and Section 4.5 the proposed method is applied to the EMPIRE10 benchmark for image registration methods.

Finally, in Chapter 5 are the summary and the conclusion of this work including a discussion for possible future evolutions and applications of the proposed method.

Chapter 2

Background on Organ Level Medical Imaging and Image Registration

2.1 Medical Imaging

Direct visual analysis of internal organs can be difficult or either impossible due to the invasiveness of such analysis. Therefore, different techniques and technologies for medical imaging have been developed in the modern era. Early medical imaging techniques used an X-ray source to show the bones in-vivo. These techniques have been evolved to represent also different tissue types. Some examples of such techniques include the Computed Tomography (CT), which allows to scan a 3D volume and is used to investigate the internal anatomy of a body, the Positron Emission Tomography (PET), which provides functional information about metabolic processes of the internal organs after the injection of a radionuclide, and the Single-Photon Emission Computed Tomography (SPECT), which provides information relative to the biological activity inside a 3D volume after the injection of a radionuclide. The main drawback of such techniques are the ionizing radiations that the source emits and that can affect also the healthy tissues that are investigated. Ultrasound imaging is an alternative medical imaging technique that uses ultrasound waves that are reflected by different tissue types. The signal produced by the reflection of the ultrasound waves is detected and reconstructed to form an image. The advantage of this technique is that ionizing radiations are not involved in the imaging process, but the interpretation of the resulting images is much more operator dependent. To obtain detailed, high resolution images of the internal organs without expose them to ionizing radiations, a technique called Magnetic Resonance Imaging (MRI) has been developed in the past decades. It uses the effect of magnetic fields and radio waves on different biological tissues to reconstruct an image. An evolution of the MRI technique uses also a contrast agent to highlight blood perfusion while investigating organs with tumor lesions. This technique is called Dynamic Contrast Enhanced - Magnetic Resonance Imaging (DCE-MRI). In this thesis datasets from MRI, DCE-MRI, and CT techniques are presented.

2.1.1 MRI

Every atom is composed of three fundamental particles: protons, which have a positive charge, neutrons, with no charge, and electrons, which have negative charge. Atoms of a certain element are characterized by the atomic number, which is the number of protons in the nucleus, the atomic weight, which is the sum of protons and neutrons in the nucleus, and the spin, or intrinsic spin angular momentum, that represents the self rotation of each nucleus. The interaction between a nucleus that have a spin and an applied magnetic field is the base of MR techniques. Therefore, all the elements that have a spin can produce an MR signal. For the analysis of tissues in human body with MR, isotopes of many different elements such as $^{1}H,^{13}C,^{17}O,^{19}F,^{23}Na$, or ^{31}P can be used. For the analysis of tissues in human body with MR, the choice of the ^{1}H hydrogen isotope is the most obvious one due to its abundance in water and fat, that compose the major part of a body.

In absence of a magnetic field $\mathbf{B}_0$, the magnetic dipole moment of each proton in a tissue rotates around an axis, the spin vector, which is randomly oriented, producing a vector sum of zero, which means that the resulting macroscopic magnetization is zero, therefore no signal can be detected. When the tissue is placed into a magnetic field $\mathbf{B}_0$, its protons act like bar magnets, making the spin vector of approximately half of the protons to orient themselves parallel (lower energy level) to $\mathbf{B}_0$ and the other half to orient themselves anti-parallel (higher energy level) to $\mathbf{B}_0$. The population difference scales with the field strength $\mathbf{B}_0$. At commonly used MR-systems only about one in a million extra spins align parallel to the $\mathbf{B}_0$ field inducing a net magnetization $\mathbf{M}_0$ pointing in the direction of $\mathbf{B}_0$ (i.e. contribute to the MR signal).

A key feature of NMR is that the resonance frequency of a particular substance is directly proportional to the strength of the applied magnetic field $\mathbf{B}_0$. The rate at which protons precess around the external field $\mathbf{B}_0$ can be defined by the Larmor equation:

$$\omega_0 = \frac{\gamma \mathbf{B}_0}{2\pi} \tag{2.1}$$

where ω_0 is the Larmor frequency, γ is the gyromagnetic ratio, specific for each nucleus. The magnetic field $\mathbf{B}_0$ is measured using the unit Tesla (T). The magnets used in clinical routine normally have values between 0.5T to 3T, which is 10000 to 60000 times stronger than the earth's magnetic field, respectively. The strength of $\mathbf{B}_0$ is directly proportional to the achievable Signal to Noise Ratio (SNR) for an image, therefore much effort have been placed in the development of more powerful superconductive magnets.

The alignment of the protons within the $\mathbf{B}_0$ field can be perturbed by electromagnetic pulses, such as RadioFrequency (RF), irradiated perpendicularly to $\mathbf{B}_0$. The energy of the RF pulses is chosen to be the Larmor frequency at which resonance occurs. Therefore, the protons are excited from the low energy state $E \uparrow = +\frac{1}{2}\gamma\mathbf{B}_0$, called spin-up, to the higher energy state $E \downarrow = -\frac{1}{2}\gamma\mathbf{B}_0$ called spin-down. This creates an energy difference $\Delta E = \frac{h\gamma\mathbf{B}_0}{2\pi}$ that affects the magnetization $\mathbf{M}$ of a tissue

$$\mathbf{M} \approx = \frac{h\gamma\mathbf{B}_0}{4\pi k_B T}, \tag{2.2}$$

where h is the Planck constant, k_B is the Boltzmann constant, and T is the temperature. As a result, the macroscopic magnetization is tilted into the plane perpendicular to the $\mathbf{B}_0$ field. The occurring transversal magnetization rotates in this plane and an AC voltage can be induced in a coil surrounding the measured probe. Once the excitation pulse is turned off, $\mathbf{M}$ aligns back to $\mathbf{B}_0$ as the protons relax back into their lowest energy state within $\mathbf{B}_0$ and give up their energy excess to the surround. Two different interactions can be defined: the spin-lattice and the spin-spin interaction.

The time needed by the protons to pass from an excited state back to the equilibrium is called relaxation time. In MRI the relaxation times that can be measured are known as T_1 and T_2, which differ in the final disposition of the energy. The T_1 is known also as spin-lattice relaxation and describes the energy transfer of the longitudinal component M_z

of a magnetic field **M** towards the 63% of its original value following the equation

$$M_z(t) = M_z(0)(1 - e^{-t/T_1}), \tag{2.3}$$

where t is the time following the RF pulse. Different tissues have different T_1 and consequently produce different signals, which after the reconstruction of the image give different intensity levels whose result in the contrast within the image. For example the T_1 between white matter and gray matter in a brain is significantly different and allows to produce an image where the two tissues are clearly defined and analyzable. T_1 weighted ($T_1 - w$) images are the most commonly used for the examination of the anatomy of different organs in the human and animal bodies.

The T_2 relaxation time is also known as the spin-spin or transverse relaxation time. It is the time required by the transverse component M_{xy} of a magnetic field **M** to decay to 37% of its initial value following the equation

$$M_{xy}(t) = M_{xy}(0)e^{-t/T_2}, \tag{2.4}$$

where $M_{xy,0}$ is the transversal magnetization. T_2 weighted ($T_1 - w$) images have then a different contrast in comparison to $T_1 - w$, highlighting fluids. Both $T_1 - w$ and $T_2 - w$ images are used to investigate the anatomy of the internal organs.

Lesions in some tissues may have similar intensity levels resulting from T_1 and T_2, therefore sophisticated acquisition techniques called pulse sequences are used. A pulse sequence in its most simplistic form combines rf pulses, gradient pulses, data sampling periods and the timing between each of them. This results in the creation of images that have a different contrast when compared to the $T_1 - w$ and $T_2 - w$ images. An example of a pulse sequence created to highlight lesions is the Fluid Attenuated Inversion Recovery (FLAIR), which modifies a $T_1 - w$ images suppressing the effect of the fluids such as the Cerebro-Spinal Fluid (CSF). This sequence has been developed to highlight white matter lesions such as Multiple Sclerosis (MS), which in a normal $T_1 - w$ image would have intensities similar to the white matter, lowering the local contrast resulting in a difficult or either impossible diagnosis. In this thesis an application of the proposed method over $T_1 - w$, $T_2 - w$, and $FLAIR$ images is shown.

In some cases the use of pulse sequences is also not sufficient to create the desired contrast between healthy and diseased tissue. Therefore, a contrast agent can be used to temporally increase the contrast between tissues to perform the scan and consequently gain more information over the considered tissues. One sort of contrast agents for MRI contain one or more paramagnetic metal ions with one or more unpaired electrons and are normally in form of intravenous solution with a relatively small concentration. The small concentration and dosage make the contrast agents for MRI normally well tolerated and safe to use. After their use, they are excreted through the renal system within few hours. The effect of a contrast agent is to shorten T_1 or T_2, making the contrast agent contribute to more signal in the image compared to pure water. This results in a highlight of the tissue that accumulate most the contrast agent. One of the most commonly used contrast agents is a Gadolinium based chelate complex which has been firstly used for neuro-imaging and then extended to other organs. A combination of pulse sequences with the injection of contrast agent can help to quantify and characterize lesions in the internal organs as well as give information about their metabolic state. Active lesions present an abnormal, higher vascularization, which can be highlighted by the injection of a contrast agent. A technique used for the examination of different organs in thorax and pelvis regions is the Dynamic Contrast Enhanced MRI (DCE-MRI), which allows to show the effect of the contrast agent intake on different tissues over time before, during, and after the injection of the contrast agent. Thus, DCE-MRI datasets can provide additional insight on various tissue properties. In this thesis an application of the proposed method on DCE-MRI datasets of liver, lungs, intestines, and prostate is presented. More detailed informations regarding the background on MRI, contrast agents for MRI, and pulse sequences, can be found in [5–7].

2.1.2 CT

X-ray based imaging allow to represent internal parts of a body as a 2D image. The main disadvantage is that a single 2D projection of an organ may produce an image in which different structures overlap and are consequently difficult to distinguish. In 1972 Sir Godfrey N. Hounsfield presented the first CT scanner, which can image internal body structures from different angles and reconstruct the resulting images in a 3D volume. CT scanners use an X-ray beam and a series of detectors to detect the local X-ray attenuation of a body placed between the X-ray source and the detectors. The difference between the intensity of the beam at the source and the intensity of the beam after passing through the body give the total absorption by all the pixels in a line. To determine the absorbed radiation for each pixel in each slice, some reconstruction techniques are used.

The first generation of CT scanners allow to acquire different parallel slices by translating the beam/detector set-up, while the second generation allowed to acquire a small number of slices simultaneously. In the actual third generation of CT scanners an array of hundreds of detectors is placed in an arc which can detect the attenuation of the radiation of a fan beam. Both beam emitter and detectors rotate around the body of the patient to obtain the final volumetric image.

CT scanners are commonly used in the clinical routine to image internal organs for cancer detection and to study its evolution over time. Also for CT the contrast between tissues can be increased by using contrast agents. Normally, the contrast agents used in CT contain substances with a high molecular weight which contribute to increase the attenuation given from the scanned region. Iodine or diluted barium based preparations are the most commonly used contrast agents for CT and can be either injected or drank, depending on the examination. CT images are also used for radiotherapy planning or for 3D reconstruction of complex internal body structures such as the internal ear or intestines.

The advantages of the CT are a good resolution and the velocity of the acquisition, which can be in order of few seconds which help to minimize motion artifacts. Without the use of a contrast agent the contrast of internal tissues, however, can be poor in comparison to MRI images. Intravenous contrast agents for CT are also less tolerated in comparison to the MRI contrast agents. Finally, the main disadvantage of CT is that it uses ionizing radiation, which can be relatively high and affect healthy tissues.

In this thesis are presented CT images from the EMPIRE10 challenge [8] which are used to evaluate the proposed method. More detailed explanations about CT techniques can be found in [9–11]

2.2 Medical Image Registration

The alignment of images is a common problem in many different fields such as satellite data analysis, computer vision, or medical imaging. The process of transforming different images into the same coordinate system is called image registration. Usually the image registration problem is defined with a scheme composed of 4 elements:

1. two input images, I_{ref} and I_{mov}, which are the reference and the moving image of the registration process, respectively. The image I_{mov} is transformed to match the reference image I_{ref},

2. a registration spatial transformation $\mathbf{T} = (u, v, w)$, where u, v, w are the components of the displacement field along the three axes, which is estimated from I_{ref} to I_{mov}. The transformation $\mathbf{T}$ is then inversely applied to I_{mov} to obtain a registered image $I_{reg} = I_{mov}(\mathbf{T}^{-1}(\mathbf{x}))$ where $\mathbf{x} = (x, y, z)$ are the spatial coordinates, which results in an approximation of I_{ref},

3. a similarity metric, which provides a qualitative value of the transformation and the fit quality between I_{ref} and I_{mov},

4. an optimizer, which allows to find the optimal transformation $\mathbf{T}$.

The spatial transformations $\mathbf{T}$ are of two main categories: linear and non-linear. The linear transformations can be also divided in two sub categories: rigid and affine. In Fig. 2-1 examples of linear and non-linear transformations are shown.

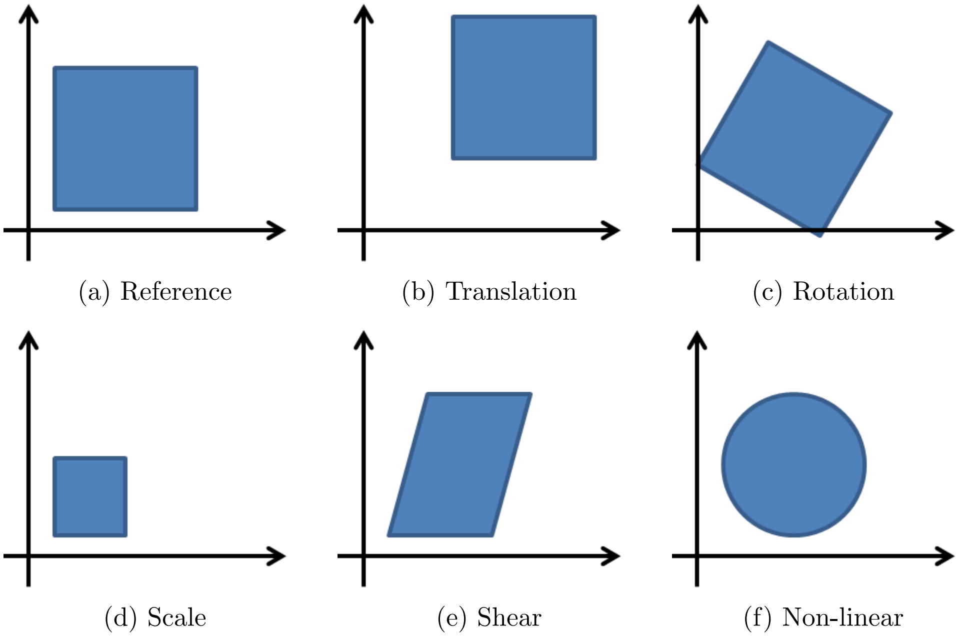
(a) Reference
(b) Translation
(c) Rotation
(d) Scale
(e) Shear
(f) Non-linear

Figure 2-1: Example of linear and non-linear transformations. (a) is the reference image, (b)-(e) are the linear affine transformations, and (f) is an example of a non-linear transformation.

2.2.1 Linear Transformations

The simplest linear transformations are rigid transformations which consist of translations and rotations [12]. Rigid transformations are a subset of the more general affine transformations, which additionally include scale and shear. Each point $\mathbf{x} = (x_1, x_2, x_3)$ in a 3D image I, can be transformed with an affine mapping into another coordinate space $\mathbf{y} = (y_1, y_2, y_3)$ represented by a matrix multiplication $\mathbf{y} = \mathbf{M}\mathbf{x}$. Points $\mathbf{x}$ and $\mathbf{y}$ can be also represented in homogeneous coordinates by 4-dimensional vectors $\mathbf{x} = (x_1, x_2, x_3, 1)$ and $\mathbf{y} = (y_1, y_2, y_3, 1)$, respectively:

$$\begin{bmatrix} y_1 \\ y_2 \\ y_3 \\ 1 \end{bmatrix} = \begin{bmatrix} m_{11} & m_{12} & m_{13} & m_{14} \\ m_{21} & m_{22} & m_{23} & m_{24} \\ m_{31} & m_{32} & m_{33} & m_{34} \\ 0 & 0 & 0 & 1 \end{bmatrix} \begin{bmatrix} x_1 \\ x_2 \\ x_3 \\ 1 \end{bmatrix}$$

The simplest transformation is the translation of a point $\mathbf{x}$ by $\mathbf{q}$ units:

$$\mathbf{y} = \mathbf{M}\mathbf{x},$$

that in matrix terms is represented as:

$$\begin{bmatrix} y_1 \\ y_2 \\ y_3 \\ 1 \end{bmatrix} = \begin{bmatrix} 1 & 0 & 0 & q_1 \\ 0 & 1 & 0 & q_2 \\ 0 & 0 & 1 & q_3 \\ 0 & 0 & 0 & 1 \end{bmatrix} \begin{bmatrix} x_1 \\ x_2 \\ x_3 \\ 1 \end{bmatrix}$$

A rotation is a transformation that can be described by a single angle in the two dimensional case. In three dimensions, rotations can be described by three Euler angles α, β, γ about three orthogonal rotation axes. The pitch α is a rotation about the x axis, and it can be formalized in matrix form as:

$$\begin{bmatrix} y_1 \\ y_2 \\ y_3 \\ 1 \end{bmatrix} = \begin{bmatrix} 1 & 0 & 0 & 0 \\ 0 & cos(\alpha) & sin(\alpha) & 0 \\ 0 & -sin(\alpha) & cos(\alpha) & 0 \\ 0 & 0 & 0 & 1 \end{bmatrix} \begin{bmatrix} x_1 \\ x_2 \\ x_3 \\ 1 \end{bmatrix}.$$

Similarly, the roll β around the y axis is written as:

$$\begin{bmatrix} y_1 \\ y_2 \\ y_3 \\ 1 \end{bmatrix} = \begin{bmatrix} cos(\beta) & 0 & sin(\beta) & 0 \\ 0 & 1 & 0 & 0 \\ -sin(\beta) & 0 & cos(\beta) & 0 \\ 0 & 0 & 0 & 1 \end{bmatrix} \begin{bmatrix} x_1 \\ x_2 \\ x_3 \\ 1 \end{bmatrix}$$

and the yaw γ around the z axis:

$$\begin{bmatrix} y_1 \\ y_2 \\ y_3 \\ 1 \end{bmatrix} = \begin{bmatrix} cos(\gamma) & sin(\gamma) & 0 & 0 \\ -sin(\gamma) & cos(\gamma) & 0 & 0 \\ 0 & 0 & 1 & 0 \\ 0 & 0 & 0 & 1 \end{bmatrix} \begin{bmatrix} x_1 \\ x_2 \\ x_3 \\ 1 \end{bmatrix}.$$

Rotations can be combined by multiplying the rotation matrices in the appropriate order, which is not commutative. Translations and rotations can describe only pure rigid-body mappings. To change the size of an image, a scaling transformation has to been introduced. It allows to modify the size of an image by a factor $\mathbf{s} = (s_1, s_2, s_3)$ either isotropically, if $s_1 = s_2 = s_3$, or anisotropically in the other cases. The scaling can be represented as:

$$\begin{bmatrix} y_1 \\ y_2 \\ y_3 \\ 1 \end{bmatrix} = \begin{bmatrix} s_1 & 0 & 0 & 0 \\ 0 & s_2 & 0 & 0 \\ 0 & 0 & s_3 & 0 \\ 0 & 0 & 0 & 1 \end{bmatrix} \begin{bmatrix} x_1 \\ x_2 \\ x_3 \\ 1 \end{bmatrix}.$$

The last transformation that complete the affine set of transformations is the shear. It is defined as the translation along an axis (e.g. the x axis) by an amount that increases linearly with another axis (y). In the three dimensional case the xy shear can be written considering shearing parameters sh_x, sh_y in the following manner:

$$\begin{bmatrix} y_1 \\ y_2 \\ y_3 \\ 1 \end{bmatrix} = \begin{bmatrix} 1 & 0 & sh_x & 0 \\ 0 & 1 & sh_y & 0 \\ 0 & 0 & 1 & 0 \\ 0 & 0 & 0 & 1 \end{bmatrix} \begin{bmatrix} x_1 \\ x_2 \\ x_3 \\ 1 \end{bmatrix},$$

the shear xz is written using parameters sh_x and sh_z

$$\begin{bmatrix} y_1 \\ y_2 \\ y_3 \\ 1 \end{bmatrix} = \begin{bmatrix} 1 & sh_x & 0 & 0 \\ 0 & 1 & 0 & 0 \\ 0 & sh_z & 1 & 0 \\ 0 & 0 & 0 & 1 \end{bmatrix} \begin{bmatrix} x_1 \\ x_2 \\ x_3 \\ 1 \end{bmatrix},$$

and finally the shear yz is

$$\begin{bmatrix} y_1 \\ y_2 \\ y_3 \\ 1 \end{bmatrix} = \begin{bmatrix} 1 & 0 & 0 & 0 \\ sh_y & 1 & 0 & 0 \\ sh_z & 0 & 1 & 0 \\ 0 & 0 & 0 & 1 \end{bmatrix} \begin{bmatrix} x_1 \\ x_2 \\ x_3 \\ 1 \end{bmatrix}.$$

Affine transformations are described by 12 parameters: 3 translations, 3 rotations, 3 scales and 3 shears. These parameters are applied to every position of an image to map it to a second image, making linear transformations global. In general, a transformation model has the purpose to increase the similarity between two images by moving image features and estimate some missing information using the interpolation between image features.

2.2.2 Non-linear Transformations

Non-linear transformations, also named non-rigid transformations, by definition translate into a possible local warping of image features. Thus, a non-linear transformation can deform an image with many degrees of freedom. Some examples of non-linear transformations are the dilation (or stretch), the contraction (or shrink) and the twist. Because of their highly parametric nature, non-rigid transformations are normally not described by transformation matrices as for the linear case.

Non-rigid transformations can be subdivided into two categories: physically based models and function representations [13]. The physically based models can be subdivided in two main subcategories: elasticity and fluid flow. Function representations use the expansion of basis functions such as B-Splines, wavelets, radial basis functions to model the deformation. Transformations models such as radial basis functions, elastic and fluid models are presented by Zitova and Flusser in their general review of image registration methods [14].

Recently Klein et. al [15] and Ou et al. [16] published surveys over the evaluation of different non-linear registration methods applied on human brain datasets. In these works are explained the different deformation approaches of the most popular non-rigid registration methods which are applied to public human brain datasets.

2.3 Registration Approaches

Image registration methods can be mainly categorized in two classes depending on the approach used to estimate the transformations: feature based and intensity based methods.

2.3.1 Feature Based Registration

Some image registration methods use a geometric or feature-based approach. An overview of feature-based registration methods can be found in [14,17,18]. The prerequisite of such methods is the definition of a significant number of features such as landmarks, curves, or surfaces which have to be aligned to obtain the resulting registered image. Typically feature-based registration methods are composed of three steps:

- definition of features such as landmarks and surfaces,
- matching of I_{ref} and I_{mov} surfaces,
- extension of the transformation to the full volume.

Landmarks are assumed to describe meaningful locations on the image and can be defined either geometrically or anatomically in case of medical image registration. The extraction of the appropriate landmarks is an open topic of research and is the main problem of feature-based approaches. One of the most popular methods for feature extraction is the Scale Invariant Feature Transform (SIFT) proposed by Lowe [19,20]. It is based on a scale-space representation in which the local minima/maxima correspond to the feature points of the considered image. This method has been extended and a comparison between SIFT and some of its extensions can be found in [21]. A survey about edge detection methods and their evaluation can be found in [22]. An exhaustive overview of methods for corner detection is given in [23].

The consecutive step of matching the landmarks can be obtained with interpolation. The major drawback of feature matching using interpolation is the lack of accuracy that the interpolation can cause when the distance between features grows, resulting in a possibly inaccurate registration. Features can be matched by using descriptor distance approaches such as thresholding, closest candidate, or taking into account the distance with the nearest and the second nearest neighbor in the feature space [18]. These approaches are intuitive and efficient with the main drawback of losing information regarding the spatial location of the feature points. An alternative category of matching is performed through geometric constraints. The problem is formulated as graph matching and can be solved using pairwise constraints [24–26]. This approach has been used in many applications even if the pairwise constraints can model a limited amount of relations.

The interpolated correspondence between pairs of similar image features typically define the transformation between two images I_{ref} and I_{mov}. Due to the relatively small amount of features that have to be registered, feature-based methods are generally very efficient and suitable for real-time application. Feature-based methods are also robust in case of large deformations. On the other hand, the resulting registration may be qualitatively limited due to the lack of density in features which can locally affect the resulting registration.

In medical imaging, different feature-based registration methods have been proposed. The method of Rohr et al. [27] provides a detection of different landmark types such as point landmarks as well as arbitrary edge points, matches the landmarks with an approximation of thin-plate splines, and performs an elastic registration. This method has been applied in 2D and 3D CT images of the human brain. Shen and Davatzikos proposed a hierarchical feature-based registration approach called HAMMER [28] which uses geometric moment invariants calculated on the tissue maps to reflect the underlying anatomy at different scales. To reduce the presence of local minima, the HAMMER method uses a sequence of successive approximations of the energy function optimized by lower dimensional smooth energy functions. This method has been applied for the registration of 3D MRI images of human brains to construct an average brain image. In Fig. 2-2 an example of the application of HAMMER to 18 different human brain datasets to obtain a brain atlas is shown. Recently, a method of Wu et al. [29] based on feature-based groupwise registration outperformed the HAMMER method in the creation of a human brain atlas. This method estimates the transformation fields for all the subjects simultaneously while minimizing the intersubject differences of anatomical structures using an energy function. The correspondences between voxels to other locations in the images are propagated with thin-plate splines. A more detailed overview of feature-based image registration methods is provided in [14, 17, 18].

2.3.2 Intensity Based Methods

Intensity-based registration methods do not need any geometric knowledge to perform the registration. These methods estimate a geometrical transformation from a similarity crite-

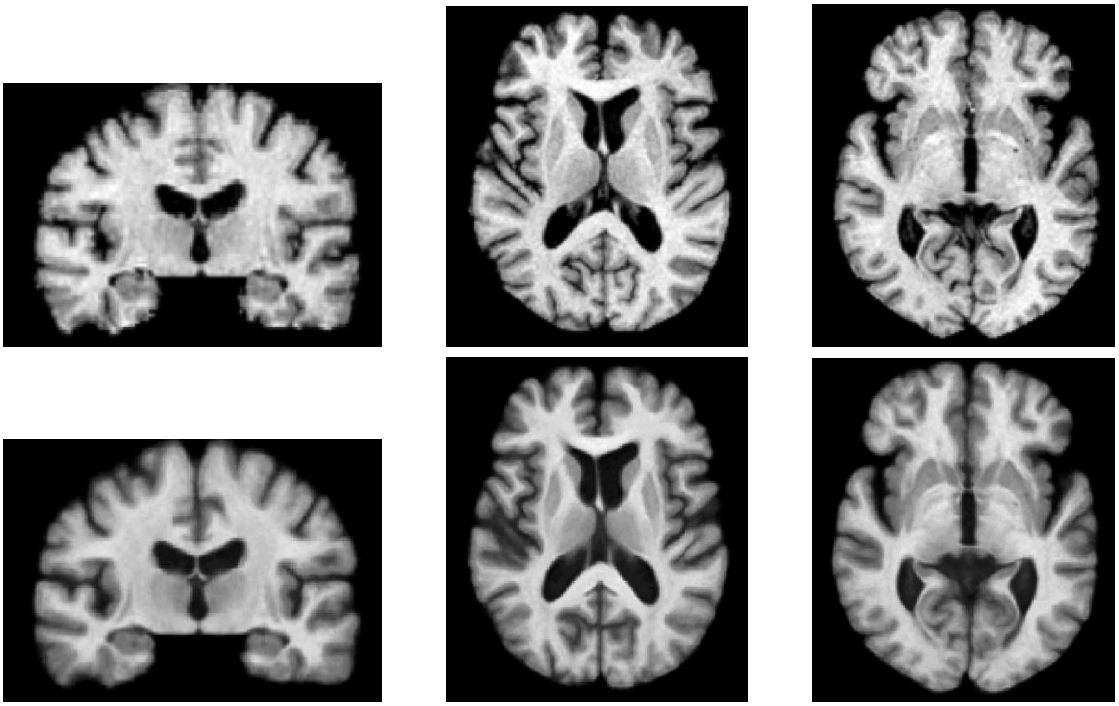

Figure 2-2: Results of application of the HAMMER method to 18 different human brain datasets to obtain a human brain atlas. In the first row are slices taken from the template image and in the second row are the same slices resulting from the application of the HAMMER method. The figure has been taken from [28].

rion until reaching the optimum. Intensity based registration methods have become very popular, in particular in the medical field where they are used to perform mono-modal as well as multi-modal registration. The choice of the appropriate similarity criterion is a fundamental task for intensity-based registration methods. To perform a mono-modal registration, similarity criteria such as SSD or CC can be used. Some literature regarding mono-modal registration using SSD and CC is provided in Section 2.5.1 and Section 2.5.2 respectively. The more general case of the multi-modal registration can be approached in different ways such as reducing the multi-modal registration problem to a mono-modal one as well as selecting information theoretic similarity criteria.

The reduction from multi-modal to mono-modal registration has the objective to simplify the registration problem and to facilitate the solution. This approach can be performed by simulating one modality from another. Roche et al. [30] estimate Ultra Sound (US) intensities from MR intensities and MR gradient magnitude to perform a rigid registration using the correlation ratio method. Wein et al. [31] estimate US from Computed Tomography

(CT) images and perform an affine registration for image guided intervention. Alternatively the problem can be approached by mapping two different imaging modalities to a common space and then perform the registration. Maintz et al. [32] used morphological tools over CT-MR, SPECT-MR, and PET-MR images to create new images in a common space and rigidly register them using CC. Heinrich et al. [33] introduce a Modality Independent Neighborhood Descriptor (MIND) which extracts descriptive structures in a local neighborhood that are preserved across modalities and perform rigid as well as non-rigid registration of CT-MR of human lungs using the SyN method [3].

To cope with the complex problem of multi-modal registration, many methods also used similarity criteria derived from information theory. The most popular similarity criterion is the MI, firstly used in medical imaging by Wells et al. [34, 35] and Maes et al. [36]. The concept of MI together with some significant literature has been presented in Section 2.5.3. An alternative similarity criterion called Correlation Ratio (CR) has been proposed by Roche et al. [37] to drive intensity based registration methods. The CR method can be applied to images that have functional dependency. It has been tested to multi-modal registration of CT, MRI, and PET over human brain datasets. A more detailed overview of intensity based image registration methods is provided in [14, 17, 18].

2.3.3 Miscellaneous Methods

Some hybrid feature/intensity-based registration methods have also been proposed in literature. They try to combine the robustness and efficiency of a feature-based algorithm with the precision that an intensity-based method can reach, trying also to reduce the probability to be trapped in a local minimum. One of the most popular methods in this category is the DRAMMS method from Ou et al. [38], which extracts a rich set of optimal attributes at each voxel and weights all voxels during the optimization process based on mutual-saliency measure. This method has been used to register 3D MRI images of human brains to construct a human brain atlas. In Fig. 2-3 an example of the application of the DRAMMS method for the creation of a human brain atlas is given. Another popular hybrid registration method has been proposed by Hellier and Barillot [39]. This method combines the extraction and registration of human brain cortical sulci features with an optical flow based registration method to create human brain atlases. Sotiras et al. [40] present a method which simultaneously estimates the correspondences between two landmarks sets and a dense displacement field that maps one image space to another using cubic B-Splines. A more detailed overview of hybrid image registration methods is provided in [14, 17, 18].

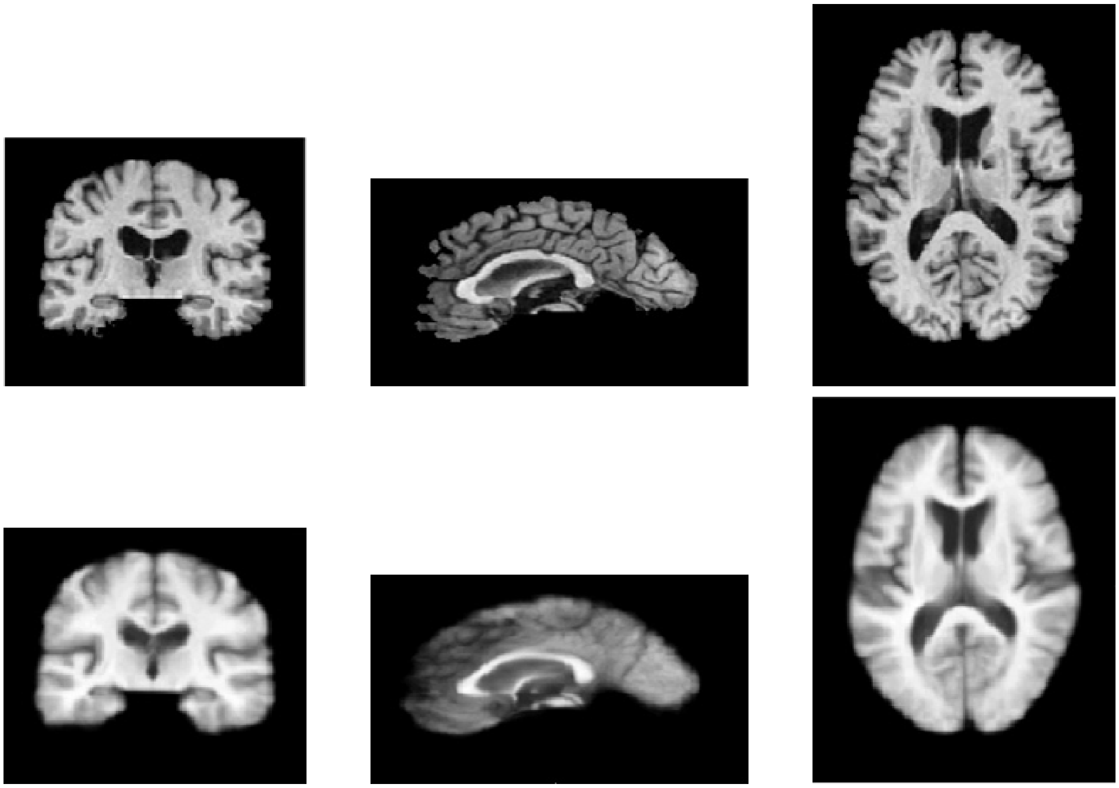

Figure 2-3: Results of application of the DRAMMS method to 30 different human brain datasets to obtain a human brain atlas. In the first line is the template and in the second line is the result of the average image obtained with DRAMMS. The figure has been taken from [38].

Image registration methods based on evolutionary computation and other metaheuristics have also been proposed. These methods are parametric and perform an optimization over a significant number of parameters to possibly reach a global solution. This makes the aforementioned methods more robust against local minima solutions, but, in general, this translates into a considerable computational cost. Many different evolutionary computation and metaheuristics based methods have been proposed. A comparative overview of the most popular methods can be found in [41], where the methods are tested on 3D BrainWeb brain MRI datasets [42] and on CT images of human wrists.

2.4 Transformation Models for Non-rigid Registration

A transformation model describes the transformations between two images. In the first part of this chapter some linear transformations such as rigid and affine have been introduced. These approaches can generally model a coarse transformation with an efficient computational time. On the other hand, non-linear transformations need to be modeled with more complex descriptors, which result in a finer and local estimation of the transformations that can be computationally intense. The compromise between richness of description and computational complexity has to be chosen depending on the context of application. Transformation models can be divided into three main categories [18]: physical models, models inspired by interpolation and approximation theory, and knowledge based models. In this section are presented some of the most common non-linear transformation models used in medical image registration such as the optical flow, Demons, and SyN methods for the physical models, the FFD models with B-Splines for the interpolation models, statistical based methods for the knowledge based models, and finally miscellaneous methods such as graph based registration. More comprehensive literature regarding the transformation models for non-rigid registration can be found in [13, 14, 17, 18].

2.4.1 B-Splines

Transformation models inspired by interpolation or approximation theories assume a known transformation in a restricted area that is then extended with interpolation techniques to the rest of the image. These models also assume the presence of errors in the estimation of a transformation which is then smoothed with an approximation technique. Some of the most important sub-categories of these models are: piecewise affine models, radial basis functions, basis functions from signal processing, elastic body splines and FFD. This section is focused on FFDs which can be used to model B-Splines because of their popular use in medical image registration. A more comprehensive overview of transformation models inspired by interpolation and approximation theories can be found in [18].

For medical image registration the combination of FFDs and cubic B-Splines has been originally proposed by Rueckert at al. [1]. A transformation $\mathbf{T}$ is modeled by a combination of global and local transformations

$$\mathbf{T}(\mathbf{x}) = \mathbf{T}_{global}(\mathbf{x}) + \mathbf{T}_{local}(\mathbf{x}). \tag{2.5}$$

$\mathbf{T}_{global}(\mathbf{x})$ can be modeled using linear transformations described in Section 2.2.1 as well as with higher order global transformations. The local transformation is instead modeled by FFDs based on B-Splines applied to a $n_x \times n_y \times n_z$ mesh of control points $\phi_{i,j,k}$ with uniform spacing. The non-linear transformations are estimated by placing a grid of control points over the image and deform the B-Splines basis functions. The estimated local transformation can then be written as

$$\mathbf{T}_{local}(\mathbf{x}) = \sum_{l=0}^{3} \sum_{m=0}^{3} \sum_{n=0}^{3} B_l(u) B_m(v) B_n(w) \phi_{i+l,j+m,k+n}, \tag{2.6}$$

where $i = \lfloor x/n_x \rfloor - 1, j = \lfloor y/n_y \rfloor - 1, k = \lfloor z/n_z \rfloor - 1, u = x/n_x - \lfloor x/n_x \rfloor, v = y/n_y - \lfloor y/n_y \rfloor, w = z/n_z - \lfloor z/n_z \rfloor$, and B_l represents the lth basis function of the B-Spline. The cubic B-Splines are represented by a set of $B_l, l = (0, ..., 3)$ basis functions

$$\begin{aligned} B_0(u) &= (1-u)^3/6 \\ B_1(u) &= (3u^3 - 6u^2 + 4)/6 \\ B_2(u) &= (-3u^3 + 3u^2 + 3u + 1)/6 \\ B_3(u) &= u^3/6. \end{aligned} \tag{2.7}$$

This method uses the NMI as similarity criterion. It has been used to register MR images of human breasts with same as well as with enhanced contrast [1].

The same author extended the B-Splines based method with a topology preservation constraint to produce diffeomorphic deformation fields and tested it on MRI datasets of human brains [43]. Similarly, Rohlfing et al. [44] proposed an extension of the original FFD based method with an incompressibility constraint which aims at preserving the volume of the organs by penalizing the transformations that have a Jacobian determinant different from unity. The method was tested on MRI datasets of human breasts.

Schnabel et al. [45] introduced a different multiresolution approach from the original FFD based method. It applies a coarse-to-fine approach that results in a smoother estimation of the spatial transformations. This method has been applied to register MRI datasets of human brains and livers of same as well as different modalities. Shi et al. [46] proposed a sparse FFD model which assumes that a transformation between images is simpler than the images themselves, therefore a sparse approach can still hold. This method has been tested on MRI images of the human heart. Noblet et al. [47], Modat et al. [48], and Sotiras and Paragios [49] presented a symmetric extension of the FFD based method tested on MRI datasets of human brains. Peperidis et al. [50] extended the use of the B-Splines also to time series to register series of MR images of human hearts. They proposed a method to optimize the spatial and temporal transformation components simultaneously as well as a method to obtain the same optimization consecutively. Similarly, Ledesma-Carbayo et al. [51] and Vandemeulebroucke et al. [52] proposed methods to cope with spatial as well temporal transformation for ultrasound cardiac registration and for CT image series of the lungs, respectively. Metz et al. [53] also extended the B-Splines based registration method to cope with temporal series of images. This is obtained by introducing an extension of the SSD similarity criterion which takes into consideration also the time component by averaging the intensities over time. This method has been tested on synthetic 3D+time CT images of lungs as well as on CT 3D+time CT images of the human heart.

2.4.2 Optical Flow

The optical flow can be defined as the displacement field that describes the pixel shift between two images [54]. The optical flow calculates the apparent motion within a series of images I taken at different time points t and $t + \delta t$. This method has been described and firstly applied to digital images by Horn and Schunk [55,56] and by Lucas and Kanade [57]. The motion is described by a motion field, which assigns a velocity vector to every voxel in the image. A velocity vector describes the displacement of a voxel in a period of time between consecutive frames

$$\vec{\mathbf{v}} = (u, v) = \left(\frac{\delta x}{\delta t}, \frac{\delta y}{\delta t} \right). \tag{2.8}$$

The optical flow describes the displacement of a voxel of intensity $I(x, y, t)$ by $\delta x, \delta y$ in time δt to $I(x + \delta x, y + \delta y, t + \delta t)$. The preservation of the intensities in space and time between the two images implies

$$I(x, y, t) = I(x + \delta x, y + \delta y, t + \delta t), \tag{2.9}$$

which is the basis of the motion constraint equation. The first order Taylor series expansion around (x, y, t) in Eq. (2.9) gives:

$$I(x + \delta x, y + \delta y, t + \delta t) = I(x, y, t) + \frac{\partial I}{\partial x}\delta x + \frac{\partial I}{\partial y}\delta y + \frac{\partial I}{\partial t}\delta t + H.O.T., \tag{2.10}$$

where $H.O.T.$ are higher order terms that for small displacement estimations can be safely ignored. From Eq. (2.9) and Eq. (2.10) it follows that:

$$\frac{\partial I}{\partial x}\delta x + \frac{\partial I}{\partial y}\delta y + \frac{\partial I}{\partial t}\delta t = 0. \tag{2.11}$$

Using the Einstein notation $I_x = \frac{\partial I}{\partial x}, I_y = \frac{\partial I}{\partial y}, I_t = \frac{\partial I}{\partial t}$ for the partial derivatives of the image intensities at point (x, y, t) and considering the velocity vector field $\vec{\mathbf{v}} = (u, v)$, the optical flow constraint equation becomes more concisely

$$I_x u + I_y v + I_t = 0, \tag{2.12}$$

which expresses a constraint on the components u and v of the optical flow. Eq. (2.12) can be written in vector form as

$$\nabla I \cdot \vec{\mathbf{v}} = -I_t, \tag{2.13}$$

where $\nabla I = (I_x, I_y)$ is the spatial intensity gradient. The component of the optical flow in the direction of the intensity gradient ∇I is

$$-\frac{I_t}{\sqrt{I_x^2 + I_y^2}}. \tag{2.14}$$

This is not able to determine the lateral motion. The resulting ambiguity is also known as aperture problem. This formulation of the optical flow can only completely determine rigid body motion which, in general, is very restrictive. Observing that the motion field varies smoothly in most parts of an image, it is possible to introduce another constraint which minimizes a measure of departure from smoothness. The smoothness constraint originally used by Horn and Schunk [55] minimizes the square of the magnitude of the optical flow velocity $(|\nabla(u)|^2 + |\nabla(v)|^2)$, where u and v are the velocity components of the 2D optical flow. The optical flow energy term that has to be minimized is then given by the regularized constraint described in Eq. (2.12). In the image domain the smooth optical flow estimation is

$$\int\int \left((I_x u + I_y v + I_t)^2 + \lambda(|\nabla(u)|^2 + |\nabla(v)|^2)\right) dxdy, \tag{2.15}$$

where λ weights the relative influence of the smoothness term. An optimum must satisfy the following Euler-Lagrange equations deriving from Eq. (2.15):

$$\begin{aligned} (I_x u + I_y v + I_t)I_x - \lambda \Delta u &= 0 \\ (I_x u + I_y v + I_t)I_y - \lambda \Delta v &= 0. \end{aligned} \tag{2.16}$$

Numerical Solvers such as Successive Over-Relaxation (SOR) can be used to solve the sparse linear system resulting from the discretization of Eq. (2.16) [58]. Starting from a displacement field initialized everywhere to 0, the SOR iteration scheme for minimizing the optical flow energy of Eq. (2.15) is [54]:

$$\begin{aligned} u_i^{k+1} &= (1-\omega)u_i^k + \omega \frac{\sum_{j \in \mathcal{N}^-(i)} u_j^{k+1} + \sum_{j \in \mathcal{N}^+(i)} u_j^k - \frac{1}{\lambda}((I_x I_y)_i v_i^k + ((I_x I_z)_i))}{\sum_{j \in \mathcal{N}^-(i) \cup \sum_{j \in \mathcal{N}^+(i)}} 1 + \frac{1}{\lambda}(I_x^2)_i} \\ v_i^{k+1} &= (1-\omega)v_i^k + \omega \frac{\sum_{j \in \mathcal{N}^-(i)} v_j^{k+1} + \sum_{j \in \mathcal{N}^+(i)} v_j^k - \frac{1}{\lambda}((I_x I_y)_i u_i^{k+1} + ((I_y I_z)_i))}{\sum_{j \in \mathcal{N}^-(i) \cup \sum_{j \in \mathcal{N}^+(i)}} 1 + \frac{1}{\lambda}(I_y^2)_i}, \end{aligned} \tag{2.17}$$

where $\mathcal{N}^-(i)$ denotes the neighboring pixels j of pixel i with $j < i$ and $\mathcal{N}^+(i)$ the neighboring pixels j of pixel i with $j > i$. The scheme converges for the relaxation parameter $\omega \in (0, 2)$. An alternative Gauss-Seidel solver has been used by Horn and Schunk in their original publication [55,56]. Other solvers such as unidirectional and bidirectional multigrid approaches can be used to efficiently minimize the optical flow energy [59]. The optical flow formulation described in this paragraph can directly be extended to 3D space.

The formulation of optical flow given by Horn and Schunk [55] assumes brightness constancy and small displacements. As further constraint it smoothens the flow field with a quadratic regularizer. The brightness assumption has been extended to higher-order constancy by Brox et al. [60] to reduce the effects of illumination change as well as to increase the robustness to noise. The coarse-to-fine strategy has been implemented to cope with displacements that are larger than the local window size. In the same work, an increasing concave function has also been applied to the energy formulation to make it more robust than the original formulation proposed by Horn and Schunk [55]. Brox and Malik [61] proposed a further extension of the optical flow calculation by integrating rich local descriptors into the variational optical flow formulation. Descriptor matching techniques provide an efficient and correct estimation of large displacements while variational techniques efficiently provide highly accurate, dense motion fields without outliers. The combination of such techniques can provide more accurate estimation of large displacements of small structures such as smaller body parts such as hands.

The application of optical flow techniques to the registration of medical images is normally limited by the intensity constancy assumption since, in general, medical images can have different intensities or dynamic ranges even within the same modality due to motion or acquisition artifacts mainly due to detector sensitivities and the reconstruction algorithm. Therefore, some extensions to the original optical flow formulation have been proposed to cope with the more general multicontrast registration problem. Hermosillo et al. [62] proposed an integration of optical flow with different similarity criteria such as cross correlation, correlation ratio, and mutual information. They tested the method on different synthetic images as well as on MRI images of the human brain. Similarly Palos et al. [63] integrate the Horn and Schunk optical flow method with mutual information to register CT and MRI images. Martel et al. [64] also added a term in the optical flow formulation to explicitly cope with the intensity variation which happen in DCE-MRI. In this study the optical flow equation drives a grid of control points to obtain the registration using the NMI as similarity criterion with a multi-resolution approach to register DCE-MRI datasets of human breasts.

2.4.3 Demons Method

One of the most popular physically inspired transformation models has been proposed by Thirion et al. [2]. The Demons method uses the analogy with Maxwell's Demons to perform the registration as a diffusion process modeled by the diffusion equation

$$\Delta \mathbf{u} + \mathbf{F} = 0, \tag{2.18}$$

where $\mathbf{u} = (u, v, w)$ is the displacement field and $\mathbf{F}$ is the force field that drives the registration based on an image matching criterion. In its original formulation, Demons uses the optical flow method from Horn and Schunk [55] to find small deformations in temporal sequences of same contrast images.

The first implementation proposed by Thirion extracts a set of demons D_{ref} from a reference image I_{ref}, where each demon corresponds to a voxel. Each demon contains different information such as:

- the spatial position $\mathbf{x}$ in I_{ref}
- a direction $\vec{d}$ from inside to the outside
- the actual displacement from I_{ref} to the moving image I_{mov} with direction $\vec{d} = \vec{\mathbf{x}\mathbf{x}'}$, where $\mathbf{x}' = T_k^{-1}(\mathbf{x})$ at iteration k
- information about the intensity at location $I_{ref}(\mathbf{x})$

The implementation adopts an iterative scheme and starts from an initial identity transformation T_0. The transformation T_k at iteration k is estimated with two steps:

1. Compute demon force $\vec{f_k}(\mathbf{x})$ for each demon $\mathbf{x} \in D_{ref}$. The force $\vec{f_k}(\mathbf{x})$ depends on the demon direction $\vec{d}$ at point $\mathbf{x}$ and on the polarity of I_{mov} at point $\mathbf{x}'$.
2. Compute T_{k+1} from T_k updated with all elementary demons forces $\left\{\vec{f_k}(\mathbf{x}), \mathbf{x} \in D_{ref}\right\}$.

The transformation model adopted is the FFD that stores every elementary displacement to form a regular displacement field which is smoothed at every iteration using a Gaussian filter and a trilinear interpolation. The demon force is estimated using optical flow described in Section 2.4.2. The original method proposed by Thirion includes also alternative formulation which consider the demons only in contours as well as in already segmented images. The method proposed by Thirion also uses a multi-scale approach and has been tested on synthetic as well as on MRI data of human brains and human heart.

Vercauteren et al. [65] extended the Demons method by introducing the diffeomorphic property. In this case the transformation is estimated and accumulated at every iteration by composition of the transformations resulting from the subsequent iterations. This work has been tested on synthetic human brain data taken from the BrainWeb database [42]. The same group proposed a further extension of the Demons algorithm by introducing the symmetric property [66], where the spatial transformations are represented in the log-domain and forward and backward forces are computed separately. The average of these two forces give the final symmetric displacement estimation. Mansi et al. [67] introduced an incompressibility constraint to register myocardium dynamic-MRI by making the velocity field to be divergence-free and, consequently, limiting the shrinking and sinking effect.

The original Demons method from Thirion as well as its extensions have been used in combination with an SSD similarity criterion. This limited the application of the Demons algorithm to datasets from the same modality and same contrast. To cope with the more general case of different contrasts or different modalities other approaches have been proposed: Guimond et al. [68] proposed an iterative approach that alternates between intensity correction and Demons registration to register images of human brains from the BrainWeb database [42], Modat et al. [69] included the NMI as similarity criterion to perform a multi-modal registration of human brain images from BrainWeb database, and Lu et al. proposed an extension of the Demons method with the integration of the point-wise MI [70] and tested it on human brain images from the BrainWeb database. The same group also proposed a hybrid version of Demons and landmark based registration [71]. This method also integrated MI as similarity criterion and it has been tested on human brain images from the BrainWeb database.

2.4.4 Symmetric Normalization (SyN)

A diffeomorphism can be defined as a differentiable, bijective map whose inverse is differentiable as well. A diffeomorphism ϕ in Ω transforms an image I into a new coordinate system by warping the image by a map defined by $\phi(\mathbf{x}, t)$

$$\phi I = I(\phi(\mathbf{x}, t)), \tag{2.19}$$

where t indicates the time and $\mathbf{x}$ a spatial coordinate. From the definition of diffeomorphism follows that

$$\phi(\phi^{-1}) = \phi^{-1}(\phi) = \mathbf{Id}, \tag{2.20}$$

where $\mathbf{Id}$ is the identity transformation. The correspondence maps ϕ result from the integration of the velocity fields $\mathbf{v}(\mathbf{x}, t)$ in time

$$\phi(\mathbf{x}, 1) = \phi(\mathbf{x}, 0) + \int_0^1 \mathbf{v}(\phi(\mathbf{x}, t), t) dt. \tag{2.21}$$

The velocity field $\mathbf{v}(\mathbf{x}, t)$ can be also regularized using a linear differential operator $L = a\nabla^2 + b\mathbf{Id}$, where a and b are constant, to obtain the distance

$$D(\phi(\mathbf{x}, 0), \phi(\mathbf{x}, 1)) = \int_0^1 \|\mathbf{v}(\mathbf{x}, t)\|_L \, dt. \tag{2.22}$$

The Large Deformation Diffeomorphic Metric Mapping (LDDMM) is a framework that allows to define a distance between images or sets of points [18,72,73], modeling the spatial transformations with flows of diffeomorphisms. An overview of the LDDMM framework and some of its extensions can be found in [18]. The LDDMM framework has been developed to solve large deformation problems providing diffeomorphic transformation which are not symmetric [74]. An evolution of the LDDMM framework has been proposed by Avants et al. [3]. This formulation introduce symmetry properties required for a geodesic connection of two images I_{ref} and I_{mov} in the space of the diffeomorphic transformations and guarantees symmetry regardless of the chosen similarity measure. The symmetry property guarantees than a transformation $\mathbf{T}$ from an image I_{ref} to I_{mov} have its exact inverse in $\mathbf{T}^{-1}$ from I_{mov} to I_{ref}.

A property of the diffeomorphisms that Avants uses in his formulation is that a diffeomorphism ϕ can be separated in two parts ϕ_1 and ϕ_2. The two images I_{ref} and I_{mov} can then equally contribute to the estimation of diffeomorphic transformations. Considering two voxels $\mathbf{x}_{ref}$ and $\mathbf{x}_{mov}$ corresponding to the position of the same anatomy on I_{ref} and I_{mov} respectively, the resulting distances are

$$D(\mathbf{Id}, \phi_1(\mathbf{x}_{ref}, 0.5)) = D(\mathbf{Id}, \phi_2(\mathbf{x}_{mov}, 0.5)). \tag{2.23}$$

Applying Eq. (2.23) to Eq. (2.22) is possible to obtain the symmetric formulation of the distance term that is

$$\int_{t=0}^{0.5} \left\{ \|\mathbf{v}_1(\mathbf{x}, t)\|_L^2 + \|\mathbf{v}_2(\mathbf{x}, t)\|_L^2 \right\} dt. \tag{2.24}$$

The objective of the similarity term is to find ϕ_1 such that $\phi_1(\mathbf{x}, 1) I_{ref} = I_{mov}$. From the definition of diffeomorphism, this assumption can be expanded in

$$\begin{aligned}
&\phi_1(\mathbf{x}_{ref}, 1)I_{ref} = I_{mov}, \\
&\phi_2^{-1}(\phi_1(\mathbf{x}_{ref}, t), 1-t)I_{ref} = I_{mov}, \\
&\phi_2(\phi_2^{-1}(\phi_1(\mathbf{x}_{ref}, t), 1-t)I_{ref} = \phi_2(\mathbf{x}_{mov}, 1-t)I_{mov}, \\
&\phi_1(\mathbf{x}_{ref}, t)I_{ref} = \phi_2(\mathbf{x}_{mov}, 1-t)I_{mov},
\end{aligned} \tag{2.25}$$

which drives to the similarity term

$$|\phi_1(\mathbf{x}_{ref}, t)I_{ref} = \phi_2(\mathbf{x}_{mov}, 1-t)I_{mov}|^2 . \tag{2.26}$$

Eq. (2.24) and (2.26) contribute to form a symmetric energy term E_{sym} that has to be minimized to obtain the estimation of a transformation

$$\begin{aligned}
E_{sym}(I_{ref}, I_{mov}) = inf_{\phi_1} inf_{\phi_2} \int_{t=0}^{0.5} \left\{ \|\mathbf{v}_1(\mathbf{x}, t)\|_L^2 + \|\mathbf{v}_2(\mathbf{x}, t)\|_L^2 \right\} dt \\
+ \int_\Omega |\phi_1(\mathbf{x}_{ref}, t)I_{ref} = \phi_2(\mathbf{x}_{mov}, 1-t)I_{mov}|^2 \, d\Omega
\end{aligned} \tag{2.27}$$

that is the Symmetric Normalization (SyN) solution. This formulation allows different similarity terms to drive the registration. Avants proposed a similarity term based on the concept of Cross Correlation (CC) which is introduced in Section 2.5.2 because of its robustness to illumination, reflectance, as well as inhomogeneities. For every voxel $\mathbf{x}$ a local intensity mean μ is calculated within a spatial neighborhood $\mathcal{N}$. The difference between the two input images I_{ref} and I_{mov} and their respective local means μ_{ref} and μ_{mov} can be written as

$$\begin{aligned}
\bar{I}_{ref}(\mathbf{x}) = I_{ref}(\mathbf{x}) - \mu_{ref}(\mathbf{x}) \\
\bar{I}_{mov}(\mathbf{x}) = I_{mov}(\mathbf{x}) - \mu_{mov}(\mathbf{x}),
\end{aligned} \tag{2.28}$$

which allows to rewrite the CC formula as

$$CC(\bar{I}_{ref}, \bar{I}_{mov}, \mathbf{x}) = \frac{\left\langle \bar{I}_{ref}, \bar{I}_{mov} \right\rangle^2}{\left\langle \bar{I}_{ref} \right\rangle \left\langle \bar{I}_{mov} \right\rangle}. \tag{2.29}$$

Similarly to Eq. (2.27), the new energy term can be rewritten as

$$E_{CC}(\bar{I}_{ref}, \bar{I}_{mov}) = inf_{\phi_1} inf_{\phi_2} \int_{t=0}^{0.5} \left\{ \|\mathbf{v}_1(\mathbf{x},t)\|_L^2 + \|\mathbf{v}_2(\mathbf{x},t)\|_L^2 \right\} dt \\ + \int_\Omega CC(\bar{I}_{ref}, \bar{I}_{mov}, \mathbf{x}) d\Omega \tag{2.30}$$

Other similarity criteria for SyN-based registration have been implemented in the ANTs toolkit [75]. The original SyN method has been tested on intra-modal human brain MRI images of patients with neurodegenerative diseases and on similar images for hippocampus studies of diseased people [76]. It has been validated also on image registration of lungs within the EMPIRE10 challenge [8], where it obtained the best overall result. Therefore, it can be considered as a state-of-the-art image registration method. An example of image registration obtained with the SyN method is in Fig. 2-4.

2.4.5 Statistical Based Methods

Image registration techniques for medical applications must be robust and stable. The robustness of a registration method is achieved when its performance is satisfactory even in presence of deviations of the input images from their assumptions. The stability of a registration method is achieved when small changes in the input images result in small changes in the output. Due to the variability of the internal organs, shapes, and positions, the aforementioned properties are of fundamental importance for an image registration method. The quality of a registration method can be increased by integrating some knowledge regarding the properties and the deformability of the tissues included in the images that have to be registered. This can be achieved using statistical deformation models which can statistically model deformations across a set of subjects to define registration constraints and, consequently, reduce the degrees of freedom and computational time while preserving the robustness of the method.

Some examples of statistical methods for image registration used Principal Component Analysis (PCA) to perform the registration or to support it. Wouters et al. [77] register sets of brain MRI datasets with a viscous fluid algorithm and calculate the PCA based decomposition on the resulting deformation fields. The registration is obtained by adjusting the coefficients of the principal components to obtain a transformation that maximizes the MI. Tang et al. [78] proposed the RABBIT approach, which constructs a statistical deformation model of the human brain using the PCA. This model is then used to efficiently estimate the differences to the individual images and finally use these informations to perform registration using the HAMMER [28] algorithm. The use of an external image registration method for PCA based registration is a common practice since they can be limited by the estimation of the statistical model, which is normally estimated from a relatively small set of subjects, and by the fact that the images used in the learning phase should be representative for the images analyzed.

2.4.6 Miscellaneous

Alternative methods have been proposed for the non-rigid registration: Tang and Chung [79] and So et al. [80, 81] formulate the registration problem as a discrete labeling problem and solved it with a graph-cut algorithm. These methods have been tested on BrainWeb datasets and showed a superior performance compared to FFD, Demons, and linear programming based methods.

2.5 Metrics

A registration metric, also named similarity criteria, quantifies the alignment between two input images. For feature-based registration methods, a simple similarity criterion measures the distance between corresponding landmarks extracted from the two images. The same approach can be used also to measure the similarity of corresponding segmented structures. The main disadvantage of these criteria is that they are able to quantify an alignment of relatively small regions and not of the full image volume.

In intensity based registration approaches the most popular similarity criteria are calculated over two full images to give a more precise quantification of their alignment. In medical image registration the Sum of Squared Differences (SSD) and the Cross Correlation (CC) are normally used for intramodality registration. For intermodality registration, instead, the most popular similarity criteria are the Mutual Information (MI) and the Normalized Mutual Information (NMI) due to their robustness against contrast and modality change.

The joint intensity statistics calculated over two images can be affected by image noise, misregistration and differing point spread of two imaging modalities [82, 83]. Studying the joint intensity statistics can then provide a measure that can quantify the misalignment of two images. In general the joint intensity distributions of two images can be described using an analogy to the ferromagnetic hysteresis [82, 83]. The effect of the misregistration on the joint intensity statistics is a creation of smooth statistics.

A more comprehensive explanation about similarity criteria for image registration is given in [84, 85], where the most popular similarity criteria are presented in detail and evaluated over CT images of a spine phantom [84] and MRI images of human brains [85]. In the following subsection the most popular similarity criteria used for medical image registration are presented.

2.5.1 Sum of Squared Differences (SSD)

A popular similarity criterion used to drive image registration is the SSD. The SSD assumes that the intensity representing the same homologus point $\mathbf{x} = (x, y, z)$ in two images I_1 and I_2 must be the same. The SSD calculated between I_1 and I_2 is defined as

$$SSD(I_1, I_2) = \frac{1}{N} \sum_{\mathbf{x}} (I_1(\mathbf{x}) - I_2(\mathbf{x}))^2, \tag{2.31}$$

where N is the number of considered voxels. The optimal value of the SSD is zero, therefore large SSD values denote a poor match between I_1 and I_2 that can be caused by spatial misalignment as well as other linear changes in the intensity result. Since a difference of intensities between I_1 and I_2 at the same spatial location $\mathbf{x}$ denotes a misalignment, the applicability of the SSD is restricted to images of the same modality and contrast.

In medical image registration the SSD has been used as a metric in different methods. One of the most popular registration methods using the SSD as similarity criterion is the Demons method originally proposed by Thirion et al. [2], later extended by Vercauteren [65, 86]. These methods have been tested on human brain images from BrainWeb database [42]. Andersson et al. proposed a method called FNIRT [87] which has been applied to register intra-modal MRI of human brains to construct an atlas. Other popular image registration methods such as the Free Form Deformation (FFD) registration proposed by Rueckert et al. [1] or the SyN method proposed by Avants et al. [3, 75] can be combined with SSD for intra-modal registration.

2.5.2 Cross Correlation

The Cross Correlation (CC) is defined as a measure of similarity of two series as a function of the lag of one relative to the other. It estimates how much two series are correlated. Being I_1, I_2 two images and $\bar{I}_1$, $\bar{I}_2$ the mean intensities of I_1 and I_2, respectively, the CC can be defined as

$$CC(I_1, I_2) = \sum_{\mathbf{x}} I_1(\mathbf{x}) I_2(\mathbf{x} + \mathbf{v}), \tag{2.32}$$

where $\mathbf{v} = (u, v, w)$ is a displacement. In image processing is more common to use the Normalized Cross Correlation (NCC) since it is more robust against contrast changes. It defined as:

$$NCC(I_1, I_2) = \frac{\sum_{\mathbf{x}} (I_1(\mathbf{x} - \bar{I}_1) \cdot (I_2(\mathbf{x}) - \bar{I}_2))}{\sqrt{\sum_{\mathbf{x}} (I_1(\mathbf{x}) - \bar{I}_1)^2 \cdot \sum_{\mathbf{x}} (I_2(\mathbf{x}) - \bar{I}_2)^2}}, \tag{2.33}$$

for every voxel $\mathbf{x}$. The NCC is maximal at the best match between two images I_1 and I_2. The most popular registration method used in combination with CC is the SyN method proposed by Avants et al. [3, 75]. This method has been applied to intramodal registration of MRI datasets of human brains with neurodegenerative diseases such as frontotemporal dementia and Alzheimer's disease. Also the method proposed by Rueckert et al. [1] can be combined with CC. An example of an intramodal brain registration over human brains of patients with frontotemporal dementia using SyN combined with CC is given in Fig. 2-4.

2.5.3 Mutual Information

The Mutual Information (MI) measures the mutual dependence of two random variables, which are the intensities of two images I_1 and I_2 in case of image registration. The MI is defined in terms of Shannon's entropy starting from the marginal probability distribution p of the voxel intensities of an image I_1

$$h(I_1) = \sum p(I_1) \log p(I_1), \tag{2.34}$$

where $h(\cdot)$is the entropy of I_1 in the discrete case. Similarly $h(I_2)$ denotes the entropy for image I_2. The joint entropy between I_1 and I_2 is defined as

$$h(I_1, I_2) = -\sum \sum p(I_1, I_2) \log p(I_1, I_2), \tag{2.35}$$

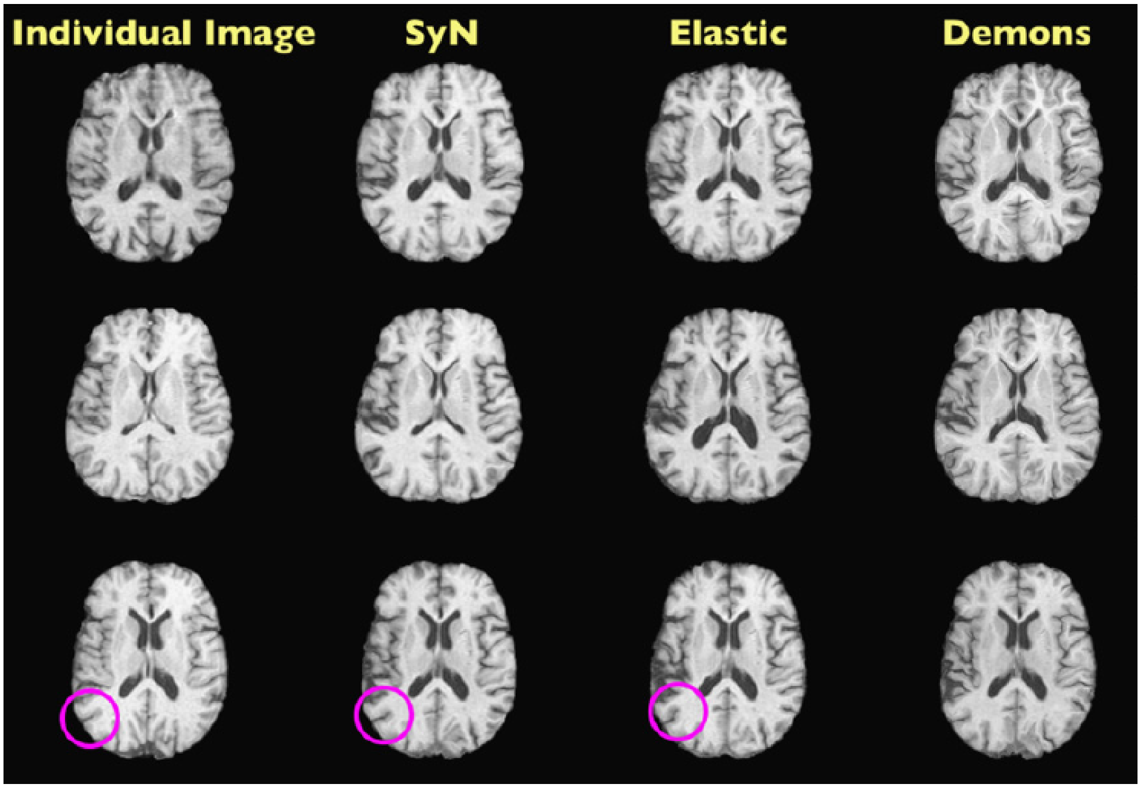

Figure 2-4: Comparison between the results of the SyN method with elastic as well as Demons registration methods. The experiments were performed over human brains of patients with frontotemporal dementia. The figure has been taken from [3].

which measures the entropy contained in a system of two images I_1 and I_2. Using the definitions of entropy and joint entropy of Eq. (2.34) and (2.35), respectively, the MI can be defined as

$$MI(I_1, I_2) = h(I_1) + h(I_2) - h(I_1, I_2), \tag{2.36}$$

which is maximal when the two images are perfectly aligned.

In the last two decades the MI has been increasingly used as a similarity criterion for image registration methods. In particular, MI has been extensively applied to register medical images of different modalities or different contrasts due to its robustness, which let the MI based methods outperform SSD or CC in such applications. The works of Wells et al. [34], Viola et al. [35], Maes et al. [36], and Pluim et al. [88] combined rigid transformations with MI to register intra-patient SPGR MR-T_2 MR, MR-CT, and MR-PET volumetric datasets.

Also non-linear transformations have been combined with MI to obtain a more local and a more precise registration of two images. Some early works have been proposed by Gaens et al. [89] who tested their MI driven method to register artificial as well as real multimodal MR images of the human brain, by Rueckert et al. [1] who applied their non-rigid registration method to breast MR images, and by Hellier and Barillot [90] who proposed a method to non-rigidly register fMRI synthetic as well as human brain data. In the early 2000s registration methods guided by MI have become very popular particularly in the medical imaging field. Mattes et al. [91] propose an MI based method which also integrates a multiresolution approach to reduce the possible local optima solutions in the registration of PET-CT datasets of human chest. Palos et al. [63] combined optical flow techniques with MI to register MR-CT synthetic data. Zöllner et al. [92] integrate B-Splines and the MI formulation of Mattes et al. [91] to register 3D+time Dynamic Contrast Enhanced (DCE)-MRI datasets of human kidneys. Recently, Dimitriev et al. [93] proposed a fully automated method for registering human breast DCE-MRI datasets also using the MI formulation of Mattes et al. [91].

The MI formulated in Eq. (2.36) can increase even in case of an increased misregistration. This behavior has been described from Studholme et al. [94] who identified the property of overlap invariance and proposed a new metric called Normalized Mutual Information (NMI), which is more robust against changes in the overlap of the considered images. The NMI is defined as

$$NMI(I_1, I_2) = \frac{h(I_1) + h(I_2)}{h(I_1, I_2)}. \tag{2.37}$$

The NMI has been used by Schnabel et al. [45] to register intramodality MR images of human brains and livers as well as MR-CT of human brain using a multiresolution approach. Rohlfing et al. [44, 95] proposed a method that uses the NMI as similarity criterion and integrates an incompressibility constraint to register contrast enhanced MR images of human breasts. This method has been subsequently validated by the study of Tanner et al. [96].

An analysis on MI/NMI based registration methods can be found in the work of Maes et al. [97]. A more comprehensive overview on MI based methods have been provided in the work of Pluim et al. [98].

2.5.4 Miscellaneous

Apart of the most popular similarity criteria mentioned above, some others such as the Correlation Ratio [37] or Ratio of Image Uniformity (RIU) [85] have been proposed and used in literature to drive a registration algorithm. A comparison of different similarity criteria for image registration including the aforementioned ones can be found in the works of Penney et al. [84] and Holden et al. [85].

2.6 Optimization

In image registration, optimization strategies are used to obtain the optimal estimation of a transformation between two images I_1 and I_2 according to the transformation model, the regularization, and the similarity criterion chosen. The resulting registration is the one that optimally aligns I_1 and I_2. The nature of the variables that have to be optimized can separate the optimization approaches in continuous and discrete. Optimization methods based on heuristics and metaheuristics can be used to optimize large solution spaces in a wide range of problems. An evaluation of optimization approaches for medical image registration using B-Splines and MI can be found in [99]. An overview of different optimization approaches is given in [18].

2.6.1 Continuous Optimization

Problems that have variables which assume real values and that have a differentiable objective function can be optimized with a continuous optimization strategy. Continuous optimization has been widely applied also to image registration problems where the parameters of a transformation $\mathbf{T}$ can be optimized using an update rule

$$\mathbf{T}_{k+1} = \mathbf{T}_k + \alpha_k \bar{d}_k(\mathbf{T}_k), \tag{2.38}$$

where k is the iteration number, α_k denotes the step size, and $\bar{d}_k$ denotes the search direction which is calculated on the regularized transformation $\mathbf{T}_k$. These methods can be further subdivided in deterministic and stochastic. Some of the most commonly optimization methods used for non-rigid registration include gradient descent, conjugate gradient, quasi-Newton, Gauss-Newton, and Levenberg-Marquardt methods. Some examples of stochastic methods include the stochastic gradient descent and the simulated annealing.

One of the most commonly used continuous optimization method is the gradient descent. The optimization of the objective function in this case is obtained by following the negative gradient

$$\bar{d} = -\nabla \mathbf{T}, \tag{2.39}$$

which results in a decrease of the energy. Gradient descent implementations can differ in the estimation of the step size α, which can be kept constant, vary constantly at each optimization step, or either be estimated at every iteration. One of the most commonly used methods using gradient descent as optimizer is the B-Splines registration method proposed by Rueckert at al. [1]. Similar methods proposed by Tanner et al. [100], Rohlfing et al. [44,95], and Modat et al. [101] also use gradient descent as optimization strategy. The gradient descent optimization has also been applied on a LDDMM framework by Beg et al. [74,102], Avants et al. [3].

An evolution of the gradient descent method is the conjugate gradient, which conjugate the direction $\bar{d}_k$ with the direction $\bar{d}_{k-1}$ using a linear combination l that is

$$\bar{d}_k = l(\nabla_{\mathbf{T}}(\mathbf{T}_k), \bar{d}_{k-1}) = -\nabla_{\mathbf{T}}(\mathbf{T}_k) + \beta_k \bar{d}_{k-1}, \tag{2.40}$$

where β_k is a weighting factor that can be estimated using different methods [103]. Some registration methods that use the conjugate gradient as optimization were proposed by Postelnicu et al. [104], Joshi et al. [105], and Modat et al. [48].

Quasi-Newton optimization methods estimate the inverse Hessian matrix $H^{-1}(\mathbf{T})$, which is used to define the search direction

$$\bar{d} = -\hat{H}^{-1}(\mathbf{T})\nabla_T(\mathbf{T}), \tag{2.41}$$

where $\hat{}$ denotes the approximation of the Hessian matrix. The quasi-Newton optimization method has been used in a multiresolution B-Splines framework proposed by Mattes et al. [91,106]. Other authors such as Song et al. [107], Sance et al. [108], Zöllner et al. [92], and Khader and Hamza [109], used a similar framework to implement a non-rigid registration using the same optimization method.

Introducing a weight ω to the previous optimization approach was a contribution of

Levenberg and Marquardt. The search direction is given by

$$\bar{d} = -(\hat{H}^{-1}(\mathbf{T}) + \mathbf{Id})\nabla_T(\mathbf{T}), \tag{2.42}$$

where **Id** is the identity matrix. Wu et al. [110] used the Levenberg-Marquardt optimizer in a wavelet based registration framework. Ashburner et al. [111] used a Levenberg-Marquardt method to optimize their diffeomorphic registration method DARTEL.

A similar optimization method is the Gauss-Newton algorithm, which approximates the Hessian $\hat{H} = 2J^T J$ without computing second derivatives, using a Jacobian matrix J. The search direction is then given as

$$\bar{d} = -(J^T(\mathbf{T})J(\mathbf{T}))^{-1}\nabla_T(\mathbf{T}). \tag{2.43}$$

This optimizer has been typically used in the Demons registration framework for mono-modality images. Vercauteren et al. [65,66,86] proposed variations of the original Thirion's Demons method using a Gauss-Newton optimization approach. Modat et al. [112] used it into an FFD framework for brain registration.

2.6.2 Discrete Optimization

Problems with variables that assume discrete values can be optimized with discrete optimization techniques. Image registration can also be formulated as a discrete problem using Markov Random Fields (MRF). With this formulation, the MRF is considered as the displacement field that has to be optimized to obtain the registration. Optimization methods such as graph-based and linear programming can be used for optimizing a discrete formulation of the image registration problem.

Efficient methods for discrete optimization include graph-based approaches, which apply a max-flow/min-cut principle over a data structure considered as a graph to optimize an energy. Starting from the maximum a posteriori estimation for binary images proposed by Greig et al. [113], Boykov et al. [114] proposed a multilabel extension of Greig method called α-expansion, which apply the minimum cut at each label at each iteration to obtain the optimal result. This optimization strategy has been used for graph based medical image registration from Tang and Chung [79], Mahapatra et al. [115], So et al. [80,81], Liao and Chung [116].

Linear programming techniques are used to solve an approximation of an originally NP-hard problem. A possible method is the Fast Primal-Dual that was originally proposed by Komodakis et al. [117]. Glocker et al. [118] used the primal-dual approach proposed by Komodakis et al. to obtain an efficient diffeomorphic registration of human brains for the creation of atlases. In this optic, also Sotiras et al. [119] proposed a method for medical image registration and calculation of atlases that is based on linear programming.

2.6.3 Miscellaneous Optimization

Other registration methods based on heuristics can be optimized using greedy approaches as well as evolutionary algorithms. Greedy approaches act on a set of possible solutions usually implemented using a multi-resolution approach that are evaluated using a standard similarity measure. This optimization strategy is often used on feature-based registration methods.

The evolutionary algorithms use an implementation similar to the greedy approaches whose solutions are evolved following an evolution strategy based on mutation. In this case the solutions are evaluated and ranked to obtain a new set of solutions that included an advantageous mutation. More comprehensive literature about evolutionary optimization methods is provided by Santamaria et al. [120].

2.7 Atlas Calculation

Medical imaging atlases record anatomic information about a certain organ or region. This information can then be used for the spatial normalization of images, for statistical analysis of a population, for characterize the progression of a pathology or treatment, and as a segmentation prior.

The registration of image datasets such as intra-patient temporal datasets and inter-patient datasets may introduce a bias in the registration. This is given by the selection of an arbitrary image as reference which may not be representative of the entire dataset. An example can be the registration of DCE-MRI datasets in the abdominal region where the organs are subject to both respiration and contrast change. The registration results then dependent on the selection of the reference image. To avoid this, it is possible to create a more general reference image like an atlas. Inter-patient atlases such as brain atlases can describe common anatomy which can be used as a reference for registration. A widely used inter-patient atlas of the human brain is the BrainWeb database [42].

The simplest atlas is the intensity average image, which can give a smooth result in particular for inter-patient atlases. A less biased result can be obtained by performing a dynamic average, which iteratively register all the images of the dataset to the average image that is recalculated from the resulting registered images at each iteration. The dynamic average assumes that a registration method is performed over an entire dataset, resulting in the creation of a minimally biased atlas. Some registration methods have been developed with the objective to create an atlas of the human brain. Some examples include feature-based registration methods such as the HAMMER method proposed by Shen and Davatzikos [28], the method proposed by Wu et al. [29] based on feature-based groupwise registration, the hybrid feature/intensity based method proposed by Hellier and Barillot [39], the DRAMMS method from Ou et al. [38], and the FNIRT method proposed by Andersson et al. [87]. Also statistical based registration methods have been use to calculate human brain atlases such as the RABBIT method proposed by Tang et al. [78].

For intra-patient temporal datasets of the abdominal organs, a minimally biased reference image can also be obtained by calculating an image including all the possible displacements due to breathing, heart beat or peristalsis. A method developed for the non-rigid registration of DCE-MRI data is the Progressive Principal Component Registration (PPCR) [121]. The method alternates iteratively between the generation of an artificial time series target image using the principal components of the current best registered time series data, and the registration of the time series with the generated images. The effect is to reduce motion artifacts while implicitly preserving the contrast enhancement. The method has been tested on 22 DCE-MRI datasets of the liver and an example of the results are shown in Fig. 2-5. In this work the intra-patient average has been calculated by iteratively refining a time-average of each considered DCE-MRI dataset. The result has been used as reference for the registration of DCE-MRI datasets. Detailed explanation of the atlas calculation method and its implementation is provided in Section 3.8.

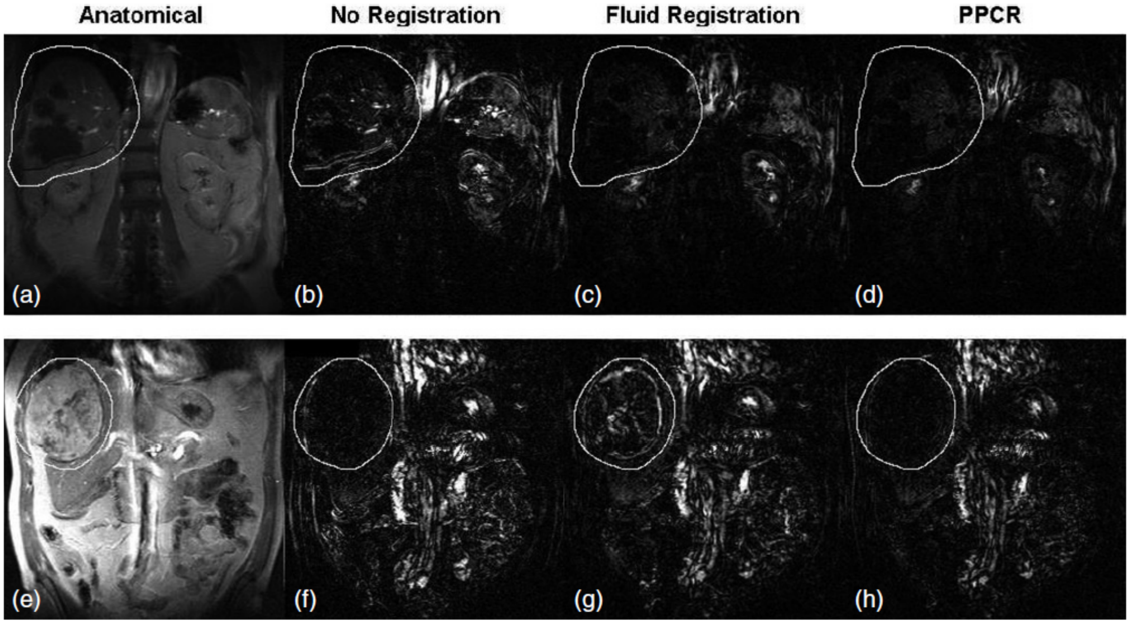

Figure 2-5: Examples of absolute difference images of two datasets [121]. In (a) and (e) are the images used as reference in the respective cases. In (b) and (e) are the absolute difference images without registration. In (c) and (g) are the absolute difference images obtained with fluid registration. In (d) and (h) are the absolute difference images obtained with PPCR method.

2.8 Non Parametric Signal Processing Methods for Image Restoration

Images can often been affected by different types of noise, a poor contrast, variations in intensity or illumination. An image filter transforms pixel intensities to obtain a desired effect such as de-noising, better contrast or sharpening edges. A filter f applied to an image I give as a result a new filtered image I_f in which the pixel intensities have been modified according to the filter used. A commonly used filter in image processing is the Gaussian filter, which can be used to blur the images as well as the displacement fields estimated with an image registration algorithm. Another important filter is the Wiener filter. It is mainly used for the deconvolution of Gaussian noise from images and in this work it has been applied to deconvolve the joint statistics of two misregistered images in order to drive a registration algorithm.

Method	Transformation Model	DoF	Metric	Pros	Cons
Rigid	Translation, Rotation	6	SSD, CC, NCC, MI, NMI	Efficient	Limited DoF
Affine	Rigid, Scale, Shear	12	SSD, CC, NCC, MI, NMI	Efficient	Limited DoF
Optical Flow	Optical Flow	Many	SSD	Dense	Same contrast/modality, small deformations
Demons	Optical Flow	Many	SSD	Dense	Same contrast/modality, small deformations
SyN	Symmetric diffeomorphisms	Many	CC	Dense, Efficient	Same contrast/modality, small deformations
B-Splines	FFD	Many	SSD, CC, NCC, MI, NMI	Large deformations	Subsampling grid, computationally intense with MI/NMI

Table 2.1: Commonly used methods for intensity based medical image registration.

2.8.1 Gaussian Filtering

The Gaussian functions are used in statistics to describe the normal distributions. A typical formulation for a Gaussian function $g(x)$ centered in 0 is:

$$g(x) = \frac{1}{\sqrt{2\pi}\sigma} e^{-\frac{x^2}{2\sigma^2}} \tag{2.44}$$

where σ is the standard deviation.

In image processing, the effect of the application of a Gaussian filter to an image is the absorption of the signal intensities in a pixel to its neighbors, which results in a blurring of the filtered image. The effect of the Gaussian filter is to reduce noise in the filtered image, which comes at cost of blurring detail in the image, resulting in a smooth visual effect. The application of a Gaussian blur to an image is equivalent to convolve the image with a Gaussian function. An example of Gaussian blur is in Fig. 2-6 where are shown the effects of the convolution of the input image with a Gaussian filter of different sizes. The amount of blurring is proportional to the width of the Gaussian filter used in the convolution.

Many image registration methods such as the Demons method (Section 2.4.3) need to regularize their estimation of a spatial transformation. This is to keep the estimated transformation smooth along the iterations by penalizing non-smooth transformations which can be non-realistic, expecially in the case of medical image registration. The most popular regularization term is based indeed on a Gaussian filter. This filter has normally the same dimensionality of the considered images. Due to its significant computational cost particularly when smoothing a dense field, the Gaussian filter is often approximated with a separable implementation where different 1D Gaussian filters are applied in cascade until covering all the dimensions of the images and the relative transformation fields.

2.8.2 Wiener Filtering

In general, images are subject to artifacts of different nature, which can be modeled analytically and also to noise which can depend on the imaging device. A simplified representation for an observed image I_{obs} can be represented as the result of the convolution of an ideal image I_{ideal} with a distortion function g and also an additive noise n:

$$I_{obs} = g * I_{ideal} + n, \tag{2.45}$$

where $*$ is convolution. One of the most common artifacts is the blur. The image can be restored for this artifact with the Wiener filter [122].

The Wiener filter assumes a second order stationarity of signal and noise and also knowledge about the Signal-to-Noise Ratio (SNR), which is the ratio between the Power Spectral Densities (PSD) of the assumed underlying uncorrupted signal I_{obs} and the noise n, $SNR = PSD(I_{obs})/PSD(n)$. The application of the Wiener filter $\mathcal{R}$ to I_{obs} of Eq. (2.45) provides an estimated inverse function that minimizes the MSE between I_{obs} and I_{ideal} which in the Fourier domain is

$$\mathcal{R} = \frac{|\mathcal{G}|}{|\mathcal{G}|^2 + \epsilon}, \tag{2.46}$$

where $\mathcal{G}$ is the Fourier transformation of the function g of Eq. (2.45) that has to be inverted and ϵ is the inverse of the SNR.

In Fig. 2-7 is an example of the application of the Wiener filter to distorted images. In the simplified case of an observed image with Gaussian blur and without noise ($n = 0$), the application of the Wiener filter results in a exact deconvolution of the Gaussian function. In the more general case of an observed image with additive noise, the deconvolution of I_{obs} with a Wiener filter, requires a knowledge or an estimate of the parameter ϵ. In Fig. 2-7a is an example of an observed image with Gaussian blur and no noise and in Fig. 2-7b is the result of its deconvolution with a Wiener filter. In Fig. 2-7c is an example of an image with Gaussian blur and noise which are both deconvolved using a Wiener filter, as shown in Fig. 2-7d.

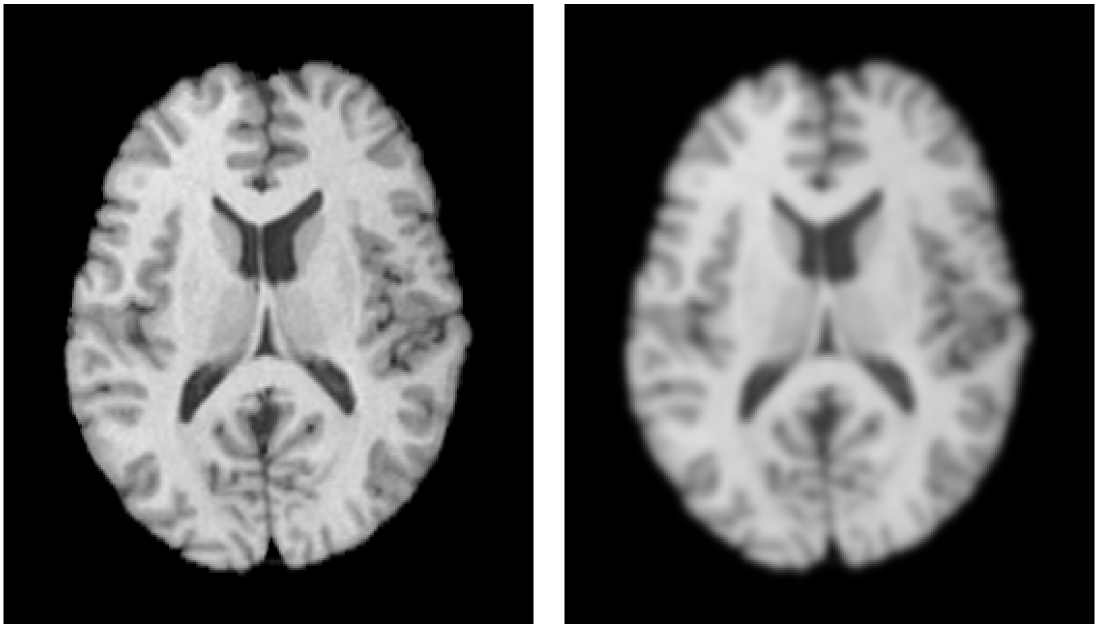

(a) Original (b) $\sigma = 2$

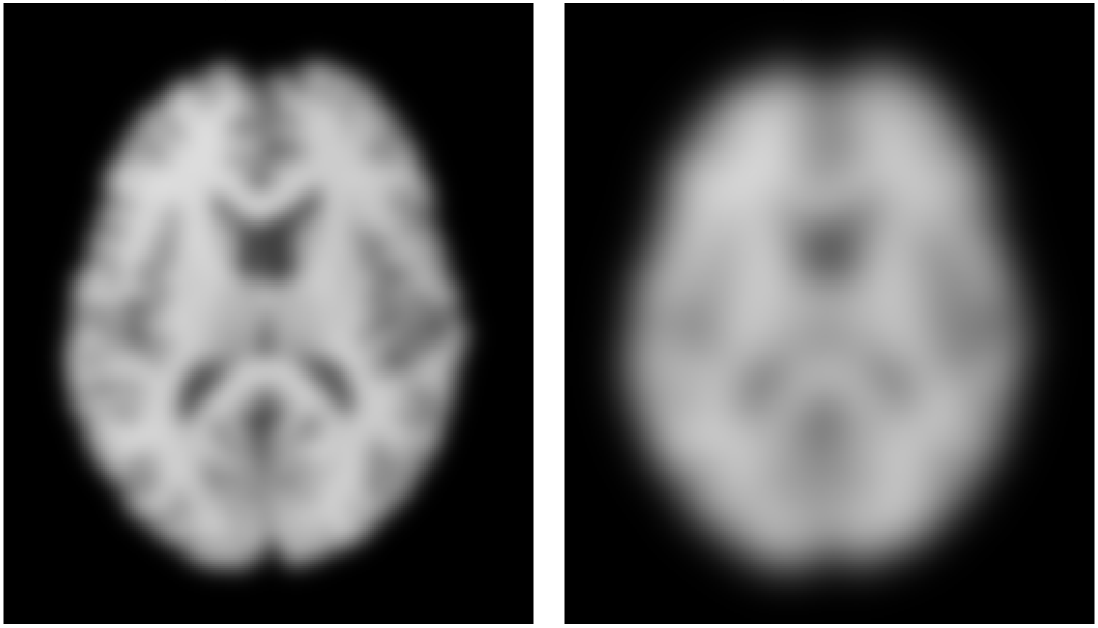

(c) $\sigma = 5$ (d) $\sigma = 10$

Figure 2-6: An example of the application of a Gaussian blur to an image. (a) is the original image and (b), (c), and (d) are the images resulting from the application of a Gaussian filter with $\sigma = 2$, $\sigma = 5$, and $\sigma = 10$, respectively

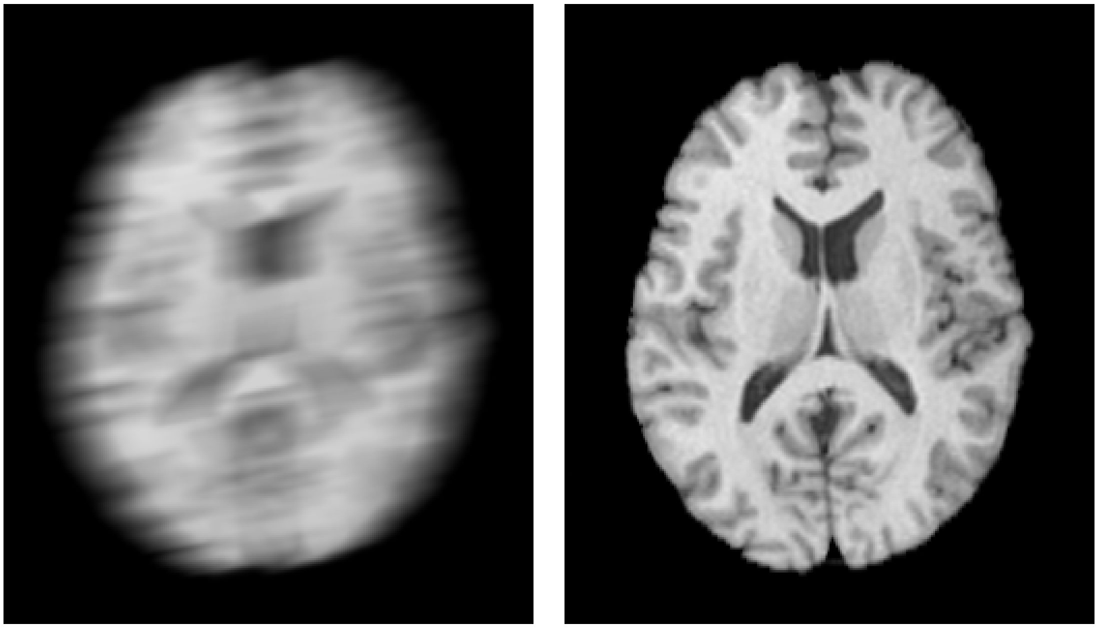

(a) Blur

(b) Wiener deconvolution

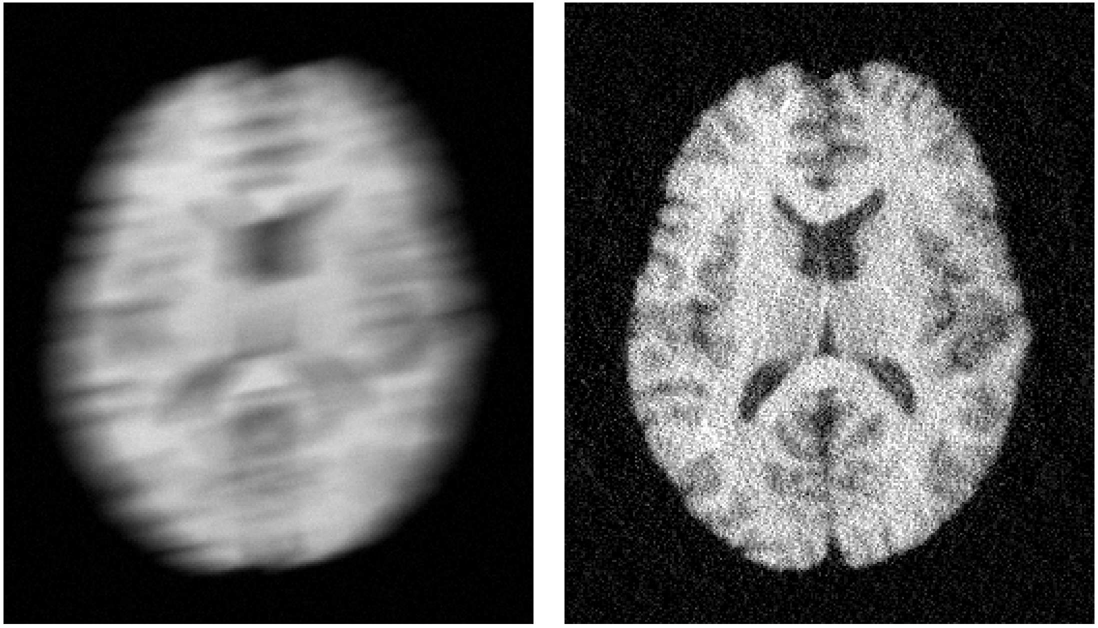

(c) Blur + Noise

(d) Wiener deconvolution

Figure 2-7: An example of the application of a Wiener deconvolution to an image. Figures (b) and (c) have been produced from the original image of Fig. 2-6a convolved with known blur and known blur + noise, respectively. In (b) is the effect of the application of a Wiener deconvolution filter with known convolution filter parameters to (a). In (d) is the effect of the application of a Wiener deconvolution with known convolution filter parameters to (c).

Chapter 3

Non-Parametric Bayesian Registration (NParBR)

In this chapter the Non-Parametric Bayesian Registration (NParBR) method is introduced together with an extensive theoretical formulation and implementation information. The effects of the misregistration are characterized using the joint intensity statistics. The misregistration between two images distorts their joint intensity statistics with a smoothing effect that can be described using an analogy with the ferromagnetic hysteresis [82]. In a typical medical image the intensity variation due to the texture of a tissue region is considered low compared to the tissue contrast. Medical images often contain misregistration and the sizes of the different anatomic structures are large compared to the extent of their misregistration. The boundaries of the regions are also assumed to be smooth due to biological reasons as well as due to the limited resolution in imaging. This smoothness limits the hysteresis effect on the joint distribution and therefore no new distributions beyond noise as well as other imaging artifacts are created. Thus, the effect of the distortion of the joint statistics is assumed to be a local Gaussian smoothing over the domain of the dynamic ranges. In this study the registration is approached as a non-parametric Bayesian statistical restoration. The effect of the spatial misregistration on the joint intensity statistics is represented as the convolution with a Gaussian filter that is used to create both the likelihood and the prior of the registration. The NParBR method in effect restores the joint intensity statistics and also performs a back-projection to the spatial domain to estimate the registration [123, 124].

The non-parametric restoration of the joint intensity statistics removes the effects of the misregistration and also preserves their form. Thus, the resulting continuous spatial registration is approximately also volume-preserving [4]. This is a desired property for many of the datasets analyzed in this work. Some examples are tumor lesions in body organs such as the liver or the prostate that are expected to preserve their volume during breathing or peristalsis. As a consequence, the NParBR method also minimizes artifacts such as sinking or shrinking of non-matching regions that are not representative, but improve the performance of a global convex measure [125]. This transformation is also regularized for spatial smoothness. The spatial normalization of an entire time series with pairwise registration can be subject to bias resulting from an arbitrary choice of an image from the series as a reference. Therefore, the registration of the DCE-MRI time series datasets computes and uses as reference an intra-dataset atlas representative of the entire dataset [76, 126, 127].

The pairwise NParBR method starts with additional pre-processing steps, which consist of a dynamic range standardization and subsequently a concatenation of a rigid and an affine spatial registration to the image selected as reference. The intensity standardization is performed by linearly rescaling the intensities of both images from 0 to a maximum value of 255. This step preserves the intensity distributions and their peaks. It also reduces the computational cost of the subsequent processing that involves the joint histogram and simplifies the parameterization of the method. It also enables the use of a Fast Fourier Transform (FFT) for the Wiener restoration in the Fourier domain. The result of the two pre-processing steps is then used to initialize the non-rigid registration. The effectiveness of the NParBR method has been empirically demonstrated over several different types of data such as brain [128], liver, prostate, lungs, and intestines [129, 130]. The NParBR method acts on a limited Region Of Interest (ROI) with meaningful tissues and imaging contrasts. It can accommodate two images with different types of imaging contrasts. In this work the ROIs over brain datasets have been determined automatically using the BET tool [131], while the ROIs over the internal organs such as the liver, prostate, lungs, and intestines have been manually annotated by experts. For the liver and the prostate, the ROI includes the whole organ with the embedded lesions. For other organs that are subject to a volume change due to their anatomy and function such as the lungs and the intestines, the ROI is limited to a region surrounding the main solid lesion. The development and implementation of the NParBR method is presented in detail in the next sections.

3.1 Overview of the Method

The problem of the non-rigid registration of pairs of images with the NParBR method has been formulated as non-parametric Bayesian estimation together with spatial smoothing. The non-parametric Bayesian estimation of the spatial registration field uses as prior a model for the distortion of the joint intensity statistics. The histogram computation is viewed as a projection, α, with units of intensity value $\mathbf{i}$ over spatial displacement $\mathbf{x}$, $\alpha = \mathbf{i} \cdot \mathbf{x}^{-1}$. The effect of the spatial misregistration on the joint intensity statistics is assumed to be a convolution of the joint histogram with a Gaussian

$$G(\Delta\mathbf{i}; 0, \sigma_\delta) = G(\alpha\Delta\mathbf{x}; 0, \sigma_\delta), \tag{3.1}$$

where $\mathbf{i} = (i, j)$ is an intensity pair and σ_δ is the standard deviation of the intensities distortion distribution in the joint intensity histogram. It maps the spatial window to a window in the dynamic range. The assumed Gaussian $G(\Delta\mathbf{i}; 0, \sigma_\delta)$ smoothing of the statistics is compensated for with deconvolution with a Wiener filter [122]. The Bayesian formulation results in back-projection of the restored statistics into image space. The back-projection has units of spatial displacement over intensity value, $\alpha^{-1} = \mathbf{i}^{-1} \cdot \mathbf{x}$.

The registration field is then smoothed with a spatial Gaussian filter $G(\mathbf{x}; 0, \sigma_S)$, where σ_S is the standard deviation for the spatial Gaussian smoothing. The optimization for the registration interleaves between the Bayesian estimation and the spatial smoothing at each iterative step, $k = 0, ..., K_{max} - 1$ for a total of K_{max} iterations. This optimization can be viewed as a coordinate descent process. The convergence of the method is shown empirically with the assumption that sharper statistics minimize the misregistration error in analogy to the eventual final state in hysteresis, such as magnetization in ferromagnetic hysteresis. An overview of the registration methodology is given with the diagram shown in Fig. 3-1.

3.2 Model of the Distortion of the Joint Intensity Statistics

A spatial misregistration between two images has an effect on the joint intensity statistics, that is described with an analogy to the physical phenomenon of the (ferromagnetic)

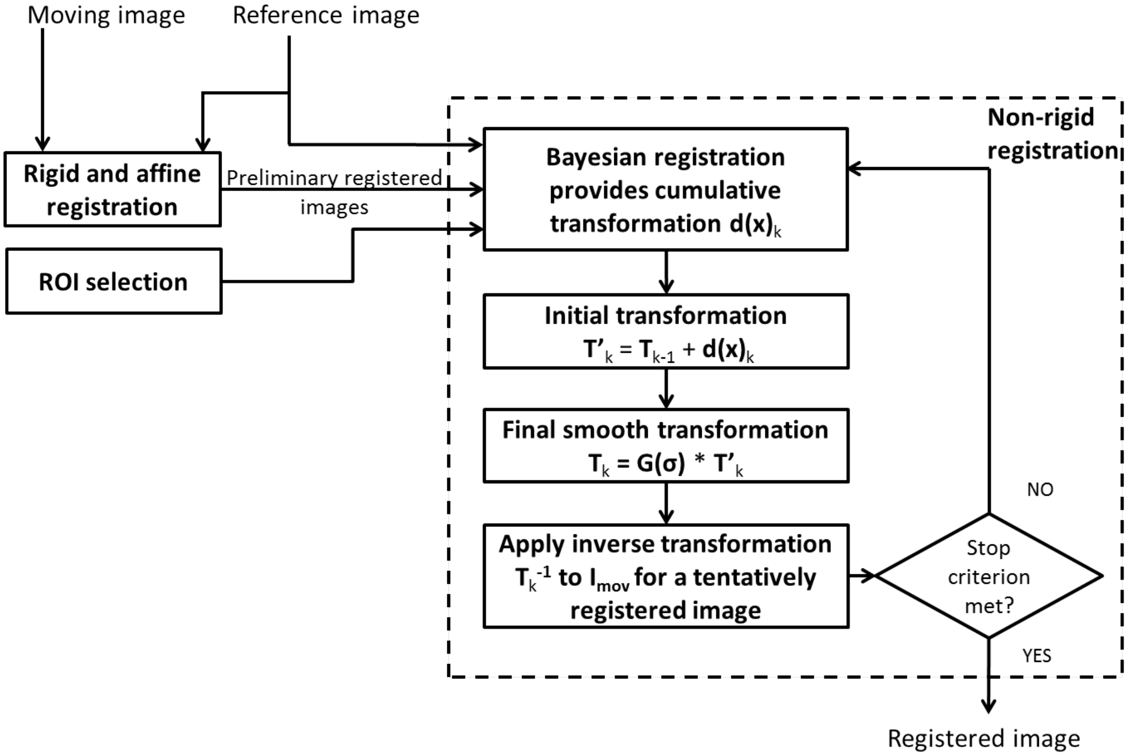

Figure 3-1: Diagram outlining the pairwise registration with the proposed registration method. A preliminary rigid and affine registration is performed and the result is used to initialize the iterative non-rigid registration iterations of NParBR.

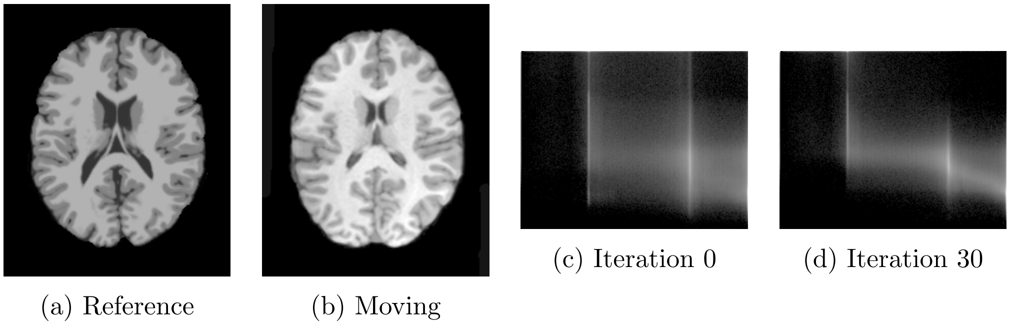
(a) Reference (b) Moving (c) Iteration 0 (d) Iteration 30

Figure 3-2: Joint statistics for initial images (a) and (b) at the initial iteration (c) and after 30 iterations (d). The joint statistics in (d) become sharper.

hysteresis [82, 83, 128]. The contrast between different tissue types is usually higher than the variations of the intensities or textures within regions of uniform tissue. The region boundaries are assumed to be smooth due to biological reasons as well as due to limited MRI resolution. As a result, the hysteresis effect in the joint intensity distributions in medical images is limited. This does not allow the creation of new cross-distributions beyond noise or other imaging artifacts. The outer envelope loop of the hysteresis effect is due to regions where the displacements normal to the corresponding regions boundaries are maximal. Thus, the hysteresis effect causes only a smoothing in the region between the statistical distributions of spatially adjacent regions. This smoothing of the joint intensity statistics is assumed to be Gaussian as given by Eq. (3.1).

A spatial neighborhood is defined as $\mathcal{N}_{\mathbf{x}} = \mathbf{x}+\Delta\mathbf{x}$, where $\Delta\mathbf{x}$ represents all possible shifts within $\mathcal{N}_{\mathbf{x}} = 3\times3\times3$. Each spatial location $\mathbf{x}$ in I_{ref} is linked to a cubic spatial neighborhood $\mathcal{N}_{\mathbf{x}}$ in I_{mov}. A simplified graph showing the linkage of a voxel in 3D to a voxel at location $\mathbf{x}$ in I_{ref} to voxels within $\mathcal{N}_{\mathbf{x}}$ in I_{mov} is in Fig. 3-3. The joint intensity statistics are calculated by relating the intensities of each voxel $\mathbf{x}$ in I_{ref} to each voxel in I_{mov} at the corresponding spatial location within neighborhood $\mathcal{N}_{\mathbf{x}}$. The joint statistics are computed by accumulating the occurences of the joint intensities throughout the images. This results in a bidimensional statistical distribution which gives rise to different distributions for different tissues as well as cross distributions for the boundaries between them.

It is assumed that two images I_{ref} and I_{mov} of the same anatomy under ideal latent alignment would give rise to the joint histogram H_{ideal}. The joint statistics H_{actual} of the misregistered images are considered to result from the convolution of H_{ideal} with a 2D Gaussian filter $G_{\delta}(\Delta\mathbf{i}; 0, \sigma_{\delta})$ that represents the distortion as described above:

$$H_{actual} = H_{ideal} * G_{\delta}(\Delta\mathbf{i}; 0, \sigma_{\delta}) + n_{\delta}, \tag{3.2}$$

where $*$ is the 2D convolution operator, σ_{δ} is the standard deviation, and n_{δ} is the noise in the statistics.

3.3 Image Restoration based on the Joint Intensity Statistics

The total registration vector $v(\mathbf{x})$ for the moving image at $\mathbf{x}$ is assumed to consist of the latent correct registration vector field $u(\mathbf{x})$ and the misregistration vector field $d(\mathbf{x})$,

$$v(\mathbf{x}) = u(\mathbf{x}) + d(\mathbf{x}). \tag{3.3}$$

It is assumed that $u(\mathbf{x})$ and $d(\mathbf{x})$ are mutually independent and identically distributed random variables. The independence assumption between $p_u(u(\mathbf{x}))$ and $p_d(d(\mathbf{x}))$, where $p(\cdot)$ denotes probability distribution gives:

$$p_v(v(\mathbf{x})) = p_u(u(\mathbf{x})) * p_d(d(\mathbf{x})), \tag{3.4}$$

where $*$ is the 2D convolution operator. The assumption of texture uniformity within tissues, local smoothness and imaging artifacts such as partial volume and noise leads to the probability distributions of the actual displacement $v(\mathbf{x})$ and the ideal displacement $u(\mathbf{x})$ as:

$$p_v(v(\mathbf{x})) = H_{actual}(I_{ref}(\mathbf{x}), I_{mov}(\mathbf{x} + v(\mathbf{x}))) \tag{3.5}$$

$$p_u(u(\mathbf{x})) = H_{ideal}(I_{ref}(\mathbf{x}), I_{mov}(\mathbf{x} + u(\mathbf{x}))), \tag{3.6}$$

where H_{actual} and H_{ideal} are the joint histograms of the two images I_{ref} and I_{mov} as they initially are and under assumed correct alignment, respectively. It is assumed that the distortion $p_d(d(\mathbf{x}))$ of the joint intensity statistics is modeled by the Gaussian distribution of Eq. (3.1) and is given by

$$p_d(d(\mathbf{x})) = G(\Delta\mathbf{i}; 0, \sigma_\delta) = G(\alpha\Delta\mathbf{x}; 0, \sigma_\delta). \tag{3.7}$$

This distribution gives the probability of $\Delta\mathbf{i}$ as described below:

$$\Delta\mathbf{i} = (I_{ref}(\mathbf{x}), I_{mov}(\mathbf{x} + d(\mathbf{x}))) - (I_{ref}(\mathbf{x}), I_{mov}(\mathbf{x})). \tag{3.8}$$

The conditional expectation of the assumed correct displacement $u(\mathbf{x})$ given the initial displacement $v(\mathbf{x})$ using Bayes' law for $p_{u|v}(u|v)$ [123, 124] is:

$$E[u|v] = \int p_{u|v}(u|v)u du = \int \frac{p_{v|u}(v|u)p_u(u)u du}{p_v(v)} = \frac{\int p_{v|u}(v|u)p_u(u)u du}{\int p_{v|u}(v|u)p_u(u) du}. \tag{3.9}$$

It is assumed that the prior probability of correct displacement $p_u(u)$ can be computed from the probability of the actual displacement $p_v(v)$ with its deconvolution from the model of the distortion $p_d(d)$. The deconvolution is performed with Wiener filtering in the Fourier domain where the Fourier transform $\mathcal{F}(\cdot)$ of the probability of the assumed correct displacement

$\mathcal{F}(p_u(u))$ can be estimated from $\mathcal{F}(p_v(v))$ by deconvolution with a Wiener filter $\mathcal{R}$ [124]. In the Fourier domain the Wiener filter $\mathcal{R}$ is given by

$$\mathcal{R} = \frac{|\mathcal{G}|}{|\mathcal{G}|^2 + \epsilon}, \tag{3.10}$$

where $\mathcal{G}$ is the Fourier transform of a Gaussian distribution for $p_d(d(\mathbf{x}))$, and $\epsilon = \frac{1}{SNR}$ is the inverse of the signal to noise ratio of the statistics. That is,

$$\mathcal{F}(p_u(u)) \approx \mathcal{R}\mathcal{F}(p_v(v)). \tag{3.11}$$

Moreover, $u(\mathbf{x})$ and $d(\mathbf{x})$ are assumed to be statistically independent, identically distributed random variables as in Eq. (3.3). Assuming also shift invariance as in the general context of the coring methodology [123, 124, 132], the conditional can be simplified into:

$$p_{v|u}(v|u) = p_d(v - u) = p_d(d), \tag{3.12}$$

where $p_{v|u}$ is the conditional probability density function of the observed displacement, p_d is the probability density function of the distortion, and $G(\Delta\mathbf{i}; 0, \sigma_\delta)$ is the Gaussian distribution as given in Eq. (3.1). The inverse Fourier transform of the Wiener filter $\mathcal{R}$ to the domain of the joint intensities is given by $r = \mathcal{F}^{-1}(\mathcal{R})$. The inversion of the restoration filter to the domain of the dynamic ranges is used only for notational convenience and is not implemented as part of the method. The substitution of Eq. (3.12) into Eq. (3.9) gives:

$$\begin{aligned} E[u|v] &= \frac{\int p_{v|u}(v|u)(r * p_v(v))u du}{\int p_{v|u}(v|u)(r * p_v(v)) du} \\ &= \frac{\int G(\Delta\mathbf{i}; 0, \sigma_\delta)(r * p_v(v))u du}{\int G(\Delta\mathbf{i}; 0, \sigma_\delta)(r * p_v(v)) du}. \end{aligned} \tag{3.13}$$

The substitution of Eq. (3.11) and Eq. (3.5) into Eq. (3.13) gives

$$E[u|v] = \frac{\int G(\Delta\mathbf{i}; 0, \sigma_\delta)(r * H_{actual})u du}{\int G(\Delta\mathbf{i}; 0, \sigma_\delta)(r * H_{actual}) du}. \tag{3.14}$$

Eq. (3.14) can be discretized with $\Delta u \in \mathcal{N}_\mathbf{v}$, where $\mathcal{N}_\mathbf{v}$ is the neighborhood of the observed displacement $\mathbf{v}$, to give:

$$\begin{aligned} E[u|v] &= \frac{\Sigma_{\mathcal{N}_{\mathbf{v}}}[G(\Delta \mathbf{i}; 0, \sigma_\delta) \cdot (r * H_{actual}) \cdot (v + \Delta u)]}{\Sigma_{\mathcal{N}_{\mathbf{v}}}[G(\Delta \mathbf{i}; 0, \sigma_\delta) \cdot (r * H_{actual})]} \\ &= \frac{\Sigma_{\mathcal{N}_{\mathbf{v}}}[G(\alpha \Delta u; 0, \sigma_\delta) \cdot (r * H_{actual}) \cdot (v + \Delta u)]}{\Sigma_{\mathcal{N}_{\mathbf{v}}}[G(\alpha \Delta u; 0, \sigma_\delta) \cdot (r * H_{actual})]}. \end{aligned} \tag{3.15}$$

3.4 Back-projection of the Statistical Restoration

After the restoration of the joint intensity statistics with the Wiener filter, the Bayesian formulation of Eq. (3.15) can give the spatial transformation. The first step to estimate a spatial transformation is to link each location $\mathbf{x}$ in I_{ref} to a cubic spatial neighborhood $\mathcal{N}_{\mathbf{v}}$ in I_{mov}.

The expectation $E[u|v]$ of the restoration enables the estimation of the distortion $d(\mathbf{x})$ considering also the stability property of the conditional expectation $E[v(\mathbf{x})|v(\mathbf{x})] = v(\mathbf{x})$ as:

$$\begin{aligned} d(\mathbf{x}) &= E[d(\mathbf{x})|v(\mathbf{x})] \\ &= E[v(\mathbf{x}) - u(\mathbf{x})|v(\mathbf{x})] \\ &= E[v(\mathbf{x})|v(\mathbf{x})] - E[u(\mathbf{x})|v(\mathbf{x})] \\ &= v(\mathbf{x}) - E[u(\mathbf{x})|v(\mathbf{x})] \\ &= v(\mathbf{x}) - \frac{\Sigma_{\mathcal{N}_{\mathbf{v}}}[G(\Delta \mathbf{i}; 0, \sigma_\delta) \cdot (r * H_{actual}) \cdot (v + \Delta u)]}{\Sigma_{\mathcal{N}_{\mathbf{v}}}[G(\Delta \mathbf{i}; 0, \sigma_\delta) \cdot (r * H_{actual})]} \\ &= v(\mathbf{x}) - \frac{\Sigma_{\mathcal{N}_{\mathbf{v}}}[G(\alpha \Delta u; 0, \sigma_\delta) \cdot (r * H_{actual}) \cdot (v + \Delta u)]}{\Sigma_{\mathcal{N}_{\mathbf{v}}}[G(\alpha \Delta u; 0, \sigma_\delta) \cdot (r * H_{actual})]}. \end{aligned} \tag{3.16}$$

3.5 Estimation of Smooth Spatial Transformation

At the starting iteration $k = 0$ the vector $v(\mathbf{x})$ is initialized to 0 for the entire image domain. The mis-registration is also assumed to be spatially smooth. Following Eq. (3.15) and (3.16), the restored joint intensity statistics are back-projected to space to give an initial spatial transformation $d(\mathbf{x})_k$ at iteration $k > 0$ as in Eq. (3.16) to obtain $\mathbf{T}'_k(\mathbf{x}) = E[u(\mathbf{x})|v(\mathbf{x})]$ that is an initial estimate of the spatial transform

$$\mathbf{T}'_k(\mathbf{x}) = \mathbf{T}_{k-1}(\mathbf{x}) + d(\mathbf{x})_k, \tag{3.17}$$

where $\mathbf{T}_{k-1}(\mathbf{x}) = u_{k-1}(\mathbf{x})$ is the total displacement from the previous iteration. To regularize the Bayesian estimate of the transformation $\mathbf{T}'_k$, the gradient magnitude $||\nabla \mathbf{T}'_k||_2$ over the image is penalized. This is equivalent to the application of a 3D Gaussian filter $G(\mathbf{x}; 0, \sigma_S)$, where σ_S is the standard deviation of the smoothing of the spatial transformation $\mathbf{T}'_k$. The final estimate of the spatial transformation at iteration k is obtained with

$$\mathbf{T}_k(\mathbf{x}) = \mathbf{T}'_k(\mathbf{x}) * G(\mathbf{x}; 0, \sigma_S). \tag{3.18}$$

The value of $\mathbf{T}_k(\mathbf{x})$ is calculated for all $\mathbf{x}$ in the ROI of $I_{ref}(\mathbf{x})$.

3.6 Implementation

The NParBR method has been implemented in *C++* and the tests were performed on a workstation with an Intel Core2 Duo 3.0 GHz CPU having 16GB of RAM. The complete method operates over the 3 spatial dimensions for the two brain anatomic MRI data and the 3 spatial together with the temporal dimension for the DCE-MRI data. The pairwise non-rigid registration developed is preceded by the rigid and affine registration methods provided by ITK [133] using their default settings such as for subsampling and interpolation. The ITK default implementation uses the Mattes MI [106] as similarity criterion and the gradient descent as optimizer. The atlas for the DCE-MRI data was computed with a maximum of 20 iterations.

The Wiener filtering in Eq. (3.10) and Eq. (3.16) of the joint intensity statistics of size 256 × 256 as part of the non-rigid registration was performed in the Fourier domain using the forward and backward FFT functionality included in ITK [133]. The value of σ_δ for the non-rigid registration has been set for all datasets to 3 intensity levels of the dynamic range of size 256. The value of σ_δ is accumulated along the iterations to give the total distortion of the joint intensity statistics. The value of ϵ of the Wiener filter has been set to 0.1 for all datasets. The Bayesian formulation is used to implement the forward projection to the statistics and the backward projection to the spatial domain according to Eq. (3.16) using a cubic spatial neighborhood $\mathcal{N}_{\mathbf{x}}$ of size $3 \times 3 \times 3$ voxels. This results in an estimation of a spatial transformation as described in Eq. (3.17). This is subsequently spatially regularized as described in Eq. (3.18). The spatial regularization $G(\mathbf{x}; 0, \sigma_S)$ of the non-rigid registration has been performed using an efficient separable implementation of the 3D Gaussian filter in ITK. The value of σ_S has been set equal to the length of the side of an in-plane voxel in 3D for all datasets.

The implementation of the NParBR method is iterative. A spatial displacement is estimated and spatially regularized at each iteration. The resulting spatial transformation is accumulated along the iterations to estimate displacements larger than 1 voxel. The convergence of the registration is evaluated at every iteration. A criterion that uses the average L_2 norm of the spatial transformation $||T_k||$ is used. The iterations $k > 0$ end when the condition $0.99 < \frac{||T_k||}{||T_{k-1}||} < 1.01$ is satisfied. A maximum number of $k_{max} = 50$ iterations is also enforced for the non-rigid registration.

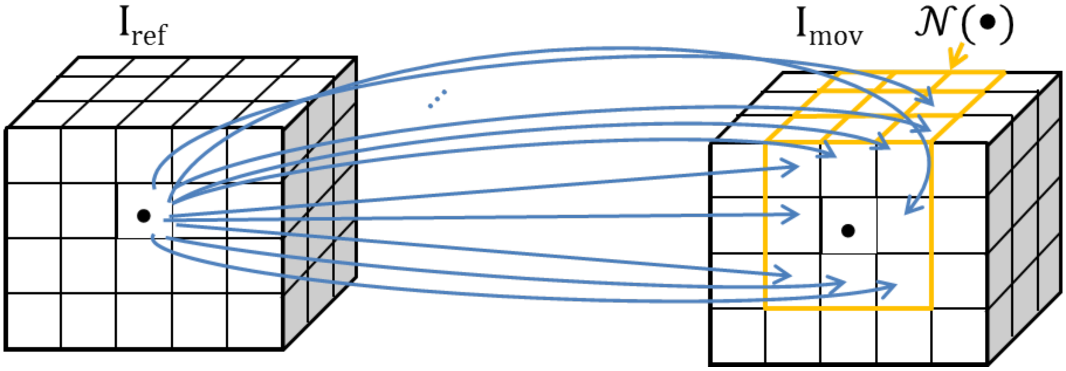

Figure 3-3: An example of linking voxels of two images within a neighborhood $\mathcal{N}$.

3.7 Order of Computational Complexity

The computational cost of the registration of DCE-MRI datasts is expressed as a function of: K-number of iterations, m-effective size for each of the image dimensions, n-size of a neighborhood window $|\mathcal{N}_{\mathbf{x}}|$ around a pixel, p-spatial subsampling factor between B-Spline center nodes, dim is the spatial dimensionality of the data, σ_S the standard deviation of the spatial smoothing, and τ the number of images for the time series data for $t-1$ registrations. For brain datasets the size of the time dimension is taken to be the unity, $\tau = 1$. The complexity of the NParBR method is $O([m^{dim}n + m^{dim}dim \cdot \sigma_S]K\tau)$, while that of the B-Splines method with the MI is higher by a multiplicative factor of $(m/p)^{dim}$.

The cost of the Demons and of the SyN methods extended with the MI can be even higher than that of the B-Splines depending on the levels l of the multiresolution pyramids they are often combined with in optimization. Assuming that the image widths are halved at every pyramid level, the cost is higher than that of the NParBR method by the factor $\sum_{l'=0}^{l-1} \frac{1}{l'} \left(\frac{m}{2^{l'}}\right)^{dim}$.

The size of an image can influence the number K of iterations for all iterative registration methods, namely, the NParBR, the B-Splines, and the SyN methods. A sufficiently large ROI can provide a sufficient number of samples, which can improve the convergence of a statistics based method such as the NParBR.

It was empirically shown that all the considered methods reach convergence in approximately the same order of number of iterations. The complexity of the NParBR method increases slower than the complexity of the B-Splines and the SyN methods when the dimensionality dim of the image increases, since the estimation of the smooth transformation is performed by the NParBR method only once per iteration in comparison to the $(m/p)^{dim}$ times of the B-Splines and the $\sum_{l'=0}^{l-1} \frac{1}{l'} \left(\frac{m}{2^{l'}}\right)^{dim}$ times of the SyN. These multiplicative factors increase the computational cost for B-Splines and the SyN methods significantly and proportionally to the order of the exponent of the image dimensionality dim.

3.8 Intra-dataset Atlas Computation for DCE-MRI Datasets

The selection of an image from a time-series as I_{ref} for the registration of an entire time-series introduces a bias in the atlas to that image. An approach to reduce this bias problem is to calculate an atlas image I_{atl} with reference from all the images in the time series of a patient. The calculation of the atlas is iterative and alternates between the calculation of the 3D tentative average image $I_{avg,k}$ and the following ITK affine registration [133] of all the 3D input images $I_{mov,k,t}$ to $I_{avg,k}$. The average image at iteration k is defined as

$$I_{avg,k} = \frac{1}{\tau} \sum_{t=0}^{\tau-1} I_{mov,k,t}, \tag{3.19}$$

where k is the iteration index. The iterations terminate when the condition $0.99 < \frac{||I_{avg,k}||}{||I_{avg,k-1}||} < 1.01$ is satisfied for $k > 0$ or after a maximum of $K_{atl} = 20$ iterations. The final average image gives the atlas $I_{atl} = I_{avg,k}$ as output. The experimental results have shown that the final average images are indeed sharper and that the method can provide the reference of the registration $I_{ref} = I_{atl}$ for an entire time-series. Thus, the registration of the time series datasets can be made with minimal bias to any specific time-point image using the calculated intra-dataset atlas I_{atl}.

Chapter 4

Application of NParBR in Medical Imaging

Image registration is an important task in particular for medical image analysis. The movement of a patient as well as the movement of the internal organs can be reduced but not completely avoided. The residual movement results in motion artifacts which cause significant image artifact that can potentially lead to an incorrect analysis of a medical image. To cope with the misalignment problem many different approaches have been proposed and applied to medical images. Relevant literature has been provided in Chapter 2. The method presented in Chapter 3 has been tested on different MRI phantom data such as a 3D extension of the Shepp-Logan brain phantom [134, 135], images taken from the Brainweb database [42], and datasets from the NIREP database [136]. The NParBR method has also been tested on real MRI and DCE-MRI datasets of different human organs such as brain [128], liver, prostate, lungs, and intestines [130]. The NParBR method has also been tested on lung CT datasets from the EMPIRE10 challenge [8]. The presented method has been compared with the most commonly used registration methods such as the one based on the SyN model and the one based on the B-Splines model presented in Section 2.4.4 and in Section 2.4.1, respectively. SyN and B-Splines methods have been selected because of their applicability to different types of medical datasets as well as for their extensive validation, which made these methods widely used.

4.1 Validation Measures

A general, however, subjective evaluation of registration has been a visual evaluation by comparing images before and after registration using a checkerboard pattern. The visual inspection of the registration resulting with the proposed method has been performed on all the considered datasets in this work and has been compared with the results from state-of-the-art methods such as B-Splines and SyN. Due to its subjectiveness and non-quantitative nature, the visual inspection of the resulting registered images has to be supported by different quantitative evaluations.

Phantom data such as the 3D extension of the Shepp-Logan brain MRI phantom as well as images taken from the Brainweb database have been modified with the application of a spatial sinusoidal transformation to simulate a non-rigid misregistration and using as reference the original image I_{true} to perform a quantitative evaluation of the registration. To evaluate the quality of the registration obtained from the Shepp-Logan and Brainweb phantom datasets with the presented method, the voxelwise Sum of Absolute Differences (SAD) has been calculated within the corresponding ROI between the true image I_{true} and the registered image I_{reg}

$$SAD = ||I_{true}(\mathbf{x}) - I_{reg}(\mathbf{x})||_2. \tag{4.1}$$

The SAD for the phantom data has been calculated before and after the registration, giving the values SAD_{bef} and SAD_{aft}, respectively. The percent improvement of SAD is defined as

$$SAD_{Imp} = \frac{SAD_{bef} - SAD_{aft}}{SAD_{bef}} 100\%, \tag{4.2}$$

where a higher value of SAD_{Imp} denotes an improved performance.

This measure has also been used to evaluate the quality of the registration of DCE-MRI datasets by calculating the SAD between consecutive frames

$$SAD_t = \frac{1}{\tau - 1} \sum_{t=0}^{\tau-2} \sum_{\mathbf{x}} |I_{t+1}(\mathbf{x}) - I_t(\mathbf{x})|, \tag{4.3}$$

where $t = 0, ..., \tau - 1$. The value of SAD_t is calculated within the ROI used for registration and is desired to decrease. The percent improvement $SAD_{Imp,t}$ of SAD is defined as

$$SAD_{Imp,t} = \frac{SAD_{bef,t} - SAD_{aft,t}}{SAD_{bef,t}} 100\%, \tag{4.4}$$

where $t = 0, ..., \tau - 1$ denotes time. A higher value of $SAD_{Imp,t}$ denotes an improved performance.

The registration of the bi-contrast human brain real datasets has also been evaluated by calculating the percent improvement in MI

$$MI_{Imp} = \frac{MI_{aft} - MI_{bef}}{MI_{aft}} 100\%, \tag{4.5}$$

where MI_{bef} and MI_{aft} are the values of MI calculated before and after the registration, respectively.

For the DCE-MRI datasets, the registration has also been evaluated by calculating the percent improvement in MI

$$MI_{Imp,t} = \frac{1}{\tau} \sum_{t=0}^{\tau-1} \frac{MI_{aft,t} - MI_{bef,t}}{MI_{aft,t}} 100\%, \tag{4.6}$$

where $MI_{bef,t}$ and $MI_{aft,t}$ are the time-series average values of MI calculated between I_{ref} and $I_{mov,t}$ before and after the registration, respectively. A higher value of $MI_{Imp,t}$ denotes a better performance of the considered method in terms of MI.

Standard deviation images of human brain datasets

$$I_{stddev} = \sqrt{\frac{\Sigma_{i=0}^{i=N-1} (I_i(T_i \mathbf{x}) - I_{mean})^2}{N-1}} \tag{4.7}$$

have been calculated within a ROI. Voxelwise average intensity mean $\langle I_{mean} \rangle_{\mathbf{x}}$ and standard deviation $\langle I_{stddev} \rangle_{\mathbf{x}}$ have also been calculated within the same ROI to give an average quality performance index. A lower value of $\langle I_{stddev} \rangle_{\mathbf{x}}$ denotes an improved performance.

For all the liver, lung, and intestines datasets a manual annotation of the main lesion that considered also the displacement of the lesion along time has been performed by an expert. Thus, for every dataset another corresponding binary dataset was produced and was composed by a series of segmented images $I_{bin,t}$, with $t = 0, ..., \tau - 1$. The displacement fields resulting from the registration have been applied to the time series of the binary segmented annotations of the lesions. An overlap of the binary registered lesion segmentations along time has been quantified by calculating the standard deviation σ_{bin} of the binary segmentation along time

$$\sigma_{bin} = \frac{1}{\tau}\sum_{t=0}^{\tau-1}\sqrt{\frac{1}{|\mathbf{x}-1|}\sum_{\mathbf{x}}(M_{bin}(\mathbf{T}^{-1}(\mathbf{x})) - I_{bin,t}(\mathbf{T}^{-1}(\mathbf{x})))^2}, \tag{4.8}$$

where

$$M_{bin} = \frac{1}{\tau}\sum_{t=0}^{\tau-1} I_{bin,t} \tag{4.9}$$

is the average of the binary segmented lesion annotation along time. This gives performance index values which decrease with improvements of the registration [125]. The time-series average standard deviation of the segmented lesion $\sigma_{bin,bef}$ and $\sigma_{bin,aft}$ calculated before and after the registration, respectively, gives rise to the percent improvement $\sigma_{bin,Imp}$ as:

$$\sigma_{bin,Imp} = \frac{\sigma_{bin,bef} - \sigma_{bin,aft}}{\sigma_{bin,bef}} 100\%. \tag{4.10}$$

A positive and high value of $\sigma_{bin,Imp}$ denotes a better performance.

A further evaluation on DCE-MRI datasets has been performed by calculating the residual errors RES of the pharmacokinetic perfusion model fitting. A MATLAB based implementation of the Tofts pharmacokinetic model has been used [137,138]. The values RES_{bef} and RES_{aft} have been calculated for all methods before and after the registration, respectively. The percent improvement RES_{Imp} of the residual error is defined as

$$RES_{Imp} = \frac{RES_{bef} - RES_{aft}}{RES_{bef}} 100\%. \tag{4.11}$$

A kymogram has also been used to track the displacement of a lesion along time before and after the registration for visual evaluation of DCE-MRI datasets. The tracking in the three axes is performed with three arrays centered in the geometrical center of the lesion. The size of the arrays has been determined by considering the size of the lesion plus 3 voxels in every direction to better appreciate the contrast of the lesion. The colors in the kymograms represent the intensity of voxels showing a separation between the different tissue types.

To evaluate the NIREP data, a validation based on the labeled data has been used.

The estimated final spatial transformation T_k has been applied to the labeled images corresponding to the volunteers data L_{mov} to obtain the labeled image $L_{reg}(\mathbf{x}) = L_{mov}(T_k^{-1}(\mathbf{x}))$ in registered space. The $DICE_L$ coefficient is defined as

$$DICE_L = \frac{2 \cdot TP}{2 \cdot TP + FP + FN}, \tag{4.12}$$

where TP is the labeled region of true positives, FP is the labeled region of false positives, and FN is the labeled region of false negative labeled regions. The value of $DICE_L$ has been calculated between the registered labeled image L_{reg} and the reference labeled image L_{ref} to quantify the similarity between the two images over the 32 considered regions. The $DICE_L$ coefficient gives a quantitative measure of the overlap between different brain regions and consequently a quantification of the registration performance. High performance for $DICE_L$ coefficient is obtained for values close to unity.

The quantitative evaluation provided by the EMPIRE10 takes into account four different aspects and it has been described in detail in [8]. The first one quantifies the error in alignment of the lung boundaries, considering points within 20mm from the lung boundaries and excluding points within 2mm from the boundaries which may be inaccurate due to segmentation errors. A similar approach has been used also to evaluate the alignment of major fissures, which are the structures that divide the lungs in regions called lobes. For this evaluation method were considered only the major fissures, which are the most visible, to facilitate the evaluation. To quantify the alignment of small internal structures of the lungs such as the alveoli, a correspondence between landmark pairs has been used. First a set of 100 well distributed set of landmarks have been automatically defined in I_{ref} of each scan pair. Then, the same landmarks were identified in the registered image I_{reg} submitted to the challenge and finally the Euclidean distance between landmarks in I_{ref} and I_{reg} has been calculated. The final evaluation criterion that has been used within the EMPIRE10 challenge is to analyze the physical plausibility of the estimated transformations. The regions where the deformation field is not bijective, i.e. there is no one-to-one correspondence between voxels of I_{ref} and I_{reg}, are called singularities. Each singularity has been assigned a unit penalty value. This number can then quantify the physical appropriateness of the estimated deformation field. An exaustive explanation of the evaluation methodology used for the EMPIRE10 datasets together with the complete results table is provided in the

Appendix.

4.2 Phantom Data

The purpose of phantom data is to model simple structures as well as simulate structures of the human body to test and optimize image acquisition with different techniques such as MRI. The synthetic data obtained can be further modified to also test an image registration method, focusing on the alignment of some structures that can be significant in the medical context. In medical imaging different models have been proposed to model in particular the human brain. One of the most popular ones is the one proposed by Shepp and Logan [134]. This phantom is a simplified model of the human brain simulating some brain structures such as the ventricles.

Models that reflect the anatomy of a human brain have also been proposed. One of the most popular ones is the atlas of a human brain acquired with different MRI contrasts that is part of the BrainWeb project [42]. Images from the BrainWeb database can be artificially distorted and used to test and validate an image registration method. Another commonly used human brain database used to evaluate an image registration method is the NIREP, which has been proposed by Christensen et al. [136]. In this work the aforementioned phantoms and databases have been used for the validation of the proposed method.

4.2.1 Shepp-Logan

The Shepp-Logan phantom is a well-known simple model of a human brain [134]. It has been widely used mainly for the development of image reconstruction methods as well as image registration methods. The 3D Shepp-Logan phantom has been introduced by Schabel et al. [135] as an extension of the aforementioned phantom. The proposed method has been validated with a multicontrast simulation from the 3D Shepp-Logan phantom with a full resolution of $128\times128\times128$ pixels as shown in Fig. 4-1. The phantom has been modified to simulate a contrast change. A 3D sinusoidal function over all the spatial coordinates has been applied to also simulate a non-rigid transformation. The value of σ_S for the spatial smoothing of the Shepp-Logan phantom has been set to 6 voxels. The registration has been performed within a provided ROI shown in Fig. 4-1e. After 8 iterations it can be seen in Fig. 4-1g that the phantom shows an obvious improvement in alignment. The registration

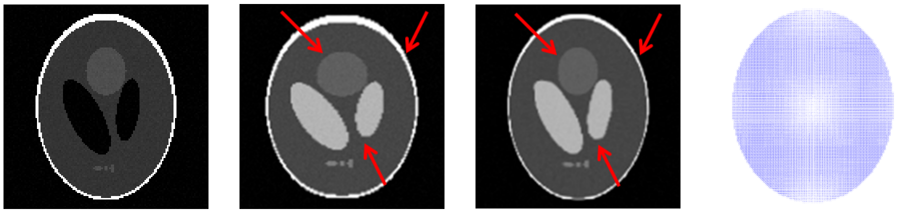

(a) Reference (b) Moving (c) Registered (d) Applied field

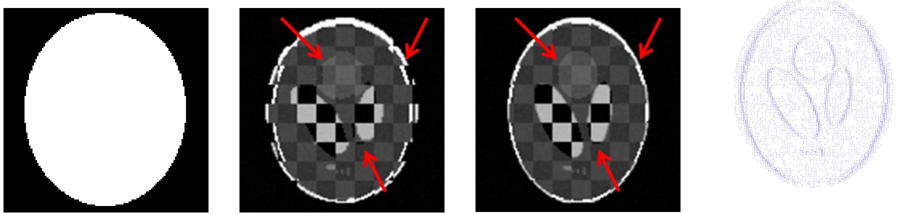

(e) ROI mask (f) Before (g) After (h) Recovered field

Figure 4-1: A 2D axial slice from the 3D Shepp-Logan phantom. (a) is the reference image, (e) is the ROI used, (b) is the misregistered image, and (c) is the registered image obtained with the proposed method. In (f) and (g) are the checkerboard compositions interleaving I_{ref} and I_{mov} before and after the registration. In (d) is the synthetic displacement field applied to (a) to obtain (b). In (h) is the final estimation of the displacement field applied to (b) to obtain (c). In intensity uniform regions that lack textures, the recovery of the displacement may be ambiguous.

between I_{ref} and I_{mov} gives an SAD_{Imp} of about 68%. A performance comparison with the B-Splines and the SyN method is shown in Table 4.1, where it is shown that the proposed method has improved comparatively both spatial operating resolution and accuracy in terms of SAD_{Imp}.

4.2.2 BrainWeb

The BrainWeb phantom resulted from repeated imaging of a young volunteer at 1.5T MRI scanner. Subsequent segmentation into tissues with noise removal. Then controlled levels of noise are added. The BrainWeb phantom is extensively used to give a brain model with ground truth and consequently help the evaluation of the brain image analysis methods [42]. The BrainWeb database consist of a set of realistic simulated human brains, covering different MRI modalities as well as different noise levels. Datasets from the BrainWeb database have also been used for testing the NParBR method as shown in Fig. 4-2. The selected data consist of two images with a voxel of resolution $1\times1\times1mm^3$ and a matrix of size $180\times216\times180$ of T_1w and T_2w contrasts. Both the noise level and the bias field have been set to zero. The T_1w image has been chosen as a reference. A non-linear misregistration has been simulated with a 3D sinusoid in spatial coordinates and applied to the T_2w image. The evaluation of the quality of the registration on the BrainWeb phantom has been performed considering the value of SAD_{Imp}. In the second row of Table 4.1 are the results of the proposed method in comparison to the ones obtained with SyN and B-Splines. The proposed method has obtained the best score in terms of SAD_{Imp} in comparison with the other methods. The value of σ_S for the Shepp-Logan phantom has been set to 6 voxels.

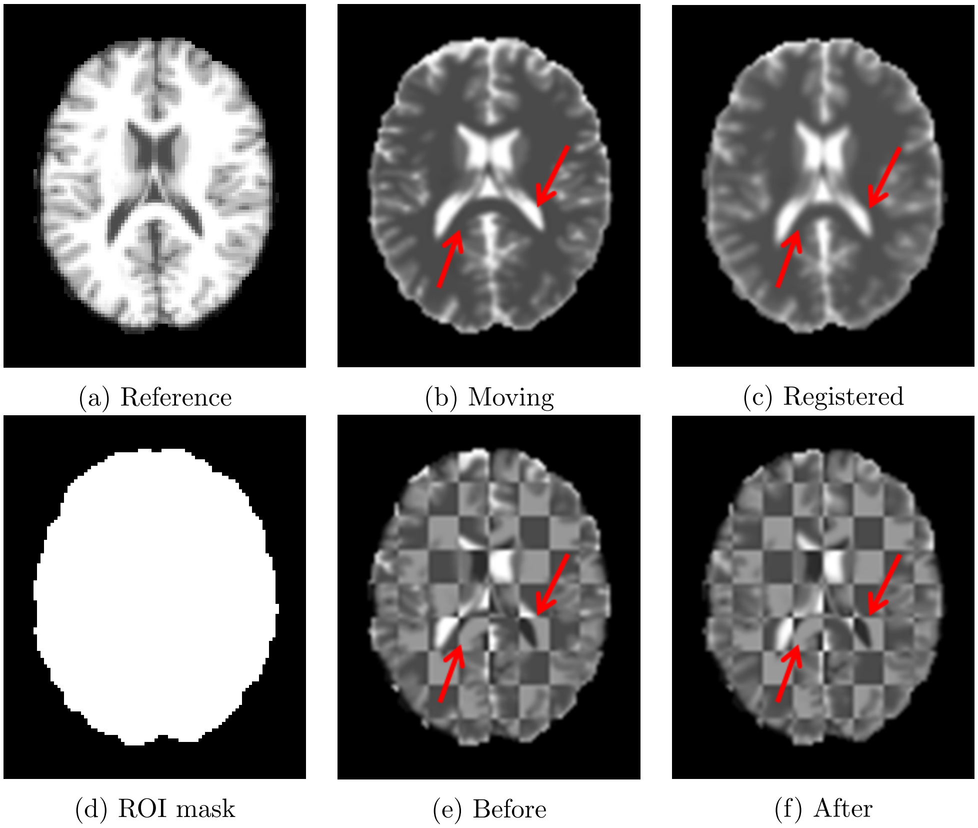
(a) Reference (b) Moving (c) Registered

(d) ROI mask (e) Before (f) After

Figure 4-2: A 2D axial slice from the 3D BrainWeb phantom. (a) is the reference image, (d) is the ROI used, (b) is the misregistered image, and (c) is the registered image obtained with the proposed method. In (e) and (f) are the checkerboard compositions interleaving I_{ref} and I_{mov} before and after the registration of the different contrast datasets. The red arrows point to alignment improvements over the ventricles and sulci.

The registration has been performed within a provided ROI shown in Fig. 4-1e. After 8 iterations it can be seen in Fig. 4-1g that the phantom shows an improvement in alignment. The value of σ_S for the BrainWeb phantom has been set to $5mm$. Representative results of the comparison with the B-Splines and the SyN method are shown in the images in Fig.

Datasets	Method	SAD_{Imp}	Resol. (voxels)	Exec. time	Memory Space
Shepp-Logan Phantom	SyN	68.19%	1	∼18min	450MB
	B-Splines	65.13%	1/262	∼1min	730MB
	Proposed	68.54%	1	∼18min	450MB
BrainWeb Phantom	SyN	53.08%	1	∼18min	450MB
	B-Splines	52.49%	1/875	∼2min	4GB
	Proposed	64.11%	1	∼ 90min	2GB

Table 4.1: Performance and comparison of the proposed method with that of B-Splines and that of SyN over the Shepp-Logan phantom, the $T_1w - T_2w$ BrainWeb phantom, and the five $T_1w - FLAIR$ volunteers datasets. The higher value of SAD_{Imp} of the proposed method denotes its better performance quality.

4-2. The B-Splines method tested operates over a grid of size $20 \times 20 \times 20$, which in the case of the BrainWeb phantom dataset implies a resolution of $9 \times 10.8 \times 9mm^3 = 875mm^3$ as subsampling. The B-Splines grid size has been chosen to maximize the registration quality while keeping their computational cost reasonable. The proposed method operates in full spatial resolution of $1{\times}1{\times}1mm^3$, which is equivalent to a resolution 875 times higher than that of the B-Splines method. The registration between I_{ref} and I_{mov} gives an SAD_{Imp} of about 68% for the Shepp-Logan phantom and of about 64% for the BrainWeb phantom. A performance comparison with the B-Splines and the SyN methods is given in Table 4.6, where it is shown that the proposed method has improved performance both in spatial operating resolution and accuracy in terms of SAD_{Imp}.

4.2.3 NIREP

The NIREP database consists of 3D brain datasets of 16 volunteers together with the labeling L of 32 different brain structures [136]. It is a commonly used framework to evaluate non-rigid registration algorithms. The NIREP database consist of 16 3D volumes with a matrix of size $256 \times 300 \times 256$ and with a voxel of resolution $1 \times 1 \times 1mm^3$. All the datasets were acquired using a T_1w sequence and have manual segmentations of 32 different brain anatomic regions considered as gold standard. An example of the registration performed on the NIREP datasets is shown in Fig. 4-3. The results of the NIREP validation are in Table 4.2, where it is shown that the proposed method outperforms SyN for all brain regions. The B-Splines outperforms the proposed method and SyN in terms of $DICE_L$ but not always by visual observation. The B-Splines method obtained a better performance in

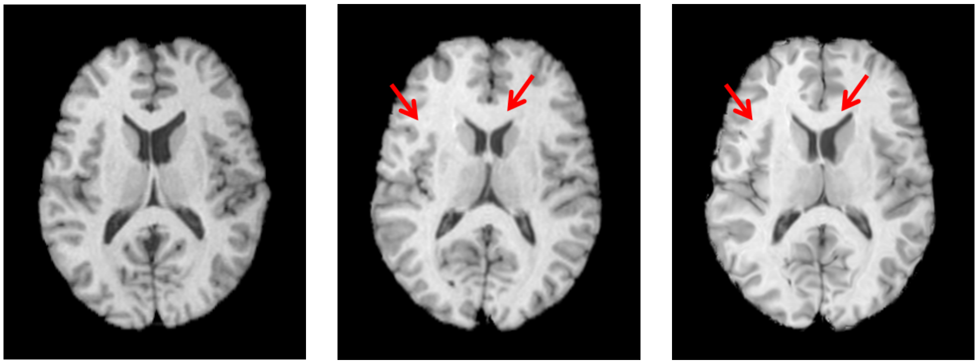

(a) Reference (b) Moving (c) Registered

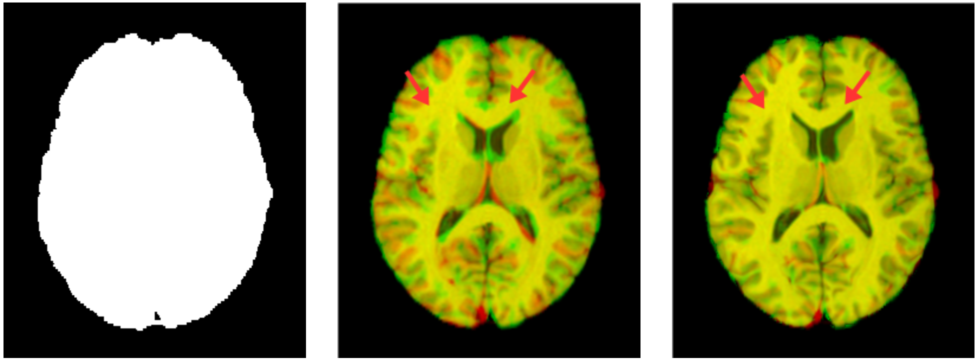

(d) ROI mask (e) Before (f) After

Figure 4-3: A 2D axial slice from 3D dataset of NIREP database. (a) is the reference image, (d) is the ROI used, (b) is the misregistered image, and (c) is the registered image obtained with the proposed method. In (e) and (f) are the channel merge images interleaving I_{ref} and I_{mov} before and after the registration of the same contrast datasets, respectively. The yellow color denotes good alignment. The red arrows point to alignment improvements over the ventricles and sulci.

terms of $DICE_L$ for the various anatomic regions since it operates on a subsampled grid with spacing in the order of the regions, which helps to model the B-Splines basis functions for a region even if it is at a lower resolution. On the other hand, the SyN and the NParBR methods estimate a dense displacement field, which in the absence of textures can lead to a smaller improvement in the alignment.

The mean image

$$I_{mean} = \frac{\Sigma_{i=0}^{i=v-1}(I_i(T_i\mathbf{x}))}{N}, \tag{4.13}$$

where N is the number of volunteers, has been calculated within a ROI to give a visual impression for the evaluation. The calculation of an average image after the registration of a set of images can provide an immediate visual evaluation of the effect of an image registration method. All the images of the dataset are independently registered to the same reference image. The effect of an effective registration on such dataset will be a creation of a sharp average image. The average images produced by the proposed method and B-Splines are comparable and are both sharper than the average produced with SyN. The proposed method produces on average a sharper image than SyN in all the considered brain regions and a sharper image than B-Splines in some significant internal brain regions, as shown in Fig. 4-4. The average images obtained with the proposed method show an increased sharpness on both the ventricles and on the sulci in comparison to those from both B-Splines and SyN. The increased working resolution of the proposed method compared to B-Splines is shown by the improvement in the sharpness of both the ventricles and the sulci that it achieves. The red arrows in Fig. 4-4 highlight the effects of the registration on cortical brain structures as well.

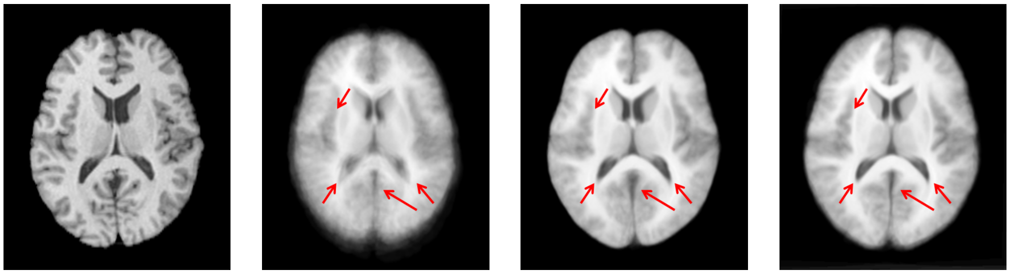
(a) Reference (b) SyN (c) B-Splines (d) Proposed

Figure 4-4: A 2D axial slice of 3D NIREP average images. (a) is the reference image, (b) is the average output image obtained with SyN, (c) is the average output image obtained with B-Splines, and (d) is the average output image obtained with the proposed method. The proposed method outperforms SyN in all brain regions.

4.3 Human Brain MRI

Validation has also been performed with real human brain datasets. This study includes data from 5 young healthy volunteers. The study was approved by the local internal review board and the volunteers provided informed consent. The images were acquired with a 3T Siemens Trio MRI system equipped with head coils. The acquisition protocol included 3D T_1w and $FLAIR$ sequences. The T_1w and $FLAIR$ sequences have a matrix of size $170 \times 512 \times 310$ with a voxel of resolution $1 \times 1 \times 1mm^3$ upsampled for clinical examination to $1 \times 0.5 \times 0.5mm^3$. All the volunteers datasets have been registered by taking the T_1w

Method	Brain Region	Side	$DICE_L$	Side	$DICE_L$
SyN	occipital lobe	L	0.11	R	0.19
B-Splines			0.34		0.48
Proposed			0.14		0.23
SyN	insula gyrus	L	0.14	R	0.21
B-Splines			0.55		0.55
Proposed			0.19		0.23
SyN	superior temporal gyrus	L	0.22	R	0.18
B-Splines			0.52		0.45
Proposed			0.23		0.19
SyN	parahippocampal gyrus	L	0.36	R	0.40
B-Splines			0.69		0.72
Proposed			0.41		0.42
SyN	superior frontal gyrus	L	0.34	R	0.35
B-Splines			0.60		0.58
Proposed			0.36		0.39
SyN	inferior gyrus	L	0.15	R	0.28
B-Splines			0.40		0.57
Proposed			0.15		0.32
SyN	precentral gyrus	L	0.29	R	0.27
B-Splines			0.53		0.48
Proposed			0.30		0.31
SyN	inferior parietal lobule	L	0.43	R	0.37
B-Splines			0.64		0.58
Proposed			0.45		0.38
SyN	cingulate gyrus	L	0.15	R	0.22
B-Splines			0.35		0.44
Proposed			0.16		0.22
SyN	temporal pole	L	0.22	R	0.25
B-Splines			0.66		0.66
Proposed			0.29		0.29
SyN	infero temporal region	L	0.41	R	0.41
B-Splines			0.70		0.67
Proposed			0.46		0.42
SyN	frontal pole	L	0.16	R	0.16
B-Splines			0.62		0.64
Proposed			0.25		0.25
SyN	middle frontal gyrus	L	0.29	R	0.35
B-Splines			0.54		0.56
Proposed			0.30		0.38
SyN	orbital frontal gyrus	L	0.25	R	0.29
B-Splines			0.64		0.66
Proposed			0.38		0.45
SyN	superior parietal lobule	L	0.31	R	0.35
B-Splines			0.52		0.58
Proposed			0.35		0.37
SyN	postcentral gyrus	L	0.28	R	0.23
B-Splines			0.50		0.40
Proposed			0.29		0.26

Table 4.2: Average performance and comparison of the proposed method with SyN and B-Splines on the labeled brain regions of the NIREP datasets. The higher value of $DICE_L$ indicates a better performance quality. The proposed method outperforms SyN in every region.

BrainWeb phantom as a reference.

The proposed method has been compared with the pairwise B-Splines based non-rigid registration method provided by BRAINSFit [139] and the SyN method implemented in ANTs [3, 75]. All the methods include also a rigid and an affine pre-registration step from ITK [133]. Rigid and affine registration steps have been used from the ITK library together with the Mattes implementation of MI [106] provided by ITK. These have been kept constant for all the experiments with all the methods to focus the comparison on only the non-rigid registration methods. For a fair comparison the best performing settings based on observation have been chosen for both the B-Splines and the SyN methods. In B-Splines the MI has been used as a metric for all the registration steps. For SyN the Cross Correlation (CC) metric has been chosen since it experimentally showed to outperform MI for the same contrast case. On the other hand, for SyN for the different contrasts case, the MI has shown a better performance than CC and therefore has been chosen. The tests have been performed on a workstation with an Intel Core2 Duo 3.0 GHz CPU and 16GB of RAM.

4.3.1 Same Contrast Brain Registration

This subsection describes the experiments performed on 5 healthy volunteers using same modality (T_1w MRI) and same contrast images. The value of σ_S for the spatial smoothing of the volunteers data has been set to 5 voxels. Fig. 4-5 shows an example of a same contrast registration between the T_1w BrainWeb phantom as reference and a T_1w image of a volunteer as moving. Fig. 4-6 shows the average images before and after the registration between the T_1w BrainWeb phantom and T_1w images from 5 volunteers.

The value of σ_S for the volunteers data has been set to 5 voxels. Fig. 4-5 shows an example of a same contrast registration between the T_1w BrainWeb phantom as reference and a T_1w image of a volunteer as moving. The misregistered image shown in Fig. 4-5b is the result of the rigid and affine registration steps that are used as pre-processing for the non-rigid registration method proposed. The first row of Fig. 4-6 shows the average images before and after the registration between the T_1w BrainWeb phantom and T_1w images from 5 volunteers.

In Table 4.3 are the results in terms of $\langle I_{stddev} \rangle_{\mathbf{x}}$ for same contrast registration. The proposed method has performed better in comparison with B-Splines.

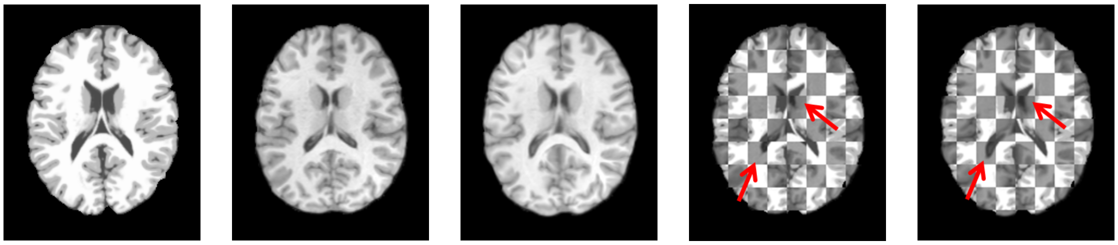

(a) Reference (b) Moving (c) Registered (d) Before (e) After

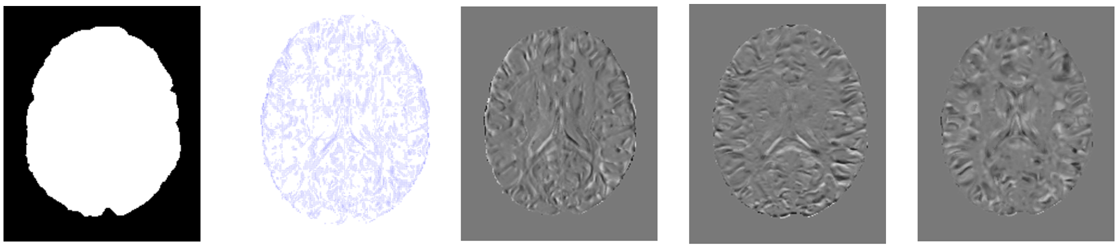

(f) ROI mask (g) Disp. field (h) Disp. u_x (i) Disp. u_y (j) Disp. u_z

Figure 4-5: A 2D axial slice of a 3D data from a volunteer T_1w dataset registered to the T_1w BrainWeb phantom. (a) is the reference image, (f) is the ROI used, (b) is the misregistered image, (c) is the registered image obtained with the proposed method. In (d) and (e) are the checkerboard compositions interleaving I_{ref} and I_{mov} before and after the registration. The red arrows highlight the effect of the registration on significant brain structures. In (g) is the recovered displacement field applied to (b) to obtain (c). (h), (i) and (j) are the transformations applied on the x, y and z axes, respectively. The brighter regions identify positive displacements, while dark regions identify negative displacements with a range of $+/-$ 4 voxels.

BrainWeb $T_1w - T_1w$ volunteers data

Method	$\langle I_{stddev} \rangle_{\mathbf{x}}$
No registration	44.34
SyN CC	22.44
B-Splines	25.82
Proposed	24.02

Table 4.3: Performance and comparison of the proposed method with no registration, SyN with CC, and B-Splines registration methods on T_1w images. A lower value of $\langle I_{stddev} \rangle_{\mathbf{x}}$ denotes a better quality performance. The proposed method on average outperforms B-Splines in terms of $\langle I_{stddev} \rangle_{\mathbf{x}}$.

4.3.2 Multicontrast Brain Registration

This subsection describes the experiments performed on 5 healthy volunteers using different modalities (T_1w and FLAIR MRI) and different contrast images. In Fig. 4-7 is an example of the multi-contrast registration between the T_1w BrainWeb phantom and a $FLAIR$ image

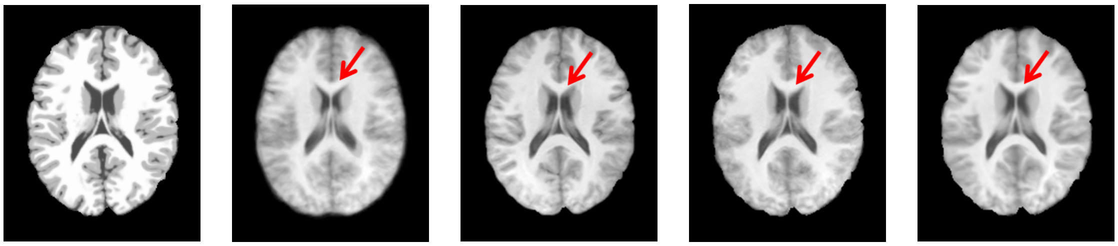

(a) Reference (b) Before (c) SyN CC (d) B-Splines (e) Proposed

Figure 4-6: A 2D axial slice of the average images of 3D real datasets. (a) is the reference image. (b) is the average image of T_1w real data before registration, (c) is the average T_1w image obtained with SyN using CC, (d) is the average image obtained with B-Splines, and (e) is the average image obtained with the proposed method. The red arrows highlight the effect of the registration on significant brain structures.

of a volunteer. The misregistered images shown in Fig. 4-5b and 4-7b are the results of the rigid and affine registration steps that are used as pre-processing for the non-rigid registration proposed. Fig. 4-8 shows the average images before and after the registration between the T_1w BrainWeb phantom and a $FLAIR$ image from 5 volunteers.

The value of σ_S for the volunteers data has been set to 5 voxels. In Fig. 4-7 is an example of the multi-contrast registration between the T_1w BrainWeb phantom and a $FLAIR$ image of a volunteer. The misregistered image shown in Fig. 4-7b is the result of the rigid and affine registration steps that are used as pre-processing for the non-rigid registration method proposed. The second row of Fig. 4-8 shows the average images before and after the registration between the T_1w BrainWeb phantom and a $FLAIR$ image from 5 volunteers.

In Table 4.4 are the results in terms of $\langle I_{stddev} \rangle_{\mathbf{x}}$ for different contrast registration. The proposed method has performed better in comparison with both B-Splines and SyN.

BrainWeb $T_1w - FLAIR$ volunteers data

Method	$\langle I_{stddev} \rangle_{\mathbf{x}}$
No registration	48.37
SyN MI	36.97
B-Splines	42.40
Proposed	33.06

Table 4.4: Performance and comparison of the proposed method with no registration, SyN with MI, and B-Splines registration methods on $FLAIR$ images. A lower value of $\langle I_{stddev} \rangle_{\mathbf{x}}$ denotes a better quality performance. The proposed method on average outperforms both SyN and B-Splines in terms of $\langle I_{stddev} \rangle_{\mathbf{x}}$.

In Table 4.5 are the comparative results of the proposed method applied to the T_1w-

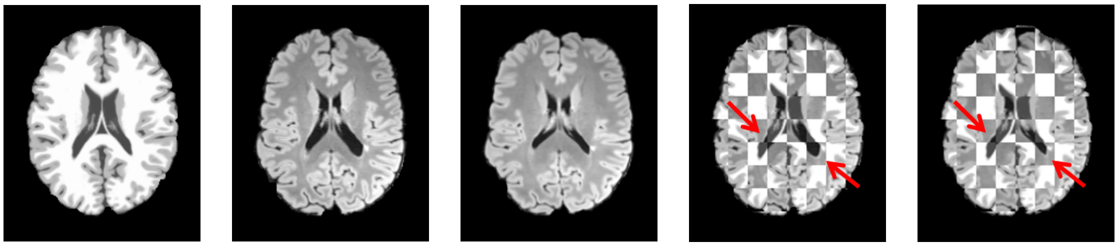

(a) Reference (b) Moving (c) Registered (d) Before (e) After

(f) ROI mask (g) Disp. field (h) Disp. u_x (i) Disp. u_y (j) Disp. u_z

Figure 4-7: A 2D axial slice of a 3D data from a volunteer $FLAIR$ dataset registered to the T_1w BrainWeb phantom. (a) is the reference image, (f) is the ROI used, (b) is the misregistered image, (c) is the registered image obtained with the proposed method. In (d) and (e) are the checkerboard compositions interleaving I_{ref} and I_{mov} before and after the registration. The red arrows highlight the effect of the registration on significant brain structures. In (g) is the recovered displacement field applied to (b) to obtain (c). (h), (i) and (j) are the transformations applied on the x, y and z axes, respectively. The brighter regions identify positive displacements, while dark regions identify negative displacements with a range of $+/-$ 4 voxels.

$FLAIR$ volunteers datasets. The proposed method over the multicontrast datasets showed a better performance in terms of both SAD_{Imp} and in terms of the MI_{Imp} compared to both the B-Splines and the SyN methods. The quantitative results and comparisons of the proposed method to those of B-Splines and SyN applied over the 16 T_1w datasets of the NIREP database are shown in Table 4.2. The proposed method over these same contrast datasets performs better than SyN in terms of $DICE_L$ for almost all the labeled regions.

In Table 4.3 and Table 4.4 are the results in terms of $\langle I_{stddev} \rangle_{\mathbf{x}}$ for same contrast and different contrast volunteer datasets, respectively. The proposed method performed better than the B-Splines method for the same contrast cases and performed better than both the B-Splines and the SyN methods for the different contrasts cases. In the case of same contrast registration the validation for these data sometimes shows comparable performance to either the B-Splines or the SyN methods. However, in all cases the non-optimized implementation of the proposed method had typically 260% lower working memory requirement compared

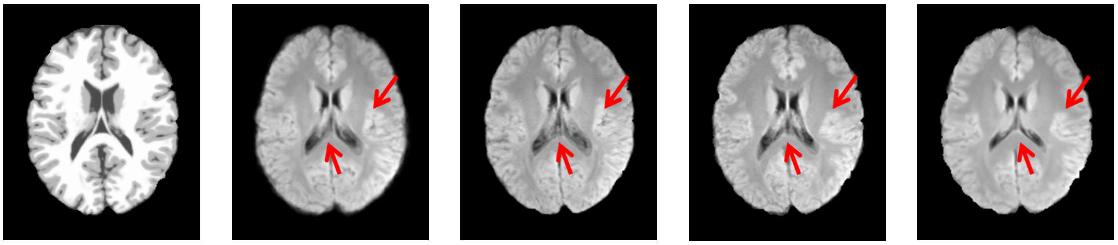

(a) Reference (b) Before (c) SyN MI (d) B-Splines (e) Proposed

Figure 4-8: A 2D axial slice of the average images of 3D real datasets. (a) is the reference image. (b) is the average image of $FLAIR$ real data before registration, (c) is the average $FLAIR$ image obtained with SyN using MI, (d) is the average image obtained with B-Splines, and (e) is the average image obtained with the proposed method. The red arrows highlight the effect of the registration on significant brain structures.

to the B-Splines method as also shown in Table 4.6. In most cases the proposed method was more efficient than the SyN method as well. The full operating resolution of the proposed method has enabled the better localization of region boundaries such as those of the ventricles in Fig. 4-8 compared to both the B-Splines and the SyN methods.

Datasets	Method	MI_{Imp}	Resol. (voxels)	Exec. time	Memory Space
Volunteer 1, $FLAIR$	SyN	48.23%	1	~18min	450MB
	B-Splines	51.65%	1/3372	~2min	4GB
	Proposed	57.14%	1	~90min	2GB
Volunteer 2, $FLAIR$	SyN	48.48%	1	~18min	450MB
	B-Splines	44.65%	1/3372	~2min	4GB
	Proposed	58.39%	1	~90min	2GB
Volunteer 3, $FLAIR$	SyN	33.91%	1	~18min	450MB
	B-Splines	34.47%	1/3372	~2min	4GB
	Proposed	35.83%	1	~90min	2GB
Volunteer 4, $FLAIR$	SyN	50.01%	1	~18min	450MB
	B-Splines	18.70%	1/3372	~2min	4GB
	Proposed	52.32%	1	~90min	2GB
Volunteer 5, $FLAIR$	SyN	27.16%	1	~18min	450MB
	B-Splines	32.13%	1/3372	~2min	4GB
	Proposed	29.29%	1	~90min	2GB

Table 4.5: Performance and comparison of the proposed method with that of B-Splines optimized in B-Splines and that of SyN optimized in SyN for five $T_1w - FLAIR$ volunteers datasets. The higher value of MI_{Imp} of the proposed method denotes its better performance quality.

4.4 DCE-MRI Datasets

The analysis of Dynamic Contrast Enhanced Magnetic Resonance Imaging (DCE-MRI) data plays an important role for the identification of vital tumors in the thoracic, abdominal, and pelvic regions. The injection of a contrast agent and its temporal accumulation in tissues can highlight both healthy anatomy as well as lesions aiding a medical doctor in lesion identification and in monitoring perfusion properties of lesions during anti-angiogenic therapies. In particular, the intensity and contrast in DCE-MRI time series varies significantly along time. The data interpretation to obtain sufficient and precise information about disease progression and treatment requires automated analysis. This is complicated, however, by patient motion and complex physiological movements such as those due to breathing, heart beat, and peristalsis that may introduce spatial misregistration in the data along time.

Many of the methods introduced in Chapter 2 can also be extended and used for DCE-MRI registration, usually by repeating a pairwise registration approach along time. Such methods can be applied to different internal organs and body regions resulting from DCE-MRI acquisitions. Registration of contrast enhanced data of human breasts has been proposed by different authors such as Rueckert et al. [1], Rohlfing et al. [44], Vignati et al. [140], and Dimitriev et al. [93] who performed the non-rigid registration using the method proposed by Rueckert and its extensions. This registration method for breast registration has also been validated in the work of Tanner et al. [96]. Other methods have been proposed for the DCE-MRI breast non-rigid registration such as the optical flow based method in Martel et al. [64] which combines a multiresolution optical flow formulation with NMI to perform the registration.

Another organ that is commonly imaged with DCE-MRI is the human heart. Due to the high perfusion and movement present during the acquisition of the images, these datasets need to be first registered before being subsequently analyzed. Contrast agents used for DCE-MRI sequences are normally described by intensity over time curve models which can distinguish between different tissue types. Adluru et al. [141] suggested to use the curve model fit to estimate the spatiotemporal registration. In their work Zakkarov et al. [142] use both B-Splines and Demons based methods together with MI to perform the cardiac non-rigid registration of subsequent images. Li et al. [143] impose spatiotemporal smoothness constraints to obtain a pseudo motion-free ground truth model which is used as reference for the registration.

In the abdominal area organs such as kidneys, liver, and prostate have been placed in the same space with a variety of methods. The B-Splines based registration methods together with MI have also been used to register kidney DCE-MRI datasets [92, 108]. Registration of kidney DCE-MRI datasets have also been performed with other methods such as the one proposed by Ruthotto et al. [144] that estimates a local linear transformation together with a hyperelastic regularizer to obtain a multicontrast non-rigid registration. A B-Splines based registration method has also been used by Noterdaeme et al. [145] to perform non-rigid registration over DCE-MRI datasets of human liver. Melbourne et al. [121] proposed a statistical based registration method that uses PCAs to progressively register spatiotemporal liver datasets. Chappelow et al. [146] focused on the registration of prostate data proposing a new metric called MultiAttribute Combined Mutual Information (MACMI) which allows to register many different medical imaging modalities at the same time. For example MACMI allows to register T_1w and T_2w MRI to histology datasets.

The NParBR method has been tested and extensively validated with different DCE-MRI datasets of organs belonging to thorax, abdominal, and pelvic regions and compared to the most commonly used and well accepted registration methods such as B-Splines and SyN based ones.

4.4.1 Thorax and Abdomen

The patient data in this study include liver datasets from 4 patients [147], lung datasets from 3 patients and intestines datasets from 3 patients. All patient datasets were acquired in regular free breathing with an 1.5T MRI scanner (Sonata, Siemens/Erlangen) using a 3D Flash pulse sequence. The images at every time point consist of 20 slices of 128×128 pixels with an in-plane spacing of 3.1mm and a slice thickness of 3.5mm. The scan lasted a total of 6 minutes and produced a time series of 72 images with a time resolution of 5sec. The value of σ_S has been set to 3mm for all axes and for the datasets. A manual segmentation of the main lesion for all liver, lung, and intestines datasets has been done by experts, tracking also the displacement of the lesion along time.

In Table 4.6 are the average quantitative results of $SAD_{Imp,t}$ for all the datasets grouped by organ. The NParBR method shows a better performance in terms of $SAD_{Imp,t}$ in com-

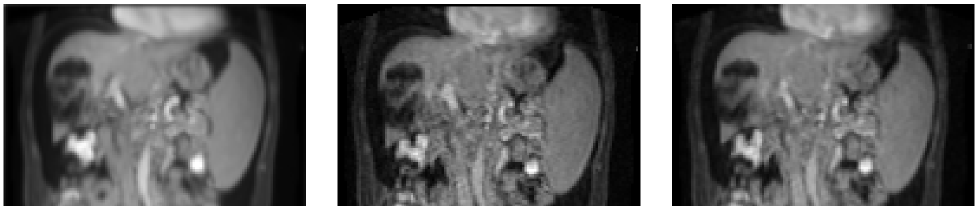
(a) Reference (b) Moving (c) Registered

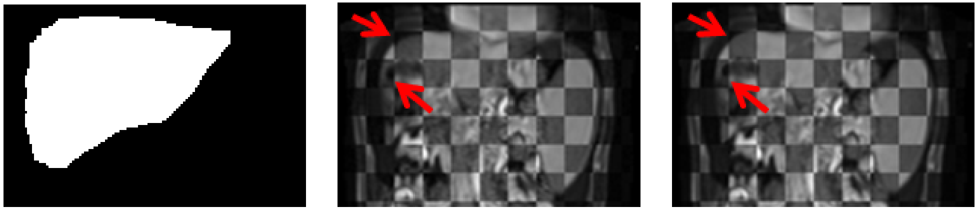
(d) ROI mask (e) Before (f) After

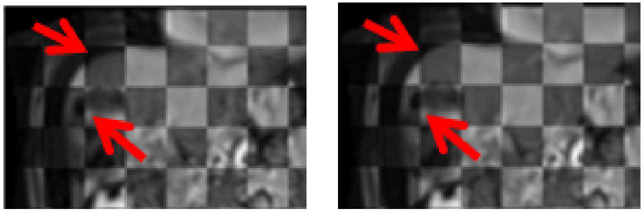
(g) Before (h) After

Figure 4-9: A coronal section from the volumetric registration of a real dataset of liver. In the original resolution images (e), (f), and in the relatively highly zoomed sub-images (g), and (h) the arrows point to improved continuity along the contour as a result of the registration.

parison to both the SyN and the B-Splines for the liver datasets. The average quantitative results in terms of $MI_{Imp,t}$ are presented in Table 4.6 for all datasets, grouped by organ. The presented method shows a better performance in terms of $MI_{Imp,t}$ in comparison to both the SyN and the B-Splines for the liver and the lungs datasets. The average quantitative results of $\sigma_{bin,Imp}$ of the NParBR method compared with the ones obtained with the SyN and the B-Splines are presented in Table 4.6 and showed that the NParBR method has the best performance. The results regarding the RES_{Imp} value have also been grouped by organ and show a better performance of NParBR in comparison with the SyN and the B-Splines on the liver and the intestines datasets as shown in Table 4.6. The Wilcoxon matched pair test revealed a statistical significant difference between the residuals RES_{bef} and RES_{aft} with a confidence level of $p < 0.005$ after the applied registrations. This showed the improved performance for NParBR for all liver, lungs, and intestines datasets.

The kymograms along axial direction of the patient in Fig. 4-10 are shown in Fig. 4-

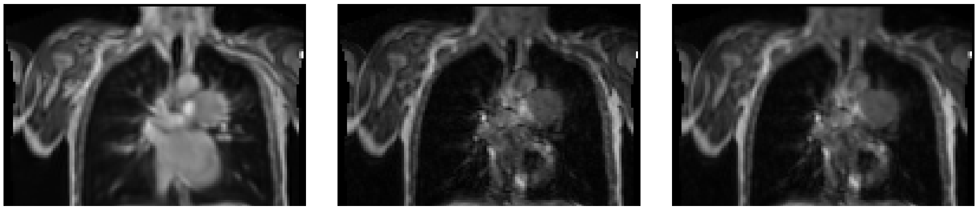
(a) Reference (b) Moving (c) Registered

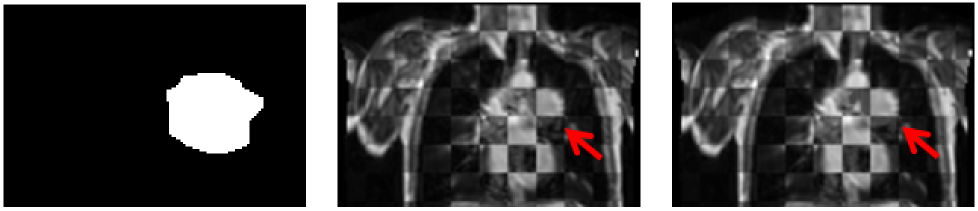
(d) ROI mask (e) Before (f) After

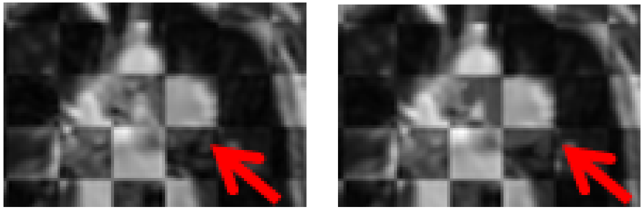
(g) Before (h) After

Figure 4-10: A coronal section from the volumetric registration of a real dataset of a lung. In the original resolution images (e), (f), and in the relatively highly zoomed sub-images (g), and (h) the arrow points to an improvement to a continuity of the contour of the lesion as a result of the registration.

14. In particular, the kymogram resulting from the axial window demonstrates that the registration significantly compensates the movement due to breathing.

The registration has also been evaluated with visual observation by comparing images before and after registration using a checkerboard pattern. In Fig. 4-9, 4-10, and 4-11 are axial sections from volumetric registration of liver, lungs, and intestines datasets, respectively. The application of the registration method results in a better alignment of the lesions as shown in Fig. 4-9, and 4-10. Some example locations are pointed out by the red arrows. In Fig. 4-11 is a challenging example of an intestine dataset which after registration still showed misalignment. The NParBR method has been found to improve the overall performance for liver and lungs datasets. It also showed the best relative performance for intestines datasets. The NParBR method also showed the best computational efficiency while working at full spatial resolution.

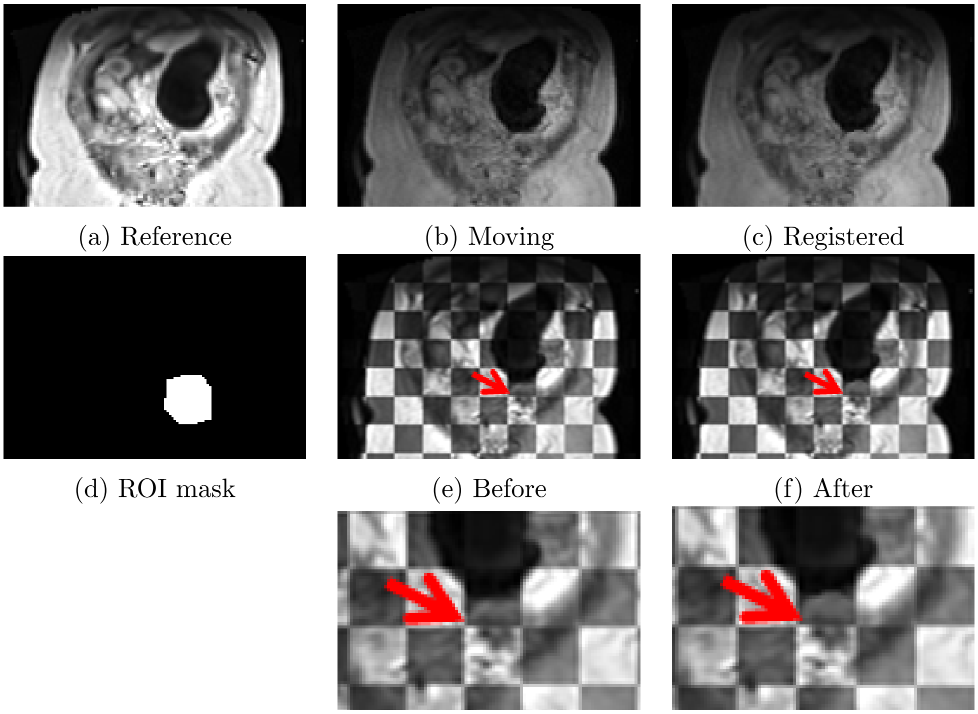
(a) Reference (b) Moving (c) Registered

(d) ROI mask (e) Before (f) After

(g) Before (h) After

Figure 4-11: A coronal section from the volumetric registration of a real dataset of intestines. In the original resolution images (e), (f), and in the relatively highly zoomed sub-images (g), and (h) the arrow points to a very small lesion which is not registered satisfactorily.

4.4.2 Pelvis

Prostate datasets from 10 patients were also considered and analyzed. They have been acquired with a 3T MRI scanner (TIM-Trio, Siemens/Erlangen) using a 3D Flash pulse sequence. The images at every time point consist of 28 slices of 192×150 pixels with an in-plane spacing of 1.8mm and a slice thickness of 3.5mm. The scan lasted a total of about 7min and produced a time series of 50 images with a time resolution of 8sec. The value of σ_S has been set to 3mm for all axes and for the prostate datasets.

In Table 4.6 are the average quantitative results of $SAD_{Imp,t}$ for all the datasets grouped by organ. The NParBR method shows a better performance in terms of $SAD_{Imp,t}$ in comparison to both the SyN and the B-Splines for the prostate datasets. The average quantitative results in terms of $MI_{Imp,t}$ are presented in Table 4.6 for all datasets, grouped by organ. The presented method shows a better performance in terms of $MI_{Imp,t}$ in comparison to both the SyN and the B-Splines for the prostate datasets. The average quantitative results of $\sigma_{bin,Imp}$ of the NParBR method compared with the ones obtained with the SyN

(a) Reference (b) Moving (c) Registered

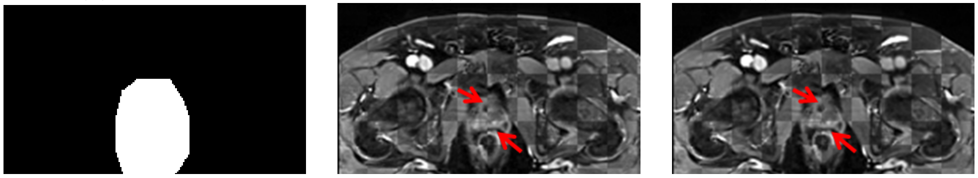

(d) ROI mask (e) Before (f) After

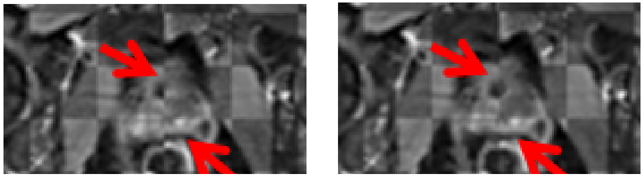

(g) Before (h) After

Figure 4-12: An axial section from the volumetric registration of a real dataset of a prostate. In the original resolution images (e), (f), and in the relatively highly zoomed sub-images (g), and (h) the arrows point to improvements in alignment as a result of the registration.

and the B-Splines are presented in Table 4.6 and showed that the NParBR method has the best performance. The results regarding the RES_{Imp} value show a comparable performance of NParBR with the SyN and the B-Splines on prostate datasets as shown in Table 4.6. The Wilcoxon matched pair test revealed a statistically significant difference between the residuals RES_{bef} and RES_{aft} with a confidence level of $p < 0.005$ after the applied registrations.

The registration has also been evaluated visually by comparing images before and after registration using a checkerboard pattern. In Fig. 4-12 are axial sections from volumetric registration of prostate datasets. The application of the registration method results in a better alignment of the lesions as shown in Fig. 4-12. Some examples are pointed by the red arrows. The NParBR method has been found to improve the overall performance for prostate datasets. The NParBR method also showed the best computational efficiency while working at full spatial resolution.

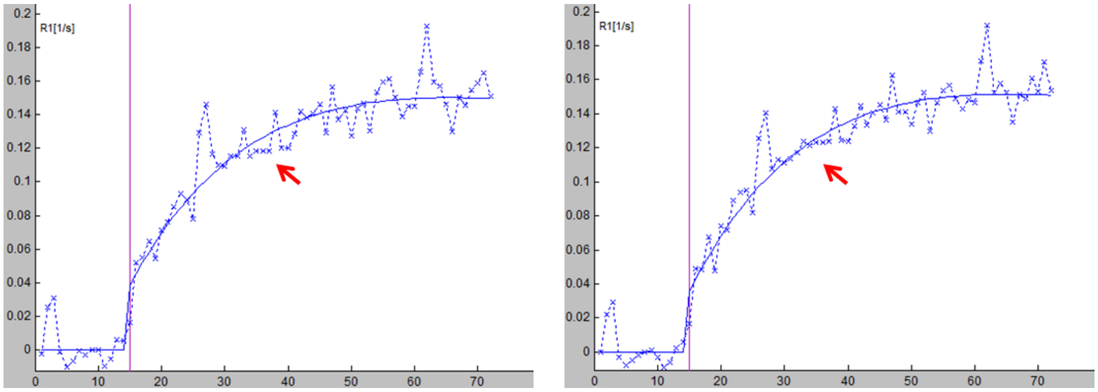

(a) Raw data (b) SyN

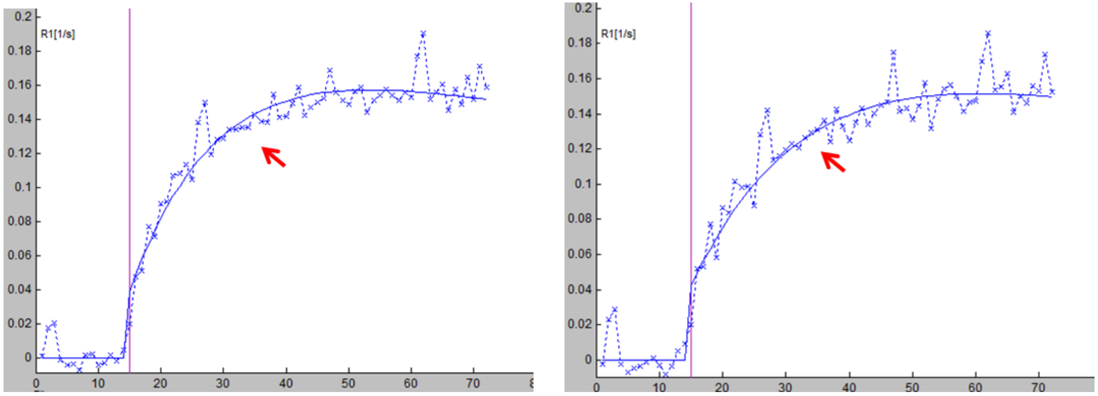

(c) B-Splines (d) NParBR

Figure 4-13: Plots of the pharmacokinetic model fitting over one temporal 3D dataset. The red arrows point to improvements in model fitting after the registration.

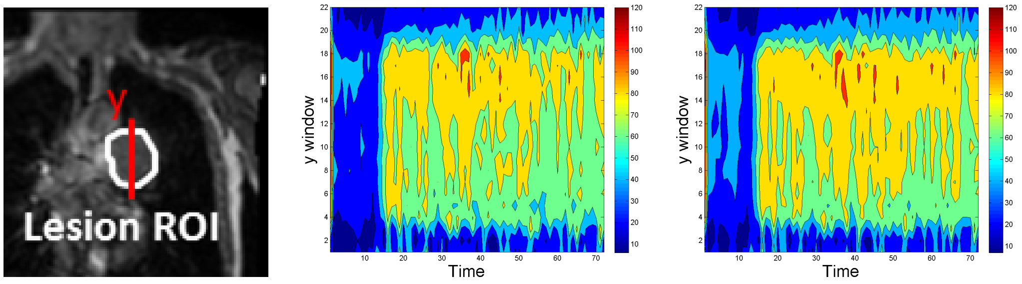

(a) Lesion (b) Before registration (c) SyN

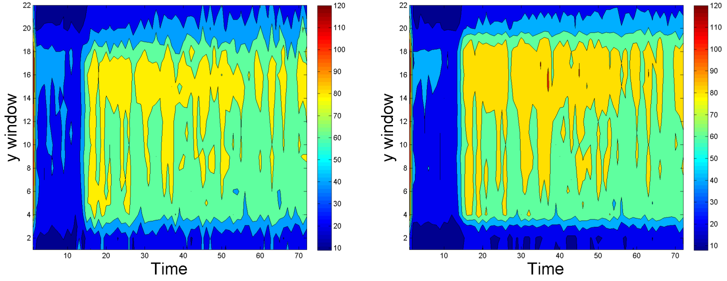

(d) B-Splines (e) NParBR

Figure 4-14: Evaluation with visual observation of the registration for the dataset shown in Fig. 4-10. In (a) is the image of the lesion in lung. In (b) is the kymogram resulting from a 1D axial window before the registration. In (c), (d), and (e) are the kymograms resulting from a 1D axial window after the registration with the SyN, the B-Splines, and the NParBR methods. The NParBR method performs a better motion compensation, which can be seen with the significant increase in smoothness along time in (e).

Datasets	Method	SAD_{Imp}	MI_{Imp}	$\sigma_{bin,Imp}$	RES_{Imp}	Resol. (voxels)	Avg. Time (hrs)	Wilcoxon p-values
Avg. over 4 liver datasets	SyN	-13.22%	3.75%	-13.31%	7.56%	1	~15	0.22
	B-Splines	14.52%	26.40%	-49.51%	12.66%	1/82	~12	0.22
	NParBR	21.26%	31.37%	16.49%	23.95%	1	~6	~ 0
Avg. over 3 lungs datasets	SyN	6.27%	19.41%	-28.04%	12.67%	1	~13	0.001
	B-Splines	20.38%	21.57%	-82.20%	46.63%	1/82	~11	~ 0
	NParBR	19.55%	27.76%	1.95%	22.90%	1	~5	~ 0
Avg. over 3 intestines datasets	SyN	5.79%	-5.62%	-79.19%	-9.57%	1	~14	0.002
	B-Splines	15.87%	8.11%	-206.11%	-113.72%	1/82	~12	~ 0
	NParBR	12.54%	-3.17%	-22.58%	2.33%	1	~6	~ 0
Avg. over 10 prostate datasets	SyN	5.44%	1.25%	N/A	0.32%	1	~12	0.087
	B-Splines	11.71%	10.03%	N/A	12.24%	1/216	~10	0.004
	NParBR	21.89%	25.28%	N/A	-2.84%	1	~8	~ 0

Table 4.6: Comparison of NParBR with SyN and B-Splines. Higher values for all the SAD_{Imp}, MI_{Imp}, $\sigma_{bin,Imp}$, and RES_{Imp} denote a better performance. NParBR generally shows improved or at least comparable performance in particular in terms of MI_{Imp} and $\sigma_{bin,Imp}$, while its average computation time is comparatively significantly lower. In all cases the NParBR method shows a statistical significance with a confidence level of $p < 0.05$.

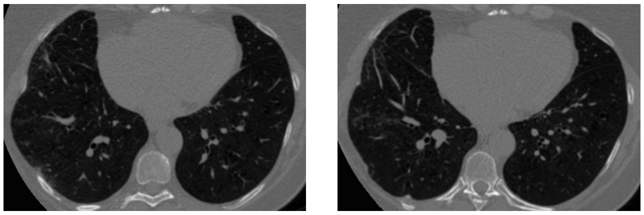

(a) Reference (b) Moving

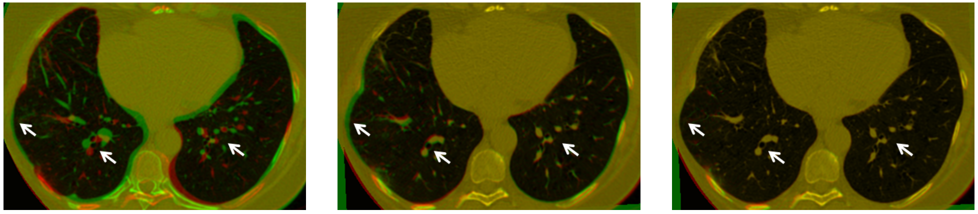

(c) Before Registration (d) After rigid/affine (e) After NParBR

Figure 4-15: An axial section from the volumetric registration of a human lung CT dataset from the EMPIRE10 challenge [8]. In (a) and (b) are the input reference and moving images, respectively. Finally in (c), (d), and (e) are the resulting overlaps before the registration, after rigid/affine registration, and after NParBR non-rigid registration, respectively. The white arrows point at structures that are better aligned after the NParBR non-rigid registration.

4.5 EMPIRE 10 Lungs CT Benchmark

The evaluation of non-rigid image registration algorithms is a nontrivial task due to the diversity of the datasets to which it can be applied. To address this problem, a public platform named EMPIRE10 (Evaluation of Methods for Pulmonary Image REgistration 2010) has been proposed as a challenge of the MICCAI conference [8]. The purpose of this benchmark is to provide the researchers with datasets whose results are evaluated using the methodology described in [8] and consequently make the various methods objectively comparable. The datasets provided from the EMPIRE10 challenge consist of 30 CT scan pairs of lungs. Each pair has been taken from the same subject, for intra-patient registration. The 30 datasets are subdivided into 6 different categories to cover a wide set of practical cases. Eight scan pairs consist of two inspiration scans (I/I), eight scan pairs consist of breathhold inspiration/expiration (I/E), four cases consist of two individual phases of a 4-D dataset (4D), four ovine datasets (Ov), two contrast/non-contrast scan pairs (Co), and finally four artificially warped scan pairs (Wa). The details concerning the acquisition of the datasets are provided in [8]. The NParBR method has also been tested with the EMPIRE10 datasets for a further comparison with the state-of-the-art registration methods. The non-rigid registration has been performed within the ROIs corresponding to the lungs volumes, segmented using the method of van Rixoort et al. [148] as provided by the EMPIRE10 challenge.

The Wiener Filtering of the joint intensity statistics was performed in the Fourier domain using the forward and backward FFT provided by ITK [133]. The value of σ_δ has been set for all datasets to 3 and is accumulated along the iterations to give the total Gaussian distortion of the joint intensity statistics. The value of ϵ of the Wiener Filter has been set to 0.1 for all datasets. The spatial regularization $G(x; 0, \sigma_S)$ has been performed using the efficient separable implementation of the 3D Gaussian Filter from ITK [133]. The value of σ_S has been set equal to the length of the side of an in-plane voxel in 3D for all datasets. A maximum number of $k_{max} = 100$ iterations is enforced for the non-rigid registration. In Fig. 4-15 and in Fig. 4-16 are examples of the application of the NParBR method over human dataset number 05 and on sheep dataset number 04, respectively. The structures highlighted with the arrows show an improved alignment after the non-rigid registration step compared to original and rigidly/affinely registered images. Further validation is performed according to the evaluation protocol of the EMPIRE10 challenge [8] and the results have been published on the EMPIRE10 challenge website. In Table 4.7 are the average results obtained with the NParBR method. The detailed results obtained with the NParBR method are presented in Section 6.1. Under the assumed condition of small residual displacements of the lung structures, the NParBR method showed no error for the alignment of the lung boundaries and fissures and a small error for the landmarks alignment as well as small presence of singularities. On the other hand, when the residual displacement after the rigid and affine registration steps was still large the NParBR method performed poorly in all evaluation categories. These limitations will be taken into consideration for the future development of a more robust version of the NParBR method which will be able to accommodate also the estimation of large displacements in images with fine texture.

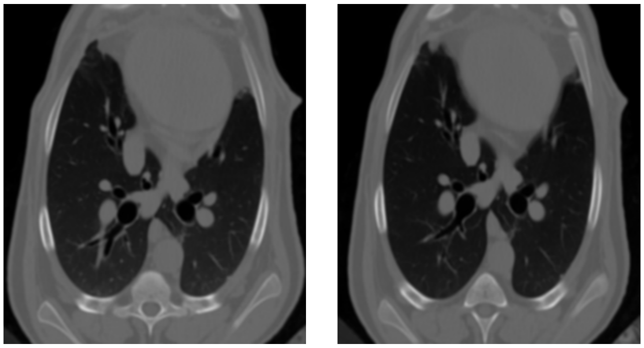

(a) Reference (b) Moving

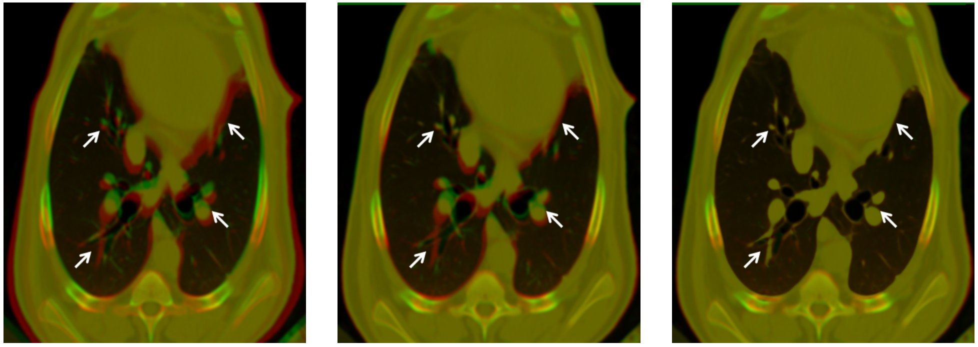

(c) Before Registration (d) After rigid/affine (e) After NParBR

Figure 4-16: An axial section from the volumetric registration of a sheep lung CT dataset from the EMPIRE10 challenge [8]. In (a) and (b) are the input reference and moving images, respectively. Finally in (c), (d), and (e) are the resulting overlaps before the registration, after rigid/affine registration, and after NParBR non-rigid registration, respectively. The yellow color denotes good alignment. The white arrows point at structures that are better aligned after the NParBR non-rigid registration.

	Min	Max	Average
Lung Boundaries	0	6.84875	1.97773
Fissures	0	13.5872	2.55263
Landmarks	0.176431	13.5489	5.03523
Singularities	6.07183e-06	1.09825	0.125658

Table 4.7: Average results of the NParBR method over all the EMPIRE10 challenge datasets. When the displacements of the small internal structures of the lungs such as the alveoli are comparable to their sizes, the NParBR method showed a good performance.

Chapter 5

Summary and Discussion

This thesis has presented an alternative solution to the ill-posed problem of non-rigid registration with a particular focus to its application in medical imaging. The major contribution of this work has been the development and the validation of a robust and efficient method for accurate non-rigid registration of different medical images, with a particular focus on human brain MRI as well as DCE-MRI datasets of thoracic, abdominal, and pelvic organs such as lungs, liver, intestines, and prostate.

The proposed pairwise registration is based on a non-parametric Bayesian formulation for the estimation of the misregistration and its removal. It can accommodate datasets of both same as well as variable image contrast. The implementation is iterative and results in an effective deconvolution of the joint intensity statistics that only requires a single computation of the joint intensity statistics and spatial smoothing of the estimated registration per iteration. The consecutive estimation of a displacement and its spatial regularization has been used for the optimization and implementation of the Demons method [2] as well as for other registration methods [1, 75, 149]. The method restores the joint intensity histogram non-parametrically by removing the effect of the misregistration and by preserving the form of the joint intensity statistics. The restored statistics are then back-projected to the image. The statistical restorations together with spatial smoothness give a spatially continuous registration that can be approximately volume preserving for the different anatomic regions. That is, the determinant of the Jacobian of the transformation is approximately equal to unity everywhere in the image domain [4]. This property is reasonable for DCE-MRI data since the lesion size is not expected to change due to breathing

[4]. A misregistration particularly multicontrast can be accounted for if it gives rise to a distribution in the statistics whose size is above that of the SNR in the Wiener filter, $\epsilon = \frac{1}{SNR}$. A small region that corresponds to very small distributions with densities low compared to the SNR are not restored and the registration is not effected. However, for the case of DCE-MRI data the blood supply occurs over extensive regions and creates distributions in the statistics that have a sufficiently large size.

The assumptions on which the NParBR method is based on and for which it converges are for typical, highly probable, medical images and mis-registrations. A typical image consists of extensive tissue regions of uniform intensity or texture separated by smooth boundaries. It also assumes that the extent of the mis-registration is limited compared to the extent of the tissue regions and as a consequence also of the ROI. Non-typical, unlikely medical images, can have a small or no overlap between corresponding tissue lesions in I_{ref} and I_{mov} and a low contrast between lesions and healthy tissue. Such non-typical images can limit the effectiveness of this as well as other intensity-based registration methods. The considered intestines datasets present some of these difficulties since the lesions are small and with limited contrast compared to the healthy tissue such as the example shown in Fig. 4-11. The registration of the intestines datasets has been the most challenging. However, as shown in Table 4.6, the NParBR method still obtained the best relative performance in terms of $\sigma_{bin,Imp}$ and RES_{Imp} for these challenging datasets. The spatial neighborhood $\mathcal{N}$ is used to calculate second order statistics that can be used for the estimation and removal of misregistration and have helped the NParBR method to improve performance in such difficult cases. In the case of datasets with limited motion such as the presented intestines or prostates datasets, all the considered methods showed in general a lower performance in terms of $\sigma_{bin,Imp}$ and RES_{Imp} compared to the non-registered datasets due to a more general parametrization of the methods. In such cases the misregistration can be smaller than the precision reachable with manual annotation and tracking of the lesions used for the evaluation, affecting consequently the relative performance metrics.

The performance of this method as well as of all methods based on image statistics can be improved if computed over a spatial ROI of meaningful contrast. The method developed significantly improves efficiency and accuracy of non-rigid registration of DCE-MRI datasets also because it is operating at full spatial resolution, which is significantly higher than that of the B-Splines method. The effectiveness and the convergence of the method has been shown empirically with datasets of a variety of anatomic regions with several different types of displacements. It is also assumed that sharper statistics minimize the misregistration error and lead to convergence similarly to the eventual magnetization following a hysteresis effect [82, 83].

The proposed method improves the efficiency and the accuracy of non-rigid registration in most cases for same contrast brain MRI datasets as well as in all cases for different contrasts brain MRI datasets while operating at full spatial resolution. The method shows an improvement compared to B-Splines and SyN methods qualitatively in terms of visual observation as well as quantitatively in terms of SAD_{Imp}, and MI_{Imp} for both phantoms and real datasets. The NParBR method has also demonstrated an effective registration for the liver breathing motion that can be up to 5.5cm in full inspiration and is one of the most extensive in the human body [150]. Another advantage of the method is that it is robust even to the anisotropic resolution present in the clinical imaging data of this study. The robustness of the method has also been demonstrated by evaluating it with a variety of body anatomic regions including datasets from the brain, the liver, the lungs, and the prostate.

The proposed method has also shown an improvement in terms of $\langle I_{stddev} \rangle_{\mathbf{x}}$ for brain datasets when compared to the registered images resulting from both B-Splines and SyN. It has also been shown to outperform the SyN method in terms of $DICE_L$ for the $NIREP$ datasets. Moreover, the NParBR method showed the best performance in terms of $\sigma_{bin,Imp}$ for all DCE-MRI datasets and in terms of SAD_{Imp} and MI_{Imp} for liver and prostate datasets. The registered DCE-MRI datasets lead to improved fitting in the pharmacokinetic modeling in terms of reduced fitting residuals compared to the fitting obtained without registration. The NParBR method also showed the best performance in terms of RES_{Imp} for liver, lungs, and intestines datasets.

The NParBR method has also been tested on 30 lung datasets from the EMPIRE10 challenge, showing a satisfactory performance only on datasets that present a limited displacement of small internal lung structures such as the alveoli. The estimation of large displacements may not satisfy the original assumption for the application of the NParBR method, that results in a lower registration quality when compared with state-of-the-art methods.

The complexity of the atlas calculation used for DCE-MRI registration is dependent upon the pairwise registration method that is common to all considered methods. The complexity of the NParBR method operating at full spatial resolution is significantly lower compared to those of the multicontrast extension of the B-Splines method by combining them with MI for the same spatial resolution as well as of the SyN method. The most common intensity based registration methods use MI that achieves its global optimum for unimodal joint statistics that raises more degrees of freedom than necessary. This leads to significantly higher computational cost for pairwise registration that for DCE-MRI datasets also has to be multiplied by the length of the time series. It also does not make any assumption about the misregistration. These limitations of the MI can have a drastic effect on the joint intensity distribution and have to be addressed by using extensive spatial regularization, which is computationally demanding. The main computational improvement of the NParBR method for a pairwise registration is that it requires the computation and the deconvolution of the joint intensity statistics as well as of the spatial smoothing only once per displacement estimation and spatial smoothing.

This is in contrast to the B-Splines method extended with the MI that requires the joint intensity statistics estimation and the spatial smoothing of order $|\mathcal{N}|$ times for each grid node to cover the entire image in an iteration. The registration in DCE-MRI must be applied to a time sequence that makes traditional methods not practical mainly due to the computational cost, which increases polynomially with the dimensionality of the images. The registration of volumetric time series makes the NParBR method orders of magnitude more efficient and even more advantageous for the case of higher dimensional registration. A detailed description of comparative costs is given in Section 3.7.

The non-rigid registration method developed in this work makes the complete registration of a DCE-MRI time series effective and practical and enables the dense spatial registration in a manner robust to temporal contrast changes and spatial anisotropy typically present in clinical data. The application of the NParBR method will be extended to volumetric datasets of other anatomic regions and acquired with other medical imaging modalities. The statistical method will also be evaluated with more complicated prior models for the distortion of the statistics as well as with different approaches for the spatial regularization. The NParBR will also be extended by implementing a spatial multiresolution approach to improve the robustness in the estimation of large displacements such as those of the small lung structures that happen in several datasets in the EMPIRE10 benchmark.

Also more general deconvolution such as Wiener for bi-modal Gaussian or multi-modal Gaussian or even blind decovolution will be considered for future extensions of the NParBR method. A further extension will be the implementation of a higher-dimensional registration which implies the creation of higher-dimensional joint intensity statistics. According to the theoretical estimation of time performance explained in Section 3.7, the NParBR method should show a dramatic increase in time performance, when compared to the state-of-the-art methods such as B-Splines and SyN. Possible applications of a higher-dimensional registration are the unbiased registration of an intra-patient time-series datasets and also the creation of a minimally biased atlas at a reasonable time cost.

Chapter 6

Appendix

6.1 Detailed Results for the EMPIRE10 Lung CT Challenge

In this section are the detailed results obtained with the NParBR method for the EMPIRE10 challenge datasets [8]. The evaluations have been performed considering the alignment of the lung boundaries, the alignment of the major lung fissures, the correspondence of selected landmarks, and the presence of singularities. The values presented in this section are summarized in Table 4.7. The detailed description of the datasets and the evaluation methods are described in [8].

6.1.1 Lung Boundary Results

To evaluate the alignment of the lung boundaries, the lungs are firstly segmented using the method of van Rixoort et al. [148]. The segmentations provide the lung boundaries, which are used to generate lung boundaries images. Mediastinal (central) regions of left and right lungs are masked out separately by placing a sphere centered in the center of mass of both lungs together whose radius correspond to the Euclidean distance from the center of mass of both lungs combined to the center of mass of each lung separately. Points within 20mm of the lung boundary are marked excluding those within 2mm of the boundary. Points inside and outside the lung boundaries are distinguished using the lung segmentation image and marked with different values. For each registration of each scan pair the following statistics are calculated:

- The percentage of checked points in the left lung for which penalties incurred

- The percentage of checked points in the right lung for which penalties incurred
- The percentage of checked points in the upper lung for which penalties incurred
- The percentage of checked points in the lower lung for which penalties incurred
- Score boundary, the percentage of total checked points for which penalties incurred (This is the overall score in the lung boundary category)

The detailed results of lungs boundary alignment obtained with the NParBR method are shown in Table 6.1.

6.1.2 Fissure Results

Fissures represent important physical boundaries which divide the lungs into regions known as lobes. Therefore, the major fissures have been used for the evaluation of registration methods in the EMPIRE10 challenge. The fissures in all images are segmented using the automated algorithm of van Rikxoort et al. [151]. A distance transform image is generated from the resulting fissure segmentation image. Points within 20mm of the fissure segmentation are marked, excluding those within 2mm from the fissure to allow for minor inaccuracies in the segmentation. Points which are not directly above or below a fissure voxel (looking at the axial direction) are excluded to prevent the marked regions from wrapping around the edges of the fissure plates. For each registration of each scan pair the following statistics are calculated:

- The percentage of checked points in the left lung for which penalties incurred
- The percentage of checked points in the right lung for which penalties incurred
- S fissure, The percentage of total checked points for which penalties incurred (This is the overall score in the fissure category)

The detailed results of lungs fissures alignment obtained with the NParBR method are shown in Table 6.2.

Scan Pair	**Left Lung (% Error)**	**Right Lung (% Error)**	**Upper Lung (% Error)**	**Lower lung (% Error)**	**Score (% Error Overall)**
1	7.21656	6.45356	5.87292	7.49495	6.84875
2	0	0	0	0	0
3	0.004664	0.322699	0.000965	0.302094	0.157597
4	0.0117	0.001015	0.010819	0	0.00545
5	0	5.90E-05	0	5.57E-05	2.87E-05
6	0	0	0	0	0
7	3.37235	7.31803	2.16439	7.55197	5.2684
8	1.76216	3.72981	0.436382	4.52563	2.71612
9	0.215921	0.518335	0.117584	0.57461	0.364696
10	4.45853	4.24922	7.35657	1.27256	4.33626
11	4.13789	2.59828	1.77052	4.57474	3.36561
12	1.03527	0.392798	0.104133	1.24699	0.72489
13	0.014808	0.006998	0.004639	0.016459	0.010957
14	5.27329	5.14708	1.71666	8.17245	5.20909
15	0	0.000344	0	0.000305	0.000167
16	0.013216	0	0	0.01196	0.006786
17	0.004257	0.001467	0	0.005317	0.002794
18	6.41316	6.78817	4.06698	8.59251	6.59939
19	0	0	0	0	0
20	4.54009	4.93294	3.78968	5.48997	4.73492
21	5.40853	5.95374	4.78386	6.31711	5.67664
22	2.33964	2.14384	0.846994	3.49975	2.24422
23	0.00901	0.009044	0	0.016007	0.009027
24	1.49068	1.24801	2.72698	0.072479	1.35395
25	0	0	0	0	0
26	0.001682	5.79E-05	0	0.001465	0.000845
27	0.04261	0.05914	0.053693	0.048402	0.050805
28	5.00942	6.01573	2.74297	7.70034	5.51078
29	3.77741	3.13519	6.95127	0.131219	3.42049
30	0.970617	0.436309	0.23447	1.10879	0.713133
Avg	**1.91745**	**2.04873**	**1.52508**	**2.29094**	**1.97773**

Table 6.1: Results of the percent error in alignment of the lung boundaries obtained with the NParBR method. The value of 0 corresponds to perfect alignment.

Scan Pair	**Left Lung (% Error)**	**Right Lung (% Error)**	**Score (% Error Overall)**
1	1.05315	2.47555	2.19711
2	0	0	0
3	0.037725	0.00388	0.012716
4	0.003211	0	0.001487
5	0	0	0
6	0.023589	0	0.009237
7	6.73057	2.23799	4.6418
8	1.71885	3.25276	2.62629
9	0.000206	0.18755	0.121297
10	0.706629	0	0.445655
11	6.62535	1.05907	2.89967
12	3.47312	4.24611	3.98296
13	2.26649	0.106904	1.50881
14	9.81444	16.8683	13.5872
15	0	0.02383	0.013038
16	0	0.068195	0.05182
17	0.589321	7.32685	4.71204
18	14.2125	5.09512	8.69317
19	0	0	0
20	15.1123	6.52371	9.80174
21	3.12372	2.08911	2.41964
22	0.026219	1.49598	0.743461
23	7.59762	3.06524	4.87145
24	0	0	0
25	0	0.00033	0.000207
26	0.010173	0	0.002977
27	0.0123	2.61679	1.57825
28	2.57662	15.1709	10.6679
29	0	0	0
30	2.54099	0.022057	0.988995
Avg	**2.6085**	**2.46454**	**2.55263**

Table 6.2: Results of the percent error in alignment of the lung fissures obtained with the NParBR method. The value of 0 corresponds to perfect alignment.

6.1.3 Landmark Results

A set of 100 well distributed landmarks have been defined and evaluated using the semi-automatic method proposed by Murphy et al. [152] and marked by at least 3 raters independently. For each registration of each scan pair the following statistics are calculated over the corresponding points for that pair, providing distances in mm:

- Average distance in the Anterior-Posterior (AP) direction
- Average distance in the Superior-Inferior (SI) direction
- Average distance in the Left-Right (LR) direction
- Average distance in the upper lungs
- Average distance in the lower lungs
- Minimum distance
- Maximum distance
- Score points, average distance (This is the overall score in the landmarks category)

The detailed results of lungs landmarks alignment obtained with the NParBR method are shown in Table 6.3.

6.1.4 Singularity Results

The analysis of the singularities is used to evaluate the physical plausibility of the transformation estimated by a registration method. A transformation that is not bijective is considered as a singularity. For each registration of each scan pair the following statistics are calculated:

- The percentage of checked points in the left lung for which penalties incurred
- The percentage of checked points in the right lung for which penalties incurred
- The percentage of checked points in the upper lung for which penalties incurred
- The percentage of checked points in the lower lung for which penalties incurred

Scan Pair	**Avg Dist AP**	**Avg Dist SI**	**Avg Dist LR**	**Avg Dist Upper Lung**	**Avg Dist Lower Lung**	**Min Dist**	**Max Dist**	**Score (Avg Dist)**
1	4.66945	4.753	3.52078	7.01322	9.95479	1.52902	20.9705	8.51342
2	0.28125	0.336	0.316406	0.633392	0.814587	0	1.72102	0.720366
3	1.79297	1.582	1.62422	3.04261	3.68837	0	7.493	3.35903
4	1.92397	3.08945	1.07743	6.36532	1.97374	0.46875	8.78495	4.13676
5	0.091875	0.056	0.065625	0.102941	0.25292	0	1.67968	0.176431
6	0.426562	0.9	0.39	1.2116	1.3845	0	4.70178	1.32225
7	6.58969	5.411	3.85945	8.87279	12.0644	0.7	26.1041	10.3799
8	2.895	4.144	1.7025	3.91347	7.51803	0.7	19.0597	5.85993
9	1.52441	2.268	1.62012	3.11789	4.3924	0.683594	9.91849	3.7424
10	3.26026	5.91025	1.78405	11.7693	3.28189	0.894108	16.195	7.46224
11	2.82418	3.339	1.95686	3.96237	7.48213	0.7	17.6685	5.54184
12	3.58231	2.24	2.9775	4.98845	6.79029	1.04462	13.5819	5.97947
13	1.21094	1.2	0.908203	2.10127	2.54524	0	7.17358	2.34101
14	9.79242	4.963	4.62234	12.9299	14.1933	1.68889	29.8636	13.5489
15	0.50625	0.714	0.555469	0.906582	1.6023	0	6.37799	1.29619
16	0.537109	0.95	0.478516	1.10207	1.88903	0	10.0476	1.51129
17	1.01562	1.64	0.73242	2.35923	2.70261	0	10.466	2.47
18	7.92285	4.067	2.80957	7.87425	12.8518	1.36719	23.9929	10.363
19	0.345156	0.329	0.315781	0.715066	0.822268	0	2.50489	0.764379
20	6.95934	8.526	2.80156	12.0791	12.5916	3.07598	23.8682	12.2943
21	7.81162	4.36429	4.11793	8.3721	13.2672	2.37234	24.4592	10.934
22	4.10938	2.59	2	4.62005	6.91533	0.78125	10.9904	5.9054
23	0.429687	0.725	0.322266	0.965238	1.50092	0	5.09447	1.24915
24	3.30145	3.96123	1.17077	8.14511	2.07394	0.488281	11.3903	5.59246
25	0.391016	0.245	0.412344	0.702628	0.89514	0	5.91561	0.789258
26	0.449414	0.765	0.394102	1.03806	1.43886	0	3.43669	1.25449
27	1.73092	3.71	1.60242	3.72168	5.8421	0	11.699	4.8243
28	4.89645	5.733	3.49002	7.57836	11.0523	1.58548	25.9483	9.30904
29	2.9524	3.69755	1.10147	7.76267	1.73927	0.488281	13.9315	5.1712
30	1.91387	1.673	2.60254	4.31607	4.17588	0	11.6624	4.24458
Avg	**2.87126**	**2.79606**	**1.71109**	**4.74276**	**5.25657**	**0.618926**	**12.89**	**5.03523**

Table 6.3: Results of the distance error (mm) in alignment of the pre-determined landmarks obtained with the NParBR method. The value of 0 corresponds to perfect alignment.

- Score singularities, the percentage of total checked points for which penalties incurred. (This is the overall score in the singularities category)

The detailed results regarding the presence of singularities obtained with the NParBR method are shown in Table 6.4.

Scan Pair	**Left Lung (% Error)**	**Right Lung (% Error)**	**Upper Lung (% Error)**	**Lower Lung (% Error)**	**Score (% Error Overall)**
1	0.110722	0.185568	0.000346	0.307477	0.153912
2	0	0.001019	0	0.001046	0.000523
3	0.063173	0.019327	0.009235	0.071567	0.040401
4	0.189382	0.204036	0.29559	0.10131	0.19845
5	0	0.022442	0	0.022965	0.011482
6	0.043329	0.151874	0.036417	0.157869	0.097143
7	0.109221	0.07709	0.002734	0.184981	0.093857
8	0.071261	0.060222	0.00031	0.130638	0.065474
9	0.01712	0.002121	0.001665	0.017059	0.009362
10	1.45151	0.87983	1.54803	0.648466	1.09825
11	0.082586	0.115432	0.001678	0.200663	0.101171
12	0.008893	0.000941	0.000402	0.008612	0.004507
13	0.005721	0.001503	0	0.007522	0.003761
14	0.101826	0.130776	0.082953	0.149778	0.116366
15	0.018734	0.024169	0	0.043192	0.021596
16	0.035687	0.081639	0.012135	0.11266	0.062397
17	0.027315	0.008191	0	0.033516	0.016758
18	0.082832	0.088659	0.001293	0.170286	0.085789
19	0.000512	0	0	0.000433	0.000217
20	0.155652	0.203876	0.034662	0.32966	0.182161
21	0.183338	0.146796	5.04E-05	0.327884	0.163967
22	0.077427	0.073276	0.02525	0.125214	0.075232
23	0.08387	0.019392	0.039614	0.060186	0.0499
24	0.353557	0.75993	0.387139	0.798092	0.592615
25	0	1.16E-05	0	1.21E-05	6.07E-06
26	0.01788	0.017693	0.003871	0.031686	0.017778
27	0.058838	0.128883	0.002061	0.188088	0.095075
28	0.107293	0.090556	0	0.196502	0.098251
29	0.145209	0.419365	0.190825	0.415943	0.303384
30	0.015761	0.004913	0.005941	0.013986	0.009963
Avg	**0.120622**	**0.130651**	**0.089407**	**0.16191**	**0.125658**

Table 6.4: Results of the percentage of checked points for which singularities are present as obtained with the NParBR method. The value of 0 corresponds to no singularities.

List of Figures

List of Tables

Bibliography

[1] D. Rueckert, L. Sonoda, C. Hayes, D. Hill, M. Leach, and D. Hawkes, "Non-rigid registration using free-form deformations: application to breast MR images," *IEEE Transactions on Medical Imaging*, vol. 18, no. 8, pp. 712–721, 1999.

[2] J. Thirion, "Image matching as a diffusion process: an analogy with Maxwell's Demons," *Medical Image Analysis*, vol. 2, no. 3, pp. 243–260, 1998.

[3] B. B. Avants, C. L. Epstein, M. Grossman, and J. C. Gee, "Symmetric diffeomorphic image registration with cross-correlation: evaluating automated labeling of elderly and neurodegenerative brain," *Medical Image Analysis*, vol. 12, no. 1, pp. 26–41, 2008.

[4] E. Hadjidemetriou, M. D. Grossberg, and S. K. Nayar, "Histogram preserving image transformations," *International Journal of Computer Vision*, vol. 45, no. 1, pp. 5–23, 2001.

[5] M. A. Brown and R. C. Semelka, *MRI: basic principles and applications.* John Wiley & Sons, 2011.

[6] R. W. Brown, Y.-C. N. Cheng, E. M. Haacke, M. R. Thompson, and R. Venkatesan, *Magnetic resonance imaging: physical principles and sequence design.* John Wiley & Sons, 2014.

[7] M. A. Bernstein, K. F. King, and X. J. Zhou, *Handbook of MRI pulse sequences.* Elsevier, 2004.

[8] K. Murphy, B. Van Ginneken, J. M. Reinhardt, S. Kabus, K. Ding, X. Deng, K. Cao, K. Du, G. E. Christensen, V. Garcia, *et al.*, "Evaluation of registration methods on thoracic CT: the EMPIRE10 challenge," *IEEE Transactions on Medical Imaging*, vol. 30, no. 11, pp. 1901–1920, 2011.

[9] G. T. Herman, *Fundamentals of computerized tomography: image reconstruction from projections.* Springer Science & Business Media, 2009.

[10] J. Hsieh, "Computed tomography: principles, design, artifacts, and recent advances," SPIE Bellingham, WA, 2009.

[11] W. A. Kalender, *Computed tomography: fundamentals, system technology, image quality, applications.* John Wiley & Sons, 2011.

[12] R. S. Frackowiak, K. J. Friston, C. D. Frith, R. J. Dolan, C. J. Price, S. Zeki, J. T. Ashburner, and W. D. Penny, *Human brain function.* Academic Press, 2004.

[13] M. Holden, "A review of geometric transformations for nonrigid body registration," *IEEE Transactions on Medical Imaging*, vol. 27, no. 1, pp. 111–128, 2008.

[14] B. Zitova and J. Flusser, "Image registration methods: a survey," *Image and Vision Computing*, vol. 21, no. 11, pp. 977–1000, 2003.

[15] A. Klein, J. Andersson, B. A. Ardekani, J. Ashburner, B. Avants, M.-C. Chiang, G. E. Christensen, D. L. Collins, J. Gee, P. Hellier, *et al.*, "Evaluation of 14 nonlinear deformation algorithms applied to human brain MRI registration," *Neuroimage*, vol. 46, no. 3, pp. 786–802, 2009.

[16] Y. Ou, H. Akbari, M. Bilello, X. Da, and C. Davatzikos, "Comparative evaluation of registration algorithms in different brain databases with varying difficulty: Results and insights," 2014.

[17] W. R. Crum, T. Hartkens, and D. L. G. Hill, "Non-rigid image registration: Theory and practice," *British Journal of Radiology*, vol. 77, no. SPEC. ISS. 2, 2004.

[18] A. Sotiras, C. Davatzikos, and N. Paragios, "Deformable medical image registration: A survey," *IEEE Transactions on Medical Imaging*, vol. 32, no. 7, pp. 1153–1190, 2013.

[19] D. G. Lowe, "Object recognition from local scale-invariant features," in *Proceedings of IEEE International Conference on Computer Vision*, vol. 2, pp. 1150–1157, 1999.

[20] D. G. Lowe, "Distinctive image features from scale-invariant keypoints," *International Journal of Computer Vision*, vol. 60, no. 2, pp. 91–110, 2004.

[21] L. Juan and O. Gwun, "A comparison of sift, pca-sift and surf," *International Journal of Image Processing (IJIP)*, vol. 3, no. 4, pp. 143–152, 2009.

[22] D. Ziou, S. Tabbone, *et al.*, "Edge detection techniques-an overview," *Pattern Recognition and Image Analysis C/C of Raspoznavaniye Obrazov I Analiz Izobrazhenii*, vol. 8, pp. 537–559, 1998.

[23] K. Rohr, *Landmark-based image analysis: using geometric and intensity models*, vol. 21. Springer Science & Business Media, 2001.

[24] M. Leordeanu and M. Hebert, "A spectral technique for correspondence problems using pairwise constraints," in *Proceedings of IEEE International Conference on Computer Vision*, vol. 2, pp. 1482–1489, IEEE, 2005.

[25] O. Duchenne, F. Bach, I.-S. Kweon, and J. Ponce, "A tensor-based algorithm for high-order graph matching," *IEEE Transactions on Pattern Analysis and Machine Intelligence*, vol. 33, no. 12, pp. 2383–2395, 2011.

[26] R. Zass and A. Shashua, "Probabilistic graph and hypergraph matching," in *Proceedings of IEEE Conference on Computer Vision and Pattern Recognition, CVPR*, pp. 1–8, IEEE, 2008.

[27] K. Rohr, H. S. Stiehl, R. Sprengel, T. M. Buzug, J. Weese, and M. H. Kuhn, "Landmark-based elastic registration using approximating thin-plate splines," *IEEE Transactions on Medical Imaging*, vol. 20, no. 6, pp. 526–534, 2001.

[28] D. Shen and C. Davatzikos, “HAMMER: Hierarchical attribute matching mechanism for elastic registration,” *IEEE Transactions on Medical Imaging*, vol. 21, no. 11, pp. 1421–1439, 2002.

[29] G. Wu, Q. Wang, H. Jia, and D. Shen, “Feature-based groupwise registration by hierarchical anatomical correspondence detection,” *Human Brain Mapping*, vol. 33, no. 2, pp. 253–271, 2012.

[30] A. Roche, X. Pennec, G. Malandain, and N. Ayache, “Rigid registration of 3-D ultrasound with MR images: a new approach combining intensity and gradient information,” *IEEE Transactions on Medical Imaging*, vol. 20, no. 10, pp. 1038–1049, 2001.

[31] W. Wein, S. Brunke, A. Khamene, M. R. Callstrom, and N. Navab, “Automatic CT-ultrasound registration for diagnostic imaging and image-guided intervention,” *Medical Image Analysis*, vol. 12, no. 5, pp. 577–585, 2008.

[32] J. A. Maintz, P. A. van den Elsen, and M. A. Viergever, “3d multimodality medical image registration using morphological tools,” *Image and Vision Computing*, vol. 19, no. 1, pp. 53–62, 2001.

[33] M. P. Heinrich, M. Jenkinson, M. Bhushan, T. Matin, F. V. Gleeson, M. Brady, and J. A. Schnabel, “Mind: Modality independent neighbourhood descriptor for multimodal deformable registration,” *Medical Image Analysis*, vol. 16, no. 7, pp. 1423–1435, 2012.

[34] W. Wells III, P. Viola, H. Atsumi, S. Nakajima, and R. Kikinis, “Multi-modal volume registration by maximization of mutual information,” *Medical Image Analysis*, vol. 1, no. 1, pp. 35–51, 1996.

[35] P. Viola and W. M. Wells III, “Alignment by maximization of mutual information,” *International Journal of Computer Vision*, vol. 24, no. 2, pp. 137–154, 1997.

[36] F. Maes, A. Collignon, D. Vandermeulen, G. Marchal, and P. Suetens, “Multimodality image registration by maximization of mutual information,” *IEEE Transactions on Medical Imaging*, vol. 16, no. 2, pp. 187–198, 1997.

[37] A. Roche, G. Malandain, X. Pennec, and N. Ayache, “The correlation ratio as a new similarity measure for multimodal image registration,” in *Medical Image Computing and Computer-Assisted InterventationMICCAI*, pp. 1115–1124, Springer, 1998.

[38] Y. Ou, A. Sotiras, N. Paragios, and C. Davatzikos, “DRAMMS: Deformable registration via attribute matching and mutual-saliency weighting,” *Medical Image Analysis*, vol. 15, no. 4, pp. 622–639, 2011.

[39] P. Hellier and C. Barillot, “Coupling dense and landmark-based approaches for nonrigid registration,” *IEEE Transactions on Medical Imaging*, vol. 22, no. 2, pp. 217–227, 2003.

[40] A. Sotiras, Y. Ou, B. Glocker, C. Davatzikos, and N. Paragios, “Simultaneous geometric-iconic registration,” in *Proceedings of Medical Image Computing and Computer-Assisted Intervention–MICCAI*, pp. 676–683, Springer, 2010.

[41] S. Damas, O. Cordón, and J. Santamara, "Medical image registration using evolutionary computation: An experimental survey," *IEEE Computational Intelligence Magazine*, vol. 6, no. 4, pp. 26–42, 2011.

[42] C. A. Cocosco, V. Kollokian, R. K.-S. Kwan, G. B. Pike, and A. C. Evans, "BrainWeb: Online interface to a 3D MRI simulated brain database," in *NeuroImage*, Citeseer, 1997.

[43] D. Rueckert, P. Aljabar, R. A. Heckemann, J. V. Hajnal, and A. Hammers, "Diffeomorphic registration using B-splines," in *Proceedings of Medical Image Computing and Computer-Assisted Intervention–MICCAI*, pp. 702–709, Springer, 2006.

[44] T. Rohlfing, C. R. Maurer Jr, D. A. Bluemke, and M. A. Jacobs, "Volume-preserving nonrigid registration of MR breast images using free-form deformation with an incompressibility constraint," *IEEE Transactions on Medical Imaging*, vol. 22, no. 6, pp. 730–741, 2003.

[45] J. A. Schnabel, D. Rueckert, M. Quist, J. M. Blackall, A. D. Castellano-Smith, T. Hartkens, G. P. Penney, W. A. Hall, H. Liu, C. L. Truwit, *et al.*, "A generic framework for non-rigid registration based on non-uniform multi-level free-form deformations," in *Proceedings of Medical Image Computing and Computer-Assisted Intervention–MICCAI*, pp. 573–581, Springer, 2001.

[46] W. Shi, X. Zhuang, L. Pizarro, W. Bai, H. Wang, K.-P. Tung, P. Edwards, and D. Rueckert, "Registration using sparse free-form deformations," in *Proceedings of Medical Image Computing and Computer-Assisted Intervention–MICCAI*, pp. 659–666, Springer, 2012.

[47] V. Noblet, C. Heinrich, F. Heitz, and J.-P. Armspach, "Symmetric nonrigid image registration: application to average brain templates construction," in *Proceedings of Medical Image Computing and Computer-Assisted Intervention–MICCAI*, pp. 897–904, Springer, 2008.

[48] M. Modat, M. J. Cardoso, P. Daga, D. Cash, N. C. Fox, and S. Ourselin, "Inverse-consistent symmetric free form deformation," in *Biomedical Image Registration*, pp. 79–88, Springer, 2012.

[49] A. Sotiras and N. Paragios, "Discrete symmetric image registration," in *Proceedings of IEEE International Symposium on Biomedical Imaging (ISBI)*, pp. 342–345, IEEE, 2012.

[50] D. Perperidis, R. H. Mohiaddin, and D. Rueckert, "Spatio-temporal free-form registration of cardiac MR image sequences," *Medical Image Analysis*, vol. 9, no. 5, pp. 441–456, 2005.

[51] M. J. Ledesma-Carbayo, J. Kybic, M. Desco, A. Santos, M. Suhling, P. Hunziker, and M. Unser, "Spatio-temporal nonrigid registration for ultrasound cardiac motion estimation," *IEEE Transactions on Medical Imaging*, vol. 24, no. 9, pp. 1113–1126, 2005.

[52] J. Vandemeulebroucke, S. Rit, J. Kybic, P. Clarysse, and D. Sarrut, "Spatiotemporal motion estimation for respiratory-correlated imaging of the lungs," *Medical Physics*, vol. 38, no. 1, pp. 166–178, 2011.

[53] C. Metz, S. Klein, M. Schaap, T. van Walsum, and W. J. Niessen, "Nonrigid registration of dynamic medical imaging data using nD+ t B-splines and a groupwise optimization approach," *Medical Image Analysis*, vol. 15, no. 2, pp. 238–249, 2011.

[54] T. Brox, *From pixels to regions: partial differential equations in image analysis.* PhD thesis, 2005.

[55] B. K. Horn and B. G. Schunck, "Determining optical flow," in *Technical Symposium East*, pp. 319–331, International Society for Optics and Photonics, 1981.

[56] B. Horn, *Robot vision.* MIT press, 1986.

[57] B. D. Lucas, T. Kanade, *et al.*, "An iterative image registration technique with an application to stereo vision.," in *IJCAI*, vol. 81, pp. 674–679, 1981.

[58] D. M. Young, *Iterative solution of large linear systems.* Elsevier, 1971.

[59] A. Bruhn, J. Weickert, C. Feddern, T. Kohlberger, and C. Schnorr, "Variational optical flow computation in real time," *IEEE Transactions on Image Processing*, vol. 14, no. 5, pp. 608–615, 2005.

[60] T. Brox, A. Bruhn, N. Papenberg, and J. Weickert, "High accuracy optical flow estimation based on a theory for warping," in *Computer Vision-ECCV*, pp. 25–36, Springer, 2004.

[61] T. Brox and J. Malik, "Large displacement optical flow: descriptor matching in variational motion estimation," *IEEE Transactions on Pattern Analysis and Machine Intelligence*, vol. 33, no. 3, pp. 500–513, 2011.

[62] G. Hermosillo, C. Chefd'Hotel, and O. Faugeras, "Variational methods for multimodal image matching," *International Journal of Computer Vision*, vol. 50, no. 3, pp. 329–343, 2002.

[63] G. Palos, N. Betrouni, M. Coulanges, M. Vermandel, V. Devlaminck, and J. Rousseau, "Multimodal matching by maximisation of mutual information and optical flow technique," in *Proceedings of Annual International Conference of the IEEE Engineering in Medicine and Biology Society*, vol. 1, pp. 1679–1682, IEEE, 2004.

[64] A. Martel, M. Froh, K. Brock, D. Plewes, and D. Barber, "Evaluating an optical-flow-based registration algorithm for contrast-enhanced magnetic resonance imaging of the breast," *Physics in Medicine and Biology*, vol. 52, p. 3803, 2007.

[65] T. Vercauteren, X. Pennec, A. Perchant, and N. Ayache, "Non-parametric diffeomorphic image registration with the demons algorithm," in *Proceedings of Medical Image Computing and Computer-Assisted Intervention–MICCAI*, pp. 319–326, Springer, 2007.

[66] T. Vercauteren, X. Pennec, A. Perchant, and N. Ayache, "Symmetric log-domain diffeomorphic registration: A demons-based approach," in *Proceedings of Medical Image Computing and Computer-Assisted Intervention–MICCAI*, pp. 754–761, Springer, 2008.

[67] T. Mansi, X. Pennec, M. Sermesant, H. Delingette, and N. Ayache, "ilogdemons: A demons-based registration algorithm for tracking incompressible elastic biological tissues," *International Journal of Computer Vision*, vol. 92, no. 1, pp. 92–111, 2011.

[68] A. Guimond, A. Roche, N. Ayache, and J. Meunier, "Three-dimensional multimodal brain warping using the demons algorithm and adaptive intensity corrections," *IEEE Transactions on Medical Imaging*, vol. 20, no. 1, pp. 58–69, 2001.

[69] M. Modat, T. Vercauteren, G. Ridgway, D. Hawkes, N. Fox, and S. Ourselin, "Diffeomorphic Demons using normalised mutual information, evaluation on multi-modal brain MR images," SPIE-The International Society for Optical Engineering, 2010.

[70] H. Lu, M. Reyes, A. Serifovic, S. Weber, Y. Sakurai, H. Yamagata, and P. Cattin, "Multi-modal diffeomorphic Demons registration based on point-wise mutual information," in *Proceedings of IEEE ISBI*, pp. 372–375, 2010.

[71] H. Lu, P. C. Cattin, and M. Reyes, "A hybrid multimodal non-rigid registration of MR images based on diffeomorphic demons," in *Proceedings of International Conference of the IEEE Engineering in Medicine and Biology Society*, pp. 5951–5954, 2010.

[72] S. C. Joshi and M. I. Miller, "Landmark matching via large deformation diffeomorphisms," *IEEE Transactions on Image Processing*, vol. 9, no. 8, pp. 1357–1370, 2000.

[73] S. Marsland and C. J. Twining, "Constructing diffeomorphic representations for the groupwise analysis of nonrigid registrations of medical images," *IEEE Transactions on Medical Imaging*, vol. 23, no. 8, pp. 1006–1020, 2004.

[74] M. F. Beg, M. I. Miller, A. Trouvé, and L. Younes, "Computing large deformation metric mappings via geodesic flows of diffeomorphisms," *International Journal of Computer Vision*, vol. 61, no. 2, pp. 139–157, 2005.

[75] B. B. Avants, N. J. Tustison, G. Song, P. A. Cook, A. Klein, and J. C. Gee, "A reproducible evaluation of ANTs similarity metric performance in brain image registration," *Neuroimage*, vol. 54, no. 3, pp. 2033–2044, 2011.

[76] B. B. Avants, P. Yushkevich, J. Pluta, D. Minkoff, M. Korczykowski, J. Detre, and J. C. Gee, "The optimal template effect in hippocampus studies of diseased populations," *Neuroimage*, vol. 49, no. 3, pp. 2457–2466, 2010.

[77] J. Wouters, E. D'Agostino, F. Maes, D. Vandermeulen, and P. Suetens, "Non-rigid brain image registration using a statistical deformation model," in *Medical Imaging*, pp. 614411–614411, International Society for Optics and Photonics, 2006.

[78] S. Tang, Y. Fan, G. Wu, M. Kim, and D. Shen, "Rabbit: rapid alignment of brains by building intermediate templates," *NeuroImage*, vol. 47, no. 4, pp. 1277–1287, 2009.

[79] T. W. Tang and A. C. Chung, "Non-rigid image registration using graph-cuts," in *Proceedings of Medical Image Computing and Computer-Assisted Intervention–MICCAI*, pp. 916–924, Springer, 2007.

[80] R. W. So and A. C. Chung, "Non-rigid image registration by using graph-cuts with mutual information," in *Proceedings of IEEE ICIP, 2010*, pp. 4429–4432.

[81] R. W. So, T. W. Tang, and A. Chung, "Non-rigid image registration of brain magnetic resonance images using graph-cuts," *Pattern Recognition*, vol. 44, no. 10, pp. 2450–2467, 2011.

[82] C. Studholme, D. L. Hill, D. J. Hawkes, G. UMDS, S. Thomas' Hospitals, and S. T. S. London, "Using voxel similarity as a measure of medical image registration.," in *BMVC*, pp. 1–10, 1994.

[83] D. L. Hill, C. Studholme, and D. J. Hawkes, "Voxel similarity measures for automated image registration," in *Proceedings of SPIE, vol. 2359*, pp. 205–216, International Society for Optics and Photonics, 1994.

[84] G. P. Penney, J. Weese, J. A. Little, P. Desmedt, D. L. Hill, and D. J. Hawkes, "A comparison of similarity measures for use in 2-D-3-D medical image registration," *IEEE Transactions on Medical Imaging*, vol. 17, no. 4, pp. 586–595, 1998.

[85] M. Holden, D. L. Hill, E. R. Denton, J. M. Jarosz, T. C. Cox, T. Rohlfing, J. Goodey, and D. J. Hawkes, "Voxel similarity measures for 3-D serial MR brain image registration," *IEEE Transactions on Medical Imaging*, vol. 19, no. 2, pp. 94–102, 2000.

[86] T. Vercauteren, X. Pennec, A. Perchant, and N. Ayache, "Diffeomorphic demons: Efficient non-parametric image registration," *NeuroImage*, vol. 45, no. 1, pp. S61–S72, 2009.

[87] J. Andersson, S. Smith, and M. Jenkinson, "Fnirt-fmribs non-linear image registration tool," *Human Brain Mapping*, vol. 2008, 2008.

[88] J. P. Pluim, J. A. Maintz, and M. A. Viergever, "Image registration by maximization of combined mutual information and gradient information," in *Proceedings of Medical Image Computing and Computer-Assisted Intervention–MICCAI*, pp. 452–461, Springer, 2000.

[89] T. Gaens, F. Maes, D. Vandermeulen, and P. Suetens, "Non-rigid Multimodal Image Registration Using Mutual Information," p. 1099, 1998.

[90] P. Hellier and C. Barillot, "Multimodal non-rigid warping for correction of distortions in functional MRI," in *Proceedings of Medical Image Computing and Computer-Assisted Intervention–MICCAI*, pp. 512–520, Springer, 2000.

[91] D. Mattes, D. R. Haynor, H. Vesselle, T. K. Lewellen, and W. Eubank, "Pet-ct image registration in the chest using free-form deformations," *IEEE Transactions on Medical Imaging*, vol. 22, no. 1, pp. 120–128, 2003.

[92] F. Zöllner, R. Sance, P. Rogelj, M. Ledesma-Carbayo, J. Rørvik, A. Santos, and A. Lundervold, "Assessment of 3D DCE-MRI of the kidneys using non-rigid image registration and segmentation of voxel time courses," *Comput. Med. Im. and Graphics*, vol. 33, no. 3, pp. 171–181, 2009.

[93] I. Dmitriev, C. Loo, W. Vogel, K. Pengel, and K. Gilhuijs, "Fully automated deformable registration of breast DCE-MRI and PET/CT," *Physics in Medicine and Biology*, vol. 58, no. 4, p. 1221, 2013.

[94] C. Studholme, D. L. Hill, and D. J. Hawkes, "An overlap invariant entropy measure of 3D medical image alignment," *Pattern Recognition*, vol. 32, no. 1, pp. 71–86, 1999.

[95] T. Rohlfing and C. R. Maurer Jr, "Intensity-based non-rigid registration using adaptive multilevel free-form deformation with an incompressibility constraint," in *Proceedings of Medical Image Computing and Computer-Assisted Intervention–MICCAI*, pp. 111–119, Springer, 2001.

[96] C. Tanner, J. A. Schnabel, A. Degenhard, A. D. Castellano-Smith, C. Hayes, M. O. Leach, D. R. Hose, D. L. Hill, and D. J. Hawkes, "Validation of volume-preserving non-rigid registration: Application to contrast-enhanced MR-mammography," in *Proceedings of Medical Image Computing and Computer-Assisted InterventionMICCAI*, pp. 307–314, Springer, 2002.

[97] F. Maes, D. Vandermeulen, and P. Suetens, "Medical image registration using mutual information," *Proceedings of the IEEE*, vol. 91, no. 10, pp. 1699–1722, 2003.

[98] J. P. W. Pluim, J. B. A. Maintz, and M. A. Viergever, "Mutual-information-based registration of medical images: a survey," *IEEE Transactions on Medical Imaging*, vol. 22, no. 8, pp. 986–1004, 2003.

[99] S. Klein, M. Staring, and J. P. Pluim, "Evaluation of optimization methods for nonrigid medical image registration using mutual information and b-splines," *IEEE Transactions on Image Processing*, vol. 16, no. 12, pp. 2879–2890, 2007.

[100] C. Tanner, J. A. Schnabel, D. Chung, M. J. Clarkson, D. Rueckert, D. L. Hill, and D. J. Hawkes, "Volume and shape preservation of enhancing lesions when applying non-rigid registration to a time series of contrast enhancing MR breast images," in *Proceedings of Medical Image Computing and Computer-Assisted Intervention–MICCAI*, pp. 327–337, Springer, 2000.

[101] M. Modat, G. R. Ridgway, D. J. Hawkes, N. C. Fox, and S. Ourselin, "Nonrigid registration with differential bias correction using normalised mutual information," in *IEEE International Symposium on Biomedical Imaging: From Nano to Macro*, pp. 356–359, IEEE, 2010.

[102] M. F. Beg and A. Khan, "Symmetric data attachment terms for large deformation image registration," *IEEE Transactions on Medical Imaging*, vol. 26, no. 9, pp. 1179–1189, 2007.

[103] W. W. Hager and H. Zhang, "A survey of nonlinear conjugate gradient methods," *Pacific Journal of Optimization*, vol. 2, no. 1, pp. 35–58, 2006.

[104] G. Postelnicu, L. Zöllei, and B. Fischl, "Combined volumetric and surface registration," *IEEE Transactions on Medical Imaging*, vol. 28, no. 4, pp. 508–522, 2009.

[105] A. Joshi, D. W. Shattuck, P. M. Thompson, R. M. Leahy, *et al.*, "Surface-constrained volumetric brain registration using harmonic mappings," *IEEE Transactions on Medical Imaging*, vol. 26, no. 12, pp. 1657–1669, 2007.

[106] D. Mattes, D. R. Haynor, H. Vesselle, T. K. Lewellen, and W. Eubank, "Nonrigid multimodality image registration," *Medical Imaging*, vol. 4322, no. 1, pp. 1609–1620, 2001.

[107] T. Song, V. S. Lee, H. Rusinek, M. Kaur, and A. F. Laine, "Automatic 4-D registration in dynamic MR renography," in *Proceedings of Annual International Conference of the Engineering in Medicine and Biology Society*, pp. 3067–3070, IEEE, 2006.

[108] R. Sance, M. J. Ledesma-Carbayo, A. Lundervold, and A. Santos, "Alignment of 3D DCE-MRI abdominal series for optimal quantification of kidney function," in *Proceedings of 5th International Symposium on Image and Signal Processing and Analysis, ISPA*, pp. 413–417, IEEE, 2007.

[109] M. Khader and A. B. Hamza, "Nonrigid image registration using an entropic similarity," *IEEE Transactions on Information Technology in Biomedicine*, vol. 15, no. 5, pp. 681–690, 2011.

[110] Y.-T. Wu, T. Kanade, C.-C. Li, and J. Cohn, "Image registration using wavelet-based motion model," *International Journal of Computer Vision*, vol. 38, no. 2, pp. 129–152, 2000.

[111] J. Ashburner, "A fast diffeomorphic image registration algorithm," *Neuroimage*, vol. 38, no. 1, pp. 95–113, 2007.

[112] M. Modat, G. R. Ridgway, P. Daga, M. J. Cardoso, D. J. Hawkes, J. Ashburner, and S. Ourselin, "Log-Euclidean free-form deformation," in *SPIE Medical Imaging*, pp. 79621Q–79621Q, International Society for Optics and Photonics, 2011.

[113] D. Greig, B. Porteous, and A. H. Seheult, "Exact maximum a posteriori estimation for binary images," *Journal of the Royal Statistical Society. Series B (Methodological)*, pp. 271–279, 1989.

[114] Y. Boykov, O. Veksler, and R. Zabih, "Fast approximate energy minimization via graph cuts," *IEEE Transactions on Pattern Analysis and Machine Intelligence*, vol. 23, no. 11, pp. 1222–1239, 2001.

[115] D. Mahapatra and Y. Sun, "Nonrigid registration of dynamic renal MR images using a saliency based MRF model," in *Proceedings of Medical Image Computing and Computer-Assisted Intervention–MICCAI*, pp. 771–779, Springer, 2008.

[116] S. Liao and A. Chung, "Nonrigid brain MR image registration using uniform spherical region descriptor," *IEEE Transactions on Image Processing*, vol. 21, no. 1, pp. 157–169, 2012.

[117] N. Komodakis and G. Tziritas, "Approximate labeling via graph cuts based on linear programming," *IEEE Transactions on Pattern Analysis and Machine Intelligence*, vol. 29, no. 8, pp. 1436–1453, 2007.

[118] B. Glocker, N. Komodakis, G. Tziritas, N. Navab, and N. Paragios, "Dense image registration through MRFs and efficient linear programming," *Medical Image Analysis*, vol. 12, no. 6, pp. 731–741, 2008.

[119] A. Sotiras, N. Komodakis, B. Glocker, J.-F. Deux, and N. Paragios, "Graphical models and deformable diffeomorphic population registration using global and local metrics," in *Proceedings of Medical Image Computing and Computer-Assisted Intervention–MICCAI*, pp. 672–679, Springer, 2009.

[120] J. Santamaría, O. Cordón, and S. Damas, "A comparative study of state-of-the-art evolutionary image registration methods for 3D modeling," *Computer Vision and Image Understanding*, vol. 115, no. 9, pp. 1340–1354, 2011.

[121] A. Melbourne, D. Atkinson, M. White, D. Collins, M. Leach, and D. Hawkes, "Registration of dynamic contrast-enhanced MRI using a progressive principal component registration (PPCR)," *Physics in Medicine and Biology*, vol. 52, no. 17, p. 5147, 2007.

[122] N. Wiener, *Cybernetics-: or the Control and Communication in the Animal and the Machine*, vol. 25. MIT press, 1965.

[123] E. P. Simoncelli and E. H. Adelson, "Noise removal via Bayesian wavelet coring," in *Proceedings of IEEE ICIP, 1996*, vol. 1, pp. 379–382.

[124] J. G. Sled, A. P. Zijdenbos, and A. C. Evans, "A non-parametric method for automatic correction of intensity nonuniformity in MRI data," *IEEE Transactions on Medical Imaging*, vol. 17, no. 1, pp. 87–97, 1998.

[125] T. Rohlfing, "Image similarity and tissue overlaps as surrogates for image registration accuracy: widely used but unreliable," *IEEE Transactions on Medical Imaging*, vol. 31, no. 2, pp. 153–163, 2012.

[126] P. Lorenzen, M. Prastawa, B. Davis, G. Gerig, E. Bullitt, and S. Joshi, "Multi-modal image set registration and atlas formation," *Medical Image Analysis*, vol. 10, no. 3, pp. 440–451, 2006.

[127] S. Xu, M. Styner, B. Davis, S. Joshi, and G. Gerig, "Group mean differences of voxel and surface objects via non-linear averaging," in *Proceedings of IEEE ISBI*, pp. 758–761, 2006.

[128] D. Pilutti, M. Strumia, and S. Hadjidemetriou, "Bimodal nonrigid registration of brain MRI data with deconvolution of joint statistics," *IEEE Transactions on Image Processing*, vol. 23, no. 9, pp. 3999–4009, 2014.

[129] D. Pilutti, M. Strumia, and S. Hadjidemetriou, "Non-parametric bayesian registration (NParBR) on CT lungs data-EMPIRE10 challenge,"

[130] D. Pilutti, M. Strumia, M. Büchert, and S. Hadjidemetriou, "Non-parametric bayesian registration (NParBR) of body tumors in DCE-MRI data," *IEEE Transactions on Medical Imaging*, 2015.

[131] S. M. Smith, "Fast robust automated brain extraction," *Human Brain Mapping*, vol. 17, no. 3, pp. 143–155, 2002.

[132] A. Vidal-Pantaleoni and D. Marti, "Comparison of different speckle-reduction techniques in SAR images using wavelet transform," *International Journal of Remote Sensing*, vol. 25, no. 22, pp. 4915–4932, 2004.

[133] L. Ibanez, W. Schroeder, L. Ng, and J. Cates, *The ITK Software Guide*. Kitware, Inc. ISBN 1-930934-15-7, second ed., 2005.

[134] L. A. Shepp and B. F. Logan, "The Fourier reconstruction of a head section," *Nuclear Science, IEEE Transactions on*, vol. 21, no. 3, pp. 21–43, 1974.

[135] M. Schabel, “3D Shepp-Logan phantom,” *MATLAB Central File Exchange*, pp. 1–35, 2006.

[136] G. E. Christensen, X. Geng, J. G. Kuhl, J. Bruss, T. J. Grabowski, I. A. Pirwani, M. W. Vannier, J. S. Allen, and H. Damasio, “Introduction to the non-rigid image registration evaluation project (NIREP),” in *Biomedical Image Registration*, pp. 128–135, Springer, 2006.

[137] MATLAB, *version 7.10.0 (R2010a).* Natick, Massachusetts: The MathWorks Inc., 2010.

[138] P. S. Tofts, “Modeling tracer kinetics in dynamic Gd-DTPA MR imaging,” *Journal of Magnetic Resonance Imaging*, vol. 7, no. 1, pp. 91–101, 1997.

[139] H. Johnson, G. Harris, and K. Williams, “BRAINSFit: Mutual information registrations of whole-brain 3D images, using the insight toolkit,” *Insight J*, 2007.

[140] A. Vignati, V. Giannini, A. Bert, M. Deluca, L. Morra, D. Persano, L. Martincich, and D. Regge, “A fully automatic lesion detection method for DCE-MRI fat-suppressed breast images,” in *SPIE Medical Imaging*, pp. 726026–726026, International Society for Optics and Photonics, 2009.

[141] G. Adluru, E. V. DiBella, and M. C. Schabel, “Model-based registration for dynamic cardiac perfusion MRI,” *Journal of Magnetic Resonance Imaging*, vol. 24, no. 5, pp. 1062–1070, 2006.

[142] C. Zakkaroff, D. Magee, A. Radjenovic, and R. Boyle, “Mediated spatiotemporal registration of cardiac DCE-MRI and coronary MR angiography,” in *Workshop on Spatio-Temporal Image Analysis for Longitudinal and Time-Series Image Data. Beijing*, pp. 1–12, 2010.

[143] C. Li, Y. Sun, and P. Chai, “Pseudo ground truth based nonrigid registration of myocardial perfusion MRI,” *Medical Image Analysis*, vol. 15, no. 4, pp. 449–459, 2011.

[144] L. Ruthotto, E. Hodneland, and J. Modersitzki, “Registration of dynamic contrast enhanced MRI with local rigidity constraint,” in *Biomedical Image Registration*, pp. 190–198, Springer, 2012.

[145] O. Noterdaeme and M. Brady, “Contrast enhanced magnetic resonance imaging of the liver,” in *IEEE EMBS 2008*, pp. 831–834, 2008.

[146] J. Chappelow, B. N. Bloch, N. Rofsky, E. Genega, R. Lenkinski, W. DeWolf, and A. Madabhushi, “Elastic registration of multimodal prostate MRI and histology via multiattribute combined mutual information,” *Medical Physics*, vol. 38, no. 4, pp. 2005–2018, 2011.

[147] S. Steinbild, J. Arends, M. Medinger, B. Häring, A. Frost, J. Drevs, C. Unger, R. Strecker, J. Hennig, and K. Mross, “Metronomic antiangiogenic therapy with capecitabine and celecoxib in advanced tumor patients–results of a phase II study,” *Onkologie*, vol. 30, no. 12, pp. 629–635, 2007.

[148] E. M. van Rikxoort, B. de Hoop, M. A. Viergever, M. Prokop, and B. van Ginneken, "Automatic lung segmentation from thoracic computed tomography scans using a hybrid approach with error detection," *Medical Physics*, vol. 36, no. 7, pp. 2934–2947, 2009.

[149] P. Anandan, "A computational framework and an algorithm for the measurement of visual motion," *International Journal of Computer Vision*, vol. 2, no. 3, pp. 283–310, 1989.

[150] I. Suramo, M. Päivänsalo, and V. Myllylä, "Cranio-caudal movements of the liver, pancreas and kidneys in respiration.," *Acta radiologica: diagnosis*, vol. 25, no. 2, pp. 129–131, 1983.

[151] E. M. Van Rikxoort, B. Van Ginneken, M. Klik, and M. Prokop, "Supervised enhancement filters: application to fissure detection in chest CT scans," *IEEE Transactions on Medical Imaging*, vol. 27, no. 1, pp. 1–10, 2008.

[152] K. Murphy, B. van Ginneken, J. Pluim, S. Klein, and M. Staring, "Semi-automatic reference standard construction for quantitative evaluation of lung CT registration," *Proceedings of Medical Image Computing and Computer-Assisted Intervention–MICCAI*, pp. 1006–1013, 2008.